Determining the topology of hydrogen flame

Using computed tomography of chemiluminescence

Mayanka Jha

Delft University of Technology

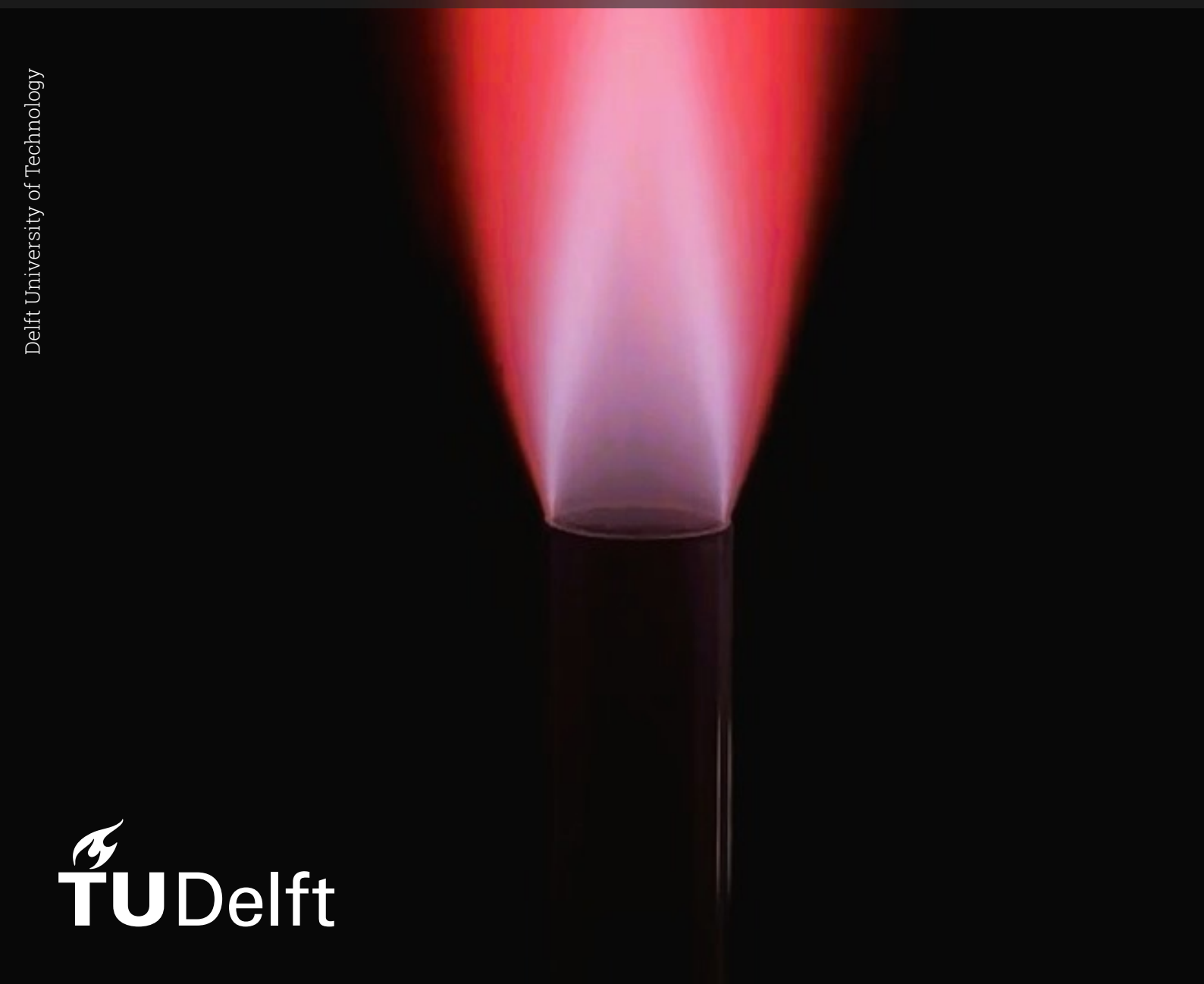

TU Delft

Determining the topology of hydrogen flame

Using computed tomography of chemiluminescence

by

Mayanka Jha

to obtain the degree of Master of Science
at the Delft University of Technology.
to be defended publicly on Friday, October 27, 2023 at 10:00.

Student number: 5478944
Project duration: December 1, 2022 - October 27, 2023
Thesis committee:

Dr.ir.G.E.Elsinga	TU Delft, Supervisor, Chair
Dr.ir.M.J.Tummers	TU Delft, Supervisor
Prof.dr.ir.S.A.Klein	TU Delft,Examiner

TU Delft

Abstract

With ongoing research towards clean combustion, hydrogen has been identified as a potential alternative to natural gas fuel, for example in power generation sectors utilizing gas turbines because of their inherent nature of being a carbon-free energy carrier. However, it is crucial to clarify that the ultimate goal is not just carbon-free combustion but clean combustion, which entails addressing other post-combustion emissions, such as NO_x (nitric oxide) emissions. To meet stringent NO_x emissions regulations, gas turbine fuels are combusted under premixed conditions. But in these premixed conditions, it has been observed that flames produced as a result of combustion have a tendency to flashback, which means that the flame travels back into the premixing chamber causing severe structural damages. This is particularly concerning when using hydrogen, which due to its high reactivity and flame speed is more prone to flashback than natural gas. To understand this high propensity of hydrogen to flashback, there is a strong requirement to examine the topology or structure of flame which can be obtained using optical combustion diagnostics technique.

Considering a flame has a three-dimensional structure, in this thesis, an optical combustion diagnostics technique of Computed Tomography of Chemiluminescence (CTC) was applied to Bunsen burner flames using six CCD cameras. The cameras were arranged around the flame and a tomographic algorithm was used to reconstruct the three-dimensional structure of the flame. The technique was applied to turbulent 100% by volume fraction Dutch Natural Gas (DNG) flames at various Reynolds numbers representing stable, close to flashback, and flashback case. The reconstructed DNG flame results highlighted the capability of the CTC technique to offer valuable insights into the intricate features of the flame. Furthermore, these results not only indicated the possible location of the origin of the flashback within the structure of flame but also revealed specific features associated with events prior to the flashback. Recognizing the potential of this technique, it was subsequently applied to a turbulent flame consisting of 50% hydrogen blended with 50% DNG. The reconstruction results offered insights into the fundamental structural differences between a flame consisting of 50% hydrogen and 50% DNG and a pure 100% DNG flame. The conclusions drawn from the visual assessments of the reconstruction results were further supported by the subsequent statistical analysis and the resulting cone angle values.

Acknowledgement

First and foremost, I would like to convey my deepest gratitude to my supervisors, Dr.ir. G.E. Elsinga and Dr.ir. M.J. Tummers, for their unwavering support and guidance throughout this thesis. Without their expertise and consistent involvement at every stage, this work would never have reached its conclusion. I am particularly appreciative of their invaluable assistance in constructing the experimental setup and conducting experiments, which proved to be of significant help, considering my limited prior experience in this field. Moreover, their meticulous feedback, especially concerning the presentation and documentation of results, played a vital role in enhancing the final report for my master's thesis. I would also like to take this opportunity to thank Prof.dr.ir.S.A.Klein for agreeing to be a part of my thesis committee.

I extend my sincere thanks to Dr. Andrea Sciacchitano and Dr.ir. Adam Head from the Aerospace Department at TU Delft for providing the cameras and data acquisition system, which were essential for conducting the experiments in this thesis. Furthermore, I would also like to thank Ir. Luuk Altenburg for his help not only during the execution of the experiments by operating the burner but also for dedicating his time to discussing the interpretations I drew from my results. I want to extend a huge thanks to Bart Hoek for ensuring that I had all the essential mechanical components necessary to construct my setup. Additionally, I want to express my gratitude to Edwin Overmars for particularly addressing my inquiries related to cameras and the imaging software DAVIS.

During my two-year journey as a master's student in Delft, I have experienced a highly dynamic environment where the only certainties have been uncertainties. But, the one constant and heartwarming aspect of my time here has been the wonderful friends I have had the privilege of making. Thanks to all of you for unknowingly brightening my days with random conversations, lame jokes, and, of course, amazing food. I would also like to thank my friends in India, Pragya, Shelly, Anshika, and Kapil. Despite the time zone differences and their demanding work schedules, none of them ever missed an opportunity to reach out, offer motivational words, or even dish out some friendly scoldings on those challenging days. I am immensely thankful to each of you for being an incredible source of support.

Lastly, but most importantly, I want to extend my profound gratitude to my parents, grandparents, and brother for their unwavering faith in me and their unconditional love and support.

Mayanka Jha
Delft, October 2023

Contents

List of Figures

List of Tables

Nomenclature

Abbreviations

Abbreviation	Definition
ART	**A**lgebraic **R**econstruction **T**echnique
BLF	**B**oundary **L**ayer **F**lashback
CCD	**C**harged **C**oupled **D**evice
CL	**C**hemi**L**uminescence
CT	**C**omputed **T**omography
CTC	**C**omputed **T**omography of **C**hemiluminescence
DNG	**D**utch **N**atural **G**as
FOV	**F**ield **o**f **v**iew
MART	**M**ultiplicative **A**lgebraic **R**econstruction **T**echnique
RMS	**R**oot **M**ean **S**quare

Symbols

Symbol	Definition	Unit
2α	Flame-angle	[degree]
D_b	Inner diameter of the quartz tube.	[mm]
$f\#$	f-stop	[-]
I	Intensity	[counts]
$\bar{I}$	Average Intensity	[counts]
$\sigma(I)$	Standard deviation of intensity	[counts]
l_h	Length of the horizontal tube in the Bunsen burner setup.	[mm]
l_v	Length of the vertical tube (including quartz tube) in the Bunsen burner setup.	[mm]
Re	Reynolds number based on bulk velocity.	[-]
S_L	Flame speed.	[m/s]
t	Wall thickness of the tubes (horizontal and vertical) in the Bunsen burner setup.	[mm]
U_b	Bulk velocity of the flow.	[m/s]
Φ	Equivalence ratio	[-]
μ	MART relaxation parameter	[-]
$\nu_{mixture}$	Kinematic viscosity of fuel mixture.	[m^2/s]

1 Introduction

1.1. Motivation

Hydrogen has gained global recognition as a prospective fuel for the future due to its inherent advantage of clean combustion. However, the exclusive replacement of conventional natural gas fuel with pure hydrogen for the sole objective of maintaining a net zero carbon emission-based approach is not a practical solution. This is primarily due to substantial disparities in fuel properties and their respective combustion behaviors necessitating a more nuanced evaluation of the feasibility and practicality of such transition. As extensive research on hydrogen fuel continues, the phenomenon of flashbacks emerged as a significant obstacle to this fuel transition in gas turbines. The current state of ongoing research acknowledges the challenge posed by hydrogen flames relating to their high propensity to the phenomenon of flashbacks and strives to comprehend the underlying factors responsible for this behavior. However, there is a notable deficiency in the fundamental understanding of the topology or structure of hydrogen flames which limits our capability to prevent the process of flashback. Gaining a visual understanding of the complete topology of hydrogen flames, particularly before and during the initiation of a flashback, will significantly reduce the challenges associated with developing effective control methods for this phenomenon. By establishing a reliable and accurate understanding of the topology of hydrogen flames, there is a possibility to identify one distinctive feature that is explicit to the proximity to the flashback condition.

1.2. Theme

Optical imaging techniques have emerged as a favored means of diagnosing combustion processes. They can be categorized into two-dimensional (2D) and three-dimensional (3D) imaging methods. In the 2D approach, a cross-sectional portion of the flame is illuminated, and the resulting light emissions from the seeded particles are captured. However, considering that combustion is inherently a three-dimensional phenomenon, relying solely on 2D imaging techniques may prove insufficient for effectively investigating flow dynamics, chemical kinetics, and their complex interplay. This limitation has propelled the adoption of 3D imaging techniques in the field. In the context of combustion diagnosis, the implementation of a 3D imaging technique can be further simplified by eliminating the need for an external excitation source. This is because flames inherently emit light, allowing for direct imaging without extensive reliance on external illumination sources. This is the fundamental principle underlying the 3D imaging technique called Computed tomography of chemiluminescence (CTC). Chemiluminescence refers to the spontaneous emission of light from a flame, which occurs when excited species formed through chemical reactions return to their ground state. CTC is a two-step technique in which the first step involves acquiring multiple projections of the chemiluminescence emitted by the flame. This can be achieved either simultaneously by using multiple cameras around the flame or sequentially by rotating a single camera around the flame. During the first step, the chemiluminescence emissions from different angles or perspectives are captured. The acquired projection data is then processed in the second step of CTC using a tomographic algorithm to reconstruct a 3D representation of the flame. By combining the information from multiple projections of the flame, a spatial distribution of

chemiluminescence throughout the flame can be obtained, allowing for a complete understanding of the combustion process.

1.3. Thesis objectives

The thesis has been structured around two objectives recognizing the potential of Computed tomography of chemiluminescence (CTC) in advancing an understanding of the combustion process.

The first objective focuses on attaining and investigating the topology of a turbulent Dutch Natural Gas (DNG) flame. Subsequently, the second and final objective of the thesis is to determine the topology of turbulent hydrogen flames. Both objectives have been selected to conduct analysis on the spatial distributions and characteristics of chemiluminescence emissions from DNG as well as hydrogen flame.

The decision to begin the study with DNG flames rather than hydrogen flames, which exhibit a complex wrinkled topology [29], is motivated by the intention to evaluate and validate the experimental setup and reconstruction results using a flame with simpler characteristics. By starting with DNG the work aims to assess the performance and effectiveness of the experimental setup.

1.4. Thesis outline

The thesis report is organized into five chapters. Chapter 2 initiates the discussion by addressing the significance and complexities of hydrogen combustion. It proceeds to review prior research on combustion using experimental techniques. Within this section of the chapter, the objective is to introduce various 2D flame diagnostic techniques while emphasizing their limitation in delivering a complete understanding of combustion-related phenomena. Finally, the chapter introduces the background theory of flame diagnostic techniques that can be used to address the limitation. Chapter 3 then specifically discusses the previously conducted work to highlight the potential, advancements, and notable results obtained from the chosen flame diagnostic technique of Computed Tomography of Chemiluminescence (CTC). Chapter 4 gives details of the CTC setup, experimental cases, and methodology. Chapter 5 presents the results obtained from both steps of CTC (acquisition and reconstruction of images). Finally, Chapter 6 summarizes the conclusions drawn and recommendations for future work.

2

Hydrogen combustion and diagnostic techniques

Hydrogen, with its carbon-free characteristics, has emerged as a crucial catalyst in the global energy transition toward achieving zero greenhouse gas emissions. In addition to its environmental benefits in terms of pollutant reductions, hydrogen is valued as a significant fuel due to its versatility in being derived from diverse sources, including many that are renewable [31]. In power sectors, utilizing hydrogen as a gas turbine fuel has been both acknowledged and questioned. The following section highlights the reason for considering hydrogen as the primary gas turbine fuel along with the challenges that hinder its full adoption as a 100% substitute for conventional fuels (for example, natural gas).

2.1. The necessity and challenges with hydrogen combustion

In the ongoing energy transition power generation sectors face the challenge of optimizing their units to reduce greenhouse emissions. In this phase, industries utilizing gas turbines are in the foreground due to their operation flexibility, and relatively low investment cost [15]. Confronted with this rapid energy transition that demands affordability, security, and sustainability, the gas turbine industry does have a prospect to firmly establish itself in the future business of power production. Their competency to handle a wide variety of alternative fuels is the primary reason to open up this potential [27]. Hence, a substantial margin for clean combustion and a replacement for regularly utilized fuel like natural gas is provided. Among the many alternative fuels, the carbon-free energy carrier hydrogen has attracted a lot of interest. Nevertheless, it has come to light that, a fully-fledged substitution of conventional fuels with 100% hydrogen leads to a considerable discharge of nitric oxide NO_x emissions due to its high flame temperature thus posing a challenge to its deployment as a primary energy carrier [33]. As the main objective of employing hydrogen at a 100% level is to strive for environment-friendly combustion, it becomes imperative to implement effective measures to manage the resulting NO_x emissions. Therefore, gas turbines operate with lean premixed combustion [1]. As compared to diffusion combustion, lean premixed combustion helps to reduce the post-combustion air dilution while operating with excess air to reduce the flame temperature. In this way, the flame is cooler, and virtually thermal NO_x is eliminated. However, even though lean premixed combustion complies with the regulations of NO_x emissions, it comes with the risk of an undesirable phenomenon called a flashback. Flashback is the upstream propagation of flame towards the burner and into the premix passages that are not designed for sustaining such high temperatures.

Experimental investigations have revealed four different types of flashback mechanisms as summed up by Lieuwen et al. [37]: core flow flashback, flashback due to combustion instabilities, flashback in the core flow due to alteration of vortex breakdown dynamics and flashback in the boundary layer. Each mechanism has been defined below:

1. **Core flow flashback**: This type of flashback is encountered in case the turbulent burning velocity of the mixture exceeds the flow velocity along some streamline. However, following a simple design rule wherein the flow velocity must not have a strong local velocity deficit and the axial

flow velocity must be substantially well above the turbulent flame speed, this type of flashback can be avoided and is therefore not considered a primary flashback mechanism in modern industrial gas turbines.

2. **Flashback due to combustion instabilities**: Combustion instabilities can arise due to the interaction of the acoustic modes, unsteady heat release, and change in flow structure [3]. These instabilities can cause pressure and velocity oscillations, leading to flame movement and the formation of large vortices that may result in flow reversal and potentially cause flashback. However, as stated by Lieuwen et al. [37], such flashbacks are typically infrequent during regular, stable combustion operations. Consequently, this type of flashback does not constitute a primary flashback mechanism in gas turbines because to prevent structural damage, measures are taken to avoid instabilities.
3. **Combustion-induced vortex breakdown (CIVB)**: Flashback triggered due to vortex breakdown is mostly encountered in swirl-stabilized burners. In the stable operation of swirl burners, an internal recirculation zone (IRZ) forms along the burner axis, typically occurring where there is a sudden expansion in the area between the mixing tube and the combustion chamber. Minor changes in the flow field can lead to the formation of a closed bubble around the internal recirculation zone. Under certain conditions, this bubble starts propagating upstream and displaces the flame from the stable position in the combustion chamber into the mixing tube causing flashback [25]. Figure 2.1 shows the flashback mechanism due to combustion-induced vortex breakdown.

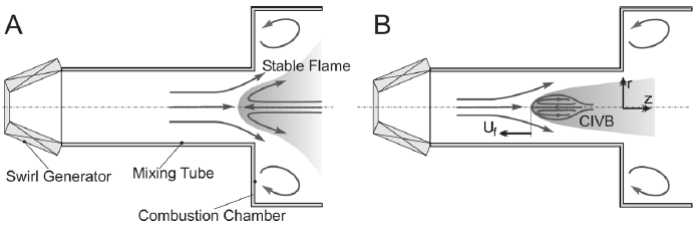

Figure 2.1: Schematic of stable flame (A) and a flashback due to combustion-induced vortex breakdown where U_f is the CIVB-flame speed (B). Adopted from Kröner et al. [26].

4. **Boundary layer flashback (BLF)**: A flashback occurs at a region where the local burning/flame velocity is large enough to overcome the local flow velocity. Due to the no-slip boundary condition, the velocity of the flow decreases to zero towards the burner wall of the premixing tube. This decrease in flow velocity enables the flame velocity to surpass it leading to a potential initiation of flashback [3]. Although the upstream propagation of flame at the wall can be prevented by heat losses to the wall such that the combustion reaction gets quenched, this distance from the wall where the quenching occurs depends on the fuel and flow conditions such as pressure and temperature. For a highly reactive fuel like hydrogen with high adiabatic flame speed, this quenching distance is quite low [38] making it more prone to flashback as compared to other fuels such as natural gas. Therefore in gas turbines that operate on hydrogen, boundary layer flashback is considered the primary flashback mechanism and is thus the flashback mechanism being considered in the present thesis. Figure 2.2 illustrates the time sequence of boundary layer flashback which was captured using high-speed OH chemiluminescence imaging (Note that the coordinates in the figure are normalized by the outer diameter D = 50 mm of the premixing tube). The snapshots from 103 ms to 244 ms show the initiation process of the boundary layer flashback in which the leading flame tongue started to propagate upstream along the wall of the premixing tube.

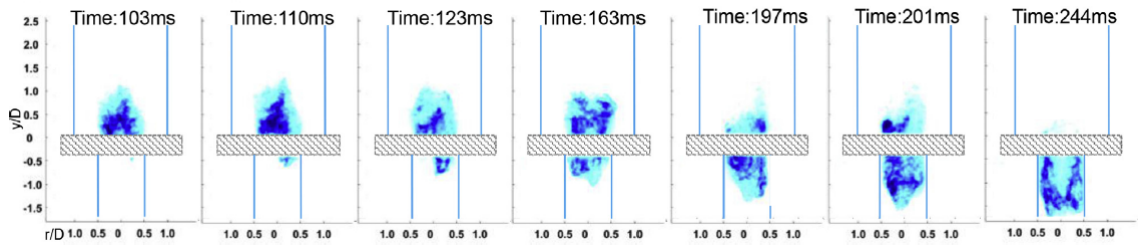

Figure 2.2: Time sequence of boundary layer flashback initiating from the wall of the premixing tube for 50% H_2-enriched-CH_4/Air flame. Adopted from Liu et al. [39].

Since the focus of the study is related to boundary layer flashback therefore Bunsen burner has been employed in the experiments performed in the present thesis to produce turbulent jet flames. A Bunsen burner is a simple tube burner and closely represents the configuration of a premixing tube. Further details about the burner will be presented in Chapter 4.

The unresolved issue of preventing hydrogen flashbacks has impeded the full realization of hydrogen's potential as a future fuel and its complete substitution for natural gas in power generation sectors such as the one using gas turbines. Hence, there is a pressing need to enhance our understanding of hydrogen flashback. Considerable prior research has been conducted to come up with theories that can model the tendency to flashback. In a study by Kalantari et al. [2] boundary layer flashback was investigated for premixed turbulent hydrogen-enriched high-pressure jet flames. The study emphasized that burner head tip temperature is one of the indicators of flashback. Clear peaks at the onset of the flashback were observed in the thermocouple responses. Additionally, the study characterized the flashback systematically by developing a non-dimensional model that takes into account all the effective parameters in boundary layer flashback propensity. In another study by Lin et al. [40] the flashback propensity and turbulent flame speed (S_T) of a hydrogen-rich fuel gas were correlated. Furthermore, using the criteria that flashback in boundary layers occurs when the velocity gradient of flame (g_c) exceeds that of the flow (g_f) the flashback limit (Φ_{FB}) was estimated as an equivalence ratio at which the two velocity gradients match.The limits were calculated for both syngas mixture (H_2-CO:50-50; the numbers are in volume %) and hydrogen-rich fuel gas. With the derived flashback limits reasonable operational limits for syngas and hydrogen-rich fuels were also estimated leading to a conclusion that flashback occurs at much leaner conditions for hydrogen-rich fuels compared to syngas. While models that provide relationships to detect flashback initiation are beneficial for estimating safe operational limits in gas turbines, but an understanding of flashbacks in hydrogen-fueled gas turbines can be further enhanced by focusing on the fundamental task of characterizing the structure or topology of flames. Integrating visual information can substantially enhance data for both numerical and experimental examinations of hydrogen flashback phenomena and contribute to the development of flashback mitigation techniques in gas turbines. Additionally, the progress in optical measurement techniques provides further reinforcement for the effective implementation of this approach.

Therefore, the central objective of this thesis is to explore and report structural features of flames pertaining to the events before the initiation of flashback using optical measurement techniques, also referred to as combustion/ flame diagnostic techniques within the scope of this study.

2.2. Combustion diagnostics

This section first discusses the definition and identification of a flame's topology/structure within the scope of the present work. Then some previous studies that utilized two-dimensional combustion diagnostic techniques for attaining the flame topology have been elaborated. Finally, the background theory of the three-dimensional combustion diagnosis technique used in this work has been described.

2.2.1. Topology of a flame

The topology of a flame in this study has been defined by the 'flame front' which is a spatial domain where the combustion reaction takes place. Figure 2.3 shows a representative diagram of Bunsen burner flame. The figure illustrates the flame front of a flame having velocity S_L forming a cone angle 2α, with a mixture (fuel + air) or flow velocity U.

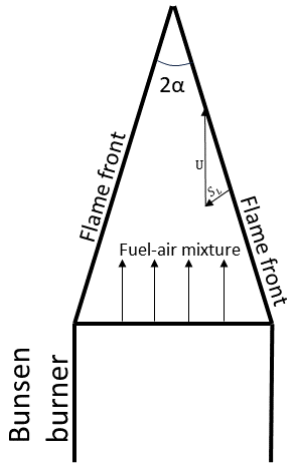

Figure 2.3: Representation of a Bunsen burner flame.

To achieve a precise diagnosis and identification of a flame front, it is essential to gather inherent information about the flame properties by directly collecting and analyzing data captured from the flame. Fortunately, flames naturally emit electromagnetic radiation. Ballester and Armingol [17] have provided a concise summary of the phenomena that make flames spontaneously emit electromagnetic radiations. According to the authors, such emissions can result from the presence of solid particles (e.g., soot or ash), which generate a black body spectrum, as well as emissions from H_2O and CO_2 in case of particle-free flames. Additionally, some chemical reactions can produce excited species, a fraction of which reaches equilibrium by emitting light, a phenomenon known as chemiluminescence. The authors have also emphasized that the visible color of the flame is dominated by the emissions from particles (if present) and from chemiluminescence in particle-free flames.

This thesis work focuses on investigating premixed combustion at stoichiometry (Φ = 1) for natural gas fuel and lean (Φ < 1) conditions for hydrogen fuel, resulting in particle-free flames. As a consequence, the emissions are considered to be dominated primarily by chemiluminescence. Therefore, the identification of the flame front was considered to be marked by the chemiluminescence intensity distribution. Chemiluminescence fundamentally comprises two sequential reaction steps [17] : (1) The formation of an excited radical (R^*) from two parent species ($A + B$) and (2) the subsequent spontaneous release of its excess energy to transition back to the ground state, accomplished by emitting a single photon. This two-step reaction has been summarized below:

$$A + B = R^* + \text{others} \tag{2.1}$$

$$R^* = R + h\nu \tag{2.2}$$

The wavelength of electromagnetic species depends on the molecules R. Each radical R^* exhibits one or more emission lines, which can be organized into distinct characteristic bands. The combined contribution of various emitting radicals produces the chemiluminescence spectrum unique to a given flame.

Ikeda et al. [41] employed local chemiluminescence measurements to calculate the thickness of the flame front and define the flame structure. This study conducted simultaneous measurements of the local flow velocity using Laser Doppler Velocimetry (LDV) and the intensity of chemiluminescence emissions from a premixed propane-air flame using Cassegrain optics. Through the digitization of chemiluminescence data and subsequent calculations of pulse duration (t_f) and the intervals between them (t_{int}), a quantifiable measure of flame thickness and the scale of the flame front was successfully derived. This approach enabled the authors to gather structural information about the flame. Subsequently, the non-dimensional Damköhler number (the ratio of the characteristic flow time scale to the chemical time scale) was calculated, which allowed observation of turbulence scales within the flame. For example, an increase in the Damköhler number along the radius of the burner indicated an increase in

turbulence scale due to the thermal expansion of burned gas at the flame front. Data pertaining to turbulence scales can prove especially valuable when examining flames under flashback conditions. It has the potential to provide quantitative definitions for structural aspects such as wrinkles of the flame front. Additionally, the study revealed that the concentrations of excited radicals were directly related to the intensity of chemiluminescence emissions. For example, blue light emission in the premixed flame is primarily attributed to CH^* radicals. Therefore, the presence of an intense blue-colored segment within the flame signifies a notable concentration of CH^* radicals in that particular region. In another investigation conducted by Kojima et al. [18], spatially and spectrally resolved measurements of flame spectra using a Cassegrain mirror system and a grating spectrometer were performed. These measurements were employed to quantitatively analyze the characteristics of chemiluminescent radicals such as OH^*, CH^*, and C_2^* within the reaction zone of a laminar premixed methane/air flame at equivalence ratios ranging from 0.9 to 1.5. This study concluded that strong correlations exist between the peak intensity ratios of OH^*/CH^*, C_2^*/CH^*, and C_2^*/OH^* within the reaction zone and the equivalence ratio. The high degree of correlation observed implied that spatially resolved chemiluminescence measurements can effectively determine the local flame stoichiometry within premixed flame fronts. Therefore, it can be affirmed that the acquisition of chemiluminescence data represents a valuable asset for understanding the flame. This data set encompasses not only the physical attributes of the flame (for example, flame color, flame thickness, and flame shape) but also offers valuable insights into the underlying chemistry (for example excited radical concentration, and associated equivalence ratio) occurring at the flame front.

Nonetheless, with advancements in laser-based measurement techniques for investigating flames, many studies frequently complement chemiluminescence imaging with other two-dimensional laser-based diagnostic techniques, including Particle Image Velocimetry (PIV), Planar Laser-Induced Fluorescence (PLIF), and Mie-scattering visualizations. Two-dimensional (2D) combustion diagnostic techniques are imaging methods that capture a certain cross-section of the flame. These techniques are instrumental in gathering information and drawing conclusions pertaining to the characteristics of those particular flame cross-sections. The subsequent section cites some previous studies to illustrate the insights that can be derived from two-dimensional combustion diagnostic techniques thereby emphasizing their considerable potential.

2.2.2. Two-dimensional combustion diagnostic techniques

Stopper et al. [35] investigated the lean premixed natural gas/ air flame of an industrial swirl burner using laser diagnostics measurement techniques. In this study, the flow field was characterized using Particle Image Velocimetry (PIV). The results from PIV provided both mean and instantaneous flow fields. Figure 2.4 shows a vector plot of the average flow field together with RMS (in grey scales) for a flame at a pressure of p = 3 bar and an equivalence ratio of Φ = 0.59. The burner mouth is on the left side as indicated by two marks. By analyzing the mean flow fields, distinct zones were identified, including the regions of inflow with highest flow velocities, the inner recirculation zone (IRZ) which appears to extend back into the burner mouth, and the outer recirculation zone (ORZ). It was also noted that between the inflow and recirculation zones, shear layers were established as recognized in Figure 2.4 by high RMS values. Additionally, the instantaneous structure of flow fields was also visualized by single-shot PIV measurements. Figure 2.5 shows two examples from a series of measurements at identical operating conditions (p = 3 bar, Φ = 0.59). From these instantaneous measurements, it was noted that the flow field in the inner shear layer was dominated by small-scale vortices. Additionally, these single-shot PIV results showed varying backflow into the burner nozzle. It was observed that while the backflow was relatively slow in Figure 2.5a, in Figure 2.5b vortices located close to the burner mouth generated massive backflow with planar velocities nearly as high as in the inflow region.

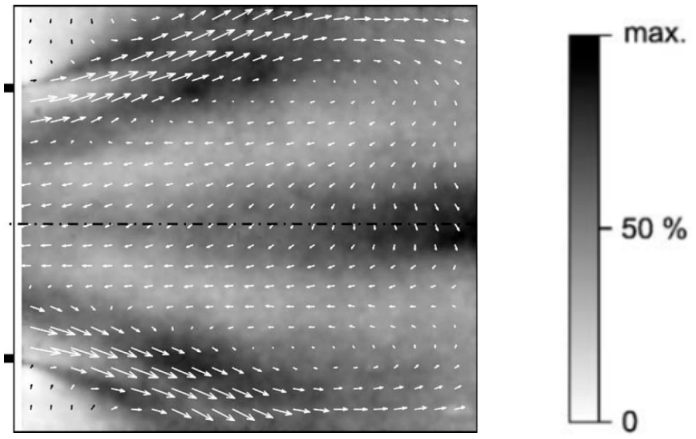

Figure 2.4: Background: mapping of the RMS of the planar flow velocity. Overlay: vector array of the average planar flow field. Grey Scale: Represents the RMS of the planar flow velocity. The pair of marks drawn on the left side of the image indicates the diameter of the burner exit. Adopted from Stopper et al. [35].

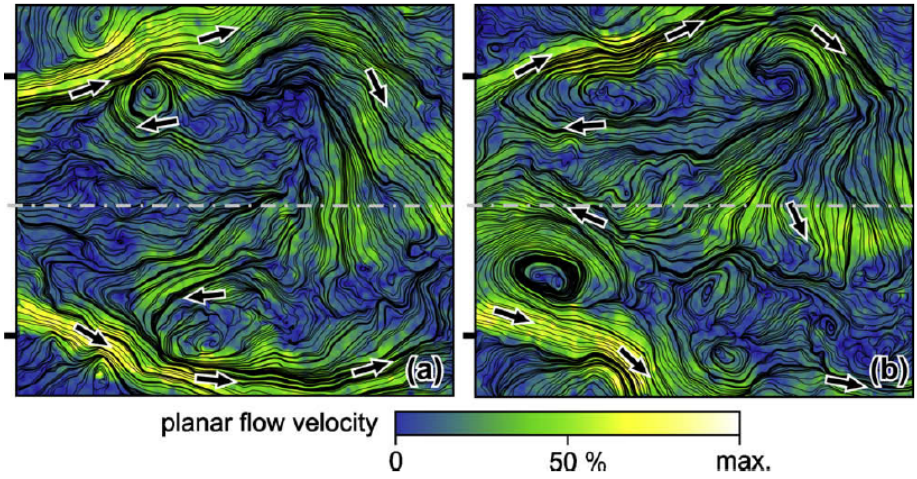

Figure 2.5: Two examples of streamline plots of the instantaneous flow field measured at the same operating point. Arrows indicate the local flow direction. The pair of marks drawn on the left side of each image indicates the diameter of the burner exit. Adopted from Stopper et al. [35].

While insight into the flow fields was extracted using PIV, the identification of the flame front and the overall structure of the flame was achieved through Planar Laser-Induced Fluorescence (PLIF) imaging of OH radicals. The PLIF imaging technique helped identify the concentration and distribution of the target chemical species (OH radicals) consequently contributing to the characterization of flame structure. Figure 2.6a displays the intensity distribution from PLIF imaging for a relatively low absolute pressure of p = 1.5 bar at an equivalence ratio of Φ = 0.53. From the obtained intensity distribution (Figure 2.6a), the cold inflow of unburnt fuel/air mixture was identified by the dark region and the flame front was recognized by the steep gradient from this dark inflow region to the fluorescence maximum. Furthermore, the inner and outer recirculation zones were identified using medium and low LIF intensities. Figure 2.6b shows the intensity distribution from PLIF imaging for a higher absolute pressure p = 4 bar at an equivalence ratio of Φ = 0.50. At this elevated pressure, the PLIF image clearly revealed a noticeable increase in corrugations and fragmentation. The study also pointed out isolated flame front fragments indicating the occurrence of local extinction and spontaneous ignition regions. Additionally, after examining the distribution of OH radicals under two distinct operational conditions (low and high pressure), the study concluded that higher concentrations of OH are more frequently present in the inner shear layer than in the outer one when pressure is raised.

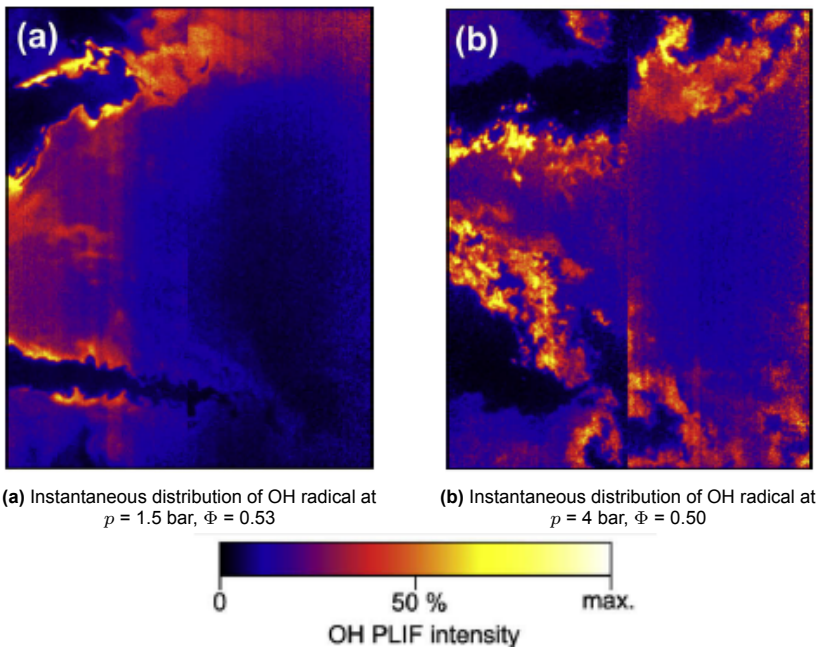

(a) Instantaneous distribution of OH radical at p = 1.5 bar, Φ = 0.53

(b) Instantaneous distribution of OH radical at p = 4 bar, Φ = 0.50

Figure 2.6: PLIF images at two operating conditions. Each figure is a composite of two different laser sheet positions imaged at different points in time. Adopted from Stopper et al. [35].

This study demonstrates that information from two-dimensional laser-based diagnostic techniques can effectively provide insights into flame structure. They enable the identification of various zones within the flame structure, the location of flame fronts, and even the detection of features such as increased corrugations in the flame front.

Another study was conducted by Ebi et al. [8] on boundary layer flashback of methane-hydrogen air flames. The investigation was performed using an optically accessible swirl burner installed in a high-pressure test rig. The swirl burner was equipped with an axial swirler and had a cylindrical center body attached to it within the mixing tube. As for the diagnostic procedures to characterize the flame propagation pathway and the flame shape at the onset and during flashback events, high-speed chemiluminescence (CL) imaging and PLIF imaging of the OH radicals were employed. The flashback was triggered first by establishing a lean flame at the desired operating condition, followed by increasing the equivalence ratio. Figure 2.7 displays the results of high-speed chemiluminescence imaging. It should be noted that the direction of mixture (fuel+air) inflow is from the left to the right in each image. The images from the right to the left show the upstream propagation of flame with increasing time. As can be seen from Figure 2.7 the flame propagates along the cylindrical rod. The flashback appears to be led by small-scale flame bulges oriented toward the incoming flow, as indicated by the yellow arrows. In other words, the flame propagated counter to the predominant swirl direction of the bulk flow, represented by the red arrows. Furthermore, the instantaneous and mean flame shapes were also obtained from PLIF imaging of OH radicals as shown in Figure 2.8. The intensity distribution of OH radicals depicted a wedge-shaped flame with a sharp leading edge propagating in an axial-radial plane above the cylindrical center body. This characteristic is typically associated with straight channel flashbacks, as opposed to high swirl flame flashbacks, which tend to exhibit a more pronounced convex shape. Therefore, the study proposed that the observed flashback can be conceptually regarded as non-swirling Boundary Layer Flashbacks (BLF) occurring in a channel wound around the center body, resembling a helical coil with flow-flame interaction being driven by the same mechanisms as those in non-swirling BLF. As a result, this study suggested that the models developed for non-swirling BLF should also be applicable to cases where a swirl burner is equipped with a cylindrical center body.

Based on the conclusions drawn from this study, it can be inferred that two-dimensional combustion diagnostic techniques have the potential to enhance existing combustion models by offering valuable

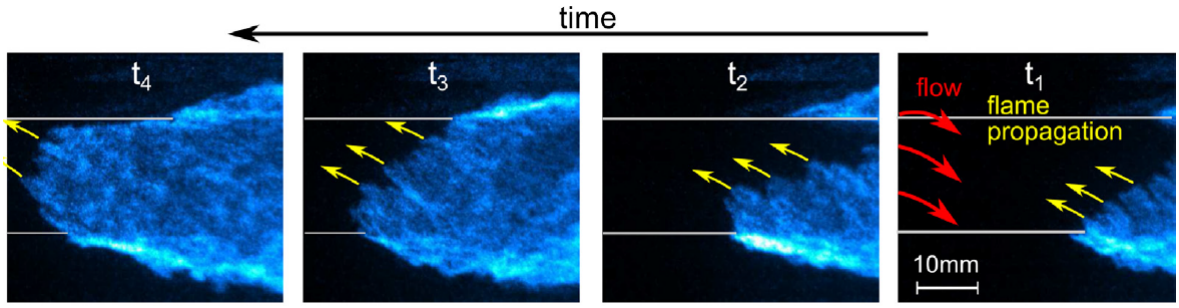

Figure 2.7: CL image sequence showing flashback at equivalence ratio of $\Phi = 0.7$ with 70% of hydrogen and 30% of methane by volume fraction for a Reynolds Number of Re = 3 $\times 10^4$. Adopted from Ebi et al. [8]).

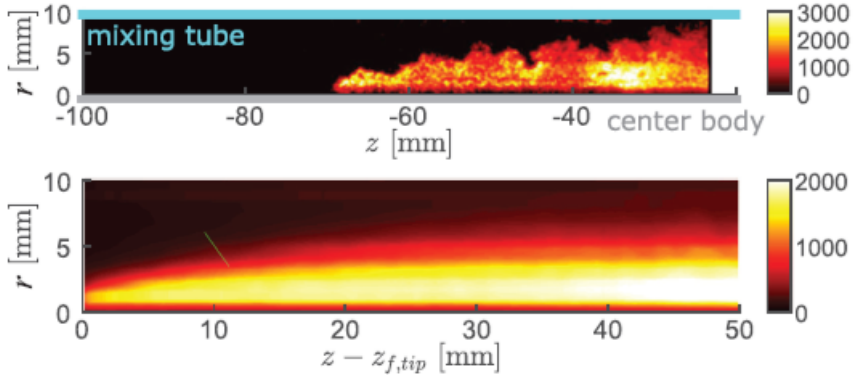

Figure 2.8: PLIF image of flame at equivalence ratio of Φ = 0.7 with 70% hydrogen and 30% of methane by volume fraction for a Reynolds Number of Re = 3 $\times 10^4$. Top: Instantaneous snapshot. Bottom: Mean flame shape. Adopted from Ebi et al. [8].

visual information.

In the recent experimental study conducted at TU Delft by Willems [16] the flame front was characterized using the planar Mie-scattering visualization technique. Mie-scattering occurs when light is elastically scattered by particles with sizes similar to or larger than the incident light's wavelength. In this study, Alumina tracer particles with a mean diameter of 1μm were introduced into the flame. The variations in seeding particle densities before and after the flame front result in different light scattering intensities. This information allowed for identifying the flame front between different seeding particle densities. To acquire a 2D velocity field in a planar cross-section of the flame PIV was used. One of the experiments in this study aimed to visualize the flashback process of a 100% Dutch Natural Gas flame at an equivalence ratio of Φ = 1. Figure 2.9 displays the unconfined flashback process using Mie-scattering images of a turbulent natural gas flame and corresponding velocity field. Unconfined flashback denotes the onset of flashback, where the flame is propagating from outside the burner tube to inside.

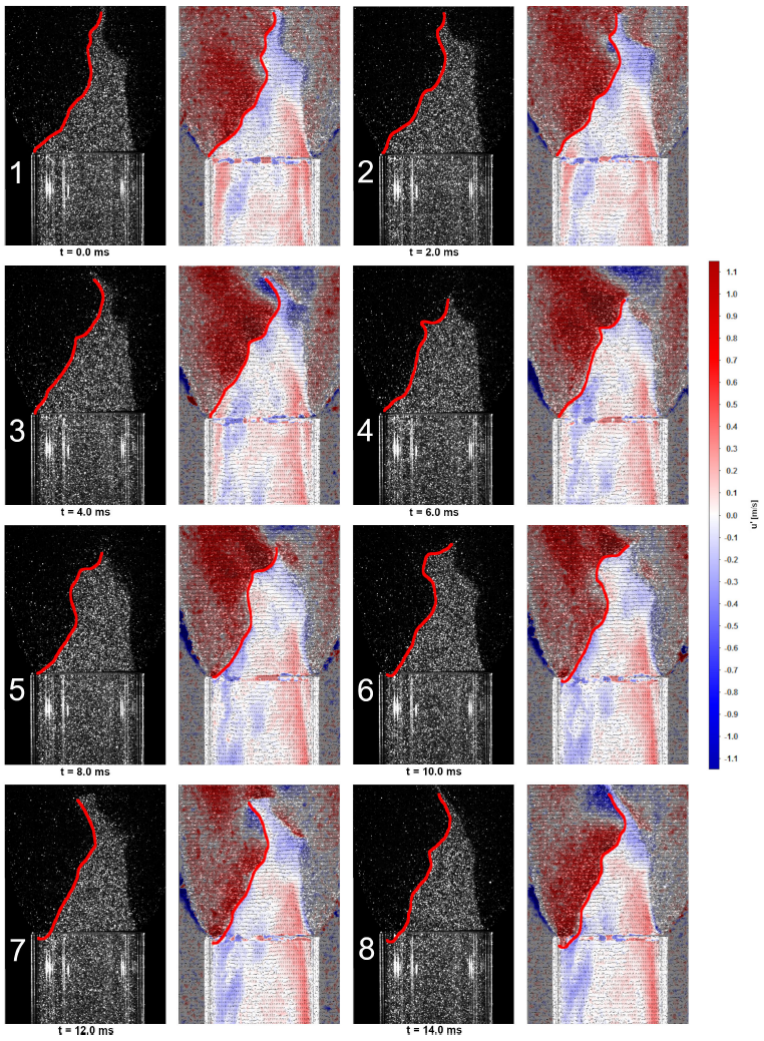

Figure 2.9: Visualisation of the unconfined flashback process for a stoichiometric (Φ = 1) 100% natural gas flame. Adopted from Willems et al. [16].

In Figure 2.9 eight sequential image pairs are shown, each with a time interval of 2 ms. Each image pair comprises a Mie scattering image on the left-hand side and the corresponding axial velocity fluctuations $u^{'}$ on the right-hand side. In the axial velocity fluctuations images, the red and blue areas denote positive and negative velocity fluctuations, respectively. A red line has been used to indicate the flame front. Upon reviewing these eight sequential image pairs, it becomes evident that the flashback originated here from the left side of the burner.

Based on the results obtained from the aforementioned studies, it can be inferred that 2D measurement techniques such as PIV, PLIF imaging, and Mie scattering visualization provide valuable insights into flame behavior and, consequently, the combustion process. However, it is essential to acknowledge that combustion is inherently three-dimensional and flames have a complex three-dimensional structure. Depending exclusively on 2D measurement techniques can potentially lead to the loss of crucial information regarding the nature of the flame. This limitation arises from the fact that measurements are conducted just on a specific cross-section rather than the entire flame. For instance, in Willems study [16] the use of Mie-scattering visualization and planar PIV successfully identified the flame front and obtained instantaneous velocity profiles during the flashback. However, it remains uncertain whether the location where the flashback was first observed coincides with the exact initiation point of the flashback on the burner rim. There is a high chance that a flashback might have been initiated already somewhere outside the observed laser plane or the cross-section of the flame.

Acknowledging the limitations of 2D measurement techniques observed in the previous thesis work,

the present study aims to address the knowledge gap surrounding flashback by employing 3D measurement techniques. By employing a 3D measurement technique, a complete and detailed representation of the 3D structure of flame can be obtained. With this enhanced understanding of the three-dimensional structure of the flame, it will become feasible to accurately identify the specific region on the burner rim where the flashback initiates. Additionally, this will enable the explicit observation and analysis of any distinctive flame feature associated with the phenomenon of flashback.

The present work, therefore, applies the three-dimensional measurement technique of Computed Tomography to reconstruct and determine the entire 3D structure of flame. In many fluid flow-related studies, Computed Tomography (CT) is performed by extending existing 2D measurement techniques such as Particle Image Velocimetry (PIV). This method, known as tomographic-PIV, involves recording particle images from an illuminated volume taken from multiple viewing directions simultaneously, which enables the reconstruction of the 3D light intensity distribution [7]. Fortunately, for flame reconstruction, the need for laser illumination of tracer particles can be eliminated, due to the presence of chemiluminescence of the flame. Chemiluminescence is a reliable indicator of the flame front (as was also explained in Section 2.2.1) and when its intensity distribution is resolved in the reconstruction process, it holds the potential to provide information related to flame features such as propagation, wrinklings, vortex formation, and breakdown. As a result, the present study focuses on reconstructing the chemiluminescence of the flame, and thus, the measurement technique is referred to as Computed Tomography of Chemiluminescence (CTC). In the subsequent section, Section 2.2.3, the focus lies on elaborating the fundamental working principles involved with CTC.

2.2.3. Computed tomography of Chemiluminescence (CTC)

Computed tomography of chemiluminescence is a diagnostic technique that reconstructs the chemiluminescence intensity distribution from a flame, thereby providing its 3D structure. The measurement is carried out in two steps [22]. Initially, images (projections) of the target flame are acquired from multiple angles (viewing direction) either in a sequential manner (by rotating a single camera around the flame to capture images) or simultaneously (using multiple cameras to capture images at the same time). In the second step, these acquired images are used as input for the reconstruction algorithm. The reconstruction algorithms can be divided into two main categories: analytical and algebraic type [43]. Analytical reconstruction algorithms, like filtered back projections typically require multiple low-noise views to achieve successful reconstruction. This requirement limits their applications for practical cases with limited optical accessibility (limited angular range). In contrast, iterative algorithms can yield good-quality reconstruction results for cases where limited data tomography is the only feasible option such as in combustion chambers.

In an algebraic approach the measurement volume (target flame) is discretized as 3D cubical elements known as voxels (essentially 3D counterparts of pixels) with intensities *E(X, Y, Z)*. The projection of light intensity *E(X, Y, Z)* onto the image pixel (x_i, y_i) yields the pixel intensity $I(x_i, y_i)$ (known from the recorded images) [7]. Hence, the recorded pixel intensity represents the integrated object intensity $E(X, Y, Z)$ along the corresponding line of sight. This relationship can be expressed as a linear equation, as shown in Equation 2.3:

$$\sum_{j \in N_i} w_{i,j} E(X_j, Y_j, Z_j) = I(x_i, y_i) \tag{2.3}$$

where N_i corresponds to the number of voxels intercepted along the line of sight. The weighing coefficient $w_{i,j}$ characterizes how the intensity distribution $E(X_j, Y_j, Z_j)$ of the j^{th} voxels contributes to the pixel intensity $I(x_i, y_i)$. It is calculated using the calibration data by considering the volume where the voxel intersects the line of sight (accounting for the cross-sectional area of the pixel) and normalizing it with the voxel volume. Figure 2.10 depicts the imaging problem (Equation 2.3) through a simplified diagram.

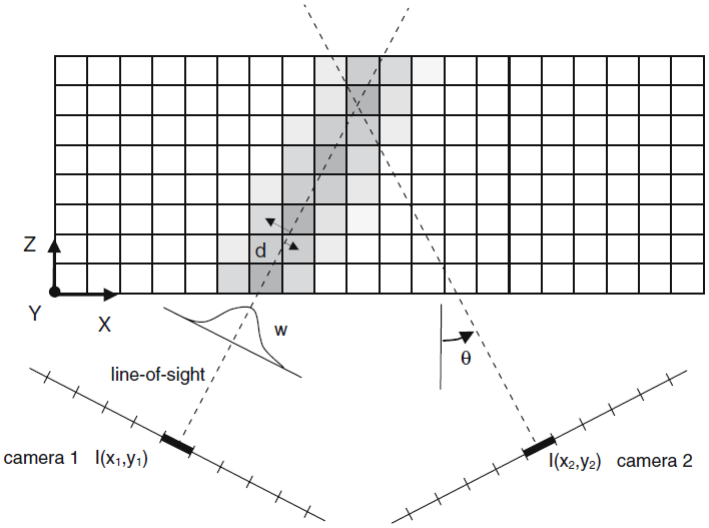

Figure 2.10: Illustration of imaging model employed for tomographic reconstruction. In this top view measurement volume (object) is represented by the 2D array of voxels and the image plane is described by the line of pixel elements. The gray level indicates the value of the weighing coefficient ($w_{i,j}$) in each of the voxels with respect to the pixel $I(x_i, y_i)$. Adopted from Elsinga et al. [7].

In the aforementioned imaging equation Equation 2.3, the pixel intensities ($I(x_i, y_i)$) and weighing coefficient ($w(i, j)$) are the known values whereas the voxel intensities remain unknown. Moreover, the number of unknown variables exceeds the number of known variables, making tomographic reconstruction an under-determined inverse problem. Calculating the inverse of the weighing coefficient matrix becomes impractical due to its substantial size, influenced by both the number of voxels and the amount of projection data. Consequently, employing direct algebraic techniques such as taking an inverse, is unfeasible for solving this challenge [43]. Therefore, algebraic iterative algorithms are required. The iterative approach involves the computation of intensities for these unknown voxels by incorporating predefined convergence criteria to attain an optimal solution, thereby ensuring an accurate representation of the object's (reconstruction) domain. Among the frequently employed algebraic iterative techniques are the Algebraic reconstruction technique (ART) and the Multiplicative Algebraic Reconstruction technique (MART). Mathematically the primary distinction between these two iterative schemes lies in the computation of correction factor or error or updating term.

The optimal solution by algebraic iterative methods is provided by back-projecting a diminishing error into the reconstruction domain until a convergence criterion is met. In the context of this work, simple criteria based on the number of iterations were used similar to the approach used by Verhoeven [6]. Equation 2.4 describes a relaxed ART algorithm, where μ is the relaxation parameter.

ART :

$$E(X_j, Y_j, Z_j)^{k+1} = E(X_j, Y_j, Z_j)^k + \mu \frac{I(x_i, y_i) - \sum_{j \in N_i} w_{i,j} E(X_j, Y_j, Z_j)^k}{\sum_{j \in N_i} w_{i,j}^2} w_{i,j} \tag{2.4}$$

The difference between measured pixel intensity and the projection of the current object ($I(x_i, y_i) - \sum_{j \in N_i} w_{i,j} E(X_j, Y_j, Z_j)^k$) when multiplied by weighing coefficient and relaxation factor in Equation 2.4 denotes the correction factor. The iterative process of the MART iterative scheme is outlined in Equation 2.5.

MART :

$$E(X_j, Y_j, Z_j)^{k+1} = E(X_j, Y_j, Z_j)^k \left(I(x_i, y_i) \Big/ \sum_{j \in N_i} w_{i,j} E(X_j, Y_j, Z_j)^k \right)^{\mu w_{i,j}} \tag{2.5}$$

In the MART algorithm, the update is conducted by taking the ratio of the measured pixel intensity to the projection of the current object, raised to the power of the relaxation factor multiplied by the weighting coefficient as can be seen in Equation 2.5. In both the algorithms an iteration is considered to be completed once all the projections have been considered.

The selection of the algorithm is determined by the nature of the target object and its impact on the reconstruction quality. For relatively smoother objects, the Algebraic Reconstruction Technique (ART) is favoured, while the Multiplicative Algebraic Reconstruction Technique (MART) is more suitable for objects with steeper gradients [6]. Given the steep gradient characteristics of flames, the Multiplicative Algebraic Technique (MART) has been employed as the reconstruction algorithm in this study.

3

Literature Review

This chapter explores prior studies conducted using Computed Tomography of Chemiluminescence (CTC), examining its application, potential, and advancements within the field of combustion.

To unveil the intricate three-dimensional characteristics of a turbulent propane-air fuel-rich premixed flame, Ishino and Ohiwa [42] employed the CTC technique. They initiated the process by capturing instantaneous images of the target flame simultaneously from forty distinct horizontal viewing directions. This was achieved using a custom-made multi-lens camera equipped with forty lenses and a film roll. Figure 3.1 depicts the schematic representation of the experimental setup, while Figure 3.2 provides a detailed view of the custom-made camera. To achieve the three-dimensional distribution of the chemiluminescence of flame, a total of four hundred CT images were reconstructed from the captured images. The reconstruction was performed using the Maximum Likelihood Expectation Maximization (MLEM) algorithm, and these images were stacked vertically. Figure 3.3 depicts a set of simultaneous images captured by the multi-lens camera. These images provide insight into specific flame sections observed by the individual lens.
Figure 3.4 presents sample of horizontal reconstruction results. Based on these reconstructions, certain observations were made. Notable, thin ring-shaped distributions were identified at the lower segment of the target flame. In the central region, it was evident that the flame front exhibited folding (cusps). This folding phenomenon of the flame front became more pronounced at higher elevations. Upon analyzing these horizontal sections, the observed cusps were found to correspond to ridges on the 3D flame front characterized by low luminosity. Figure 3.5 illustrates the overall shape of the turbulent propane fuel-rich premixed flame from a bird's eye view.

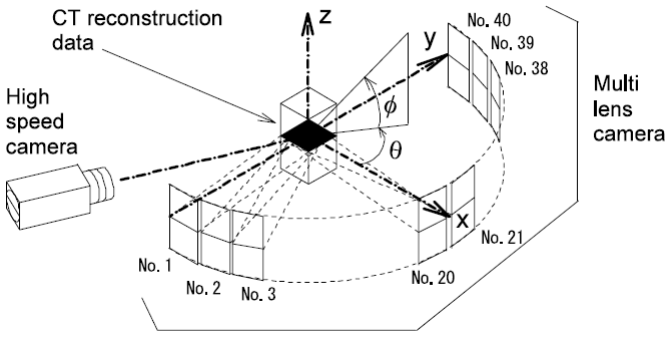

Figure 3.1: Schematic diagram of the experimental apparatus and coordinate system. Adopted from Ishino and Ohiwa [42].

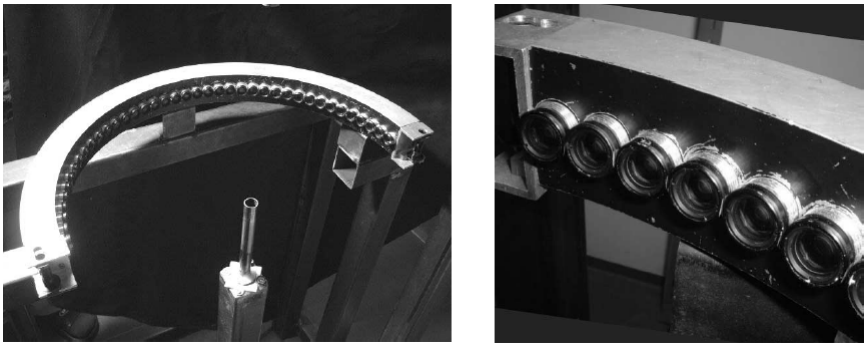

Figure 3.2: Appearance (left) and close-up (right) of multi-lens camera equipped with forty small lenses.Adopted from Ishino and Ohiwa [42].

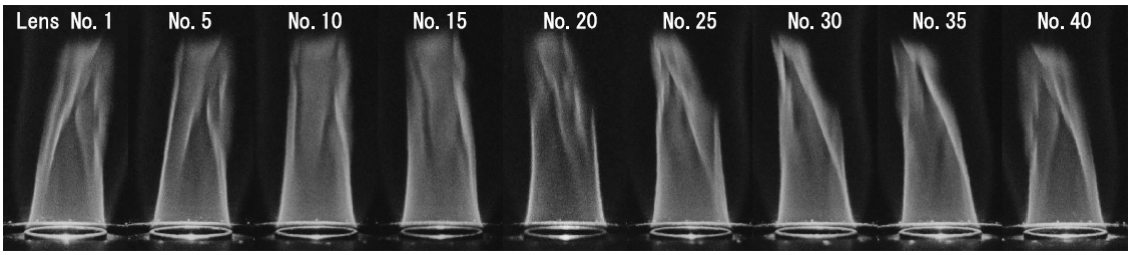

Figure 3.3: Sample set of images taken simultaneously by the multi-lens camera. Adopted from Ishino and Ohiwa [42].

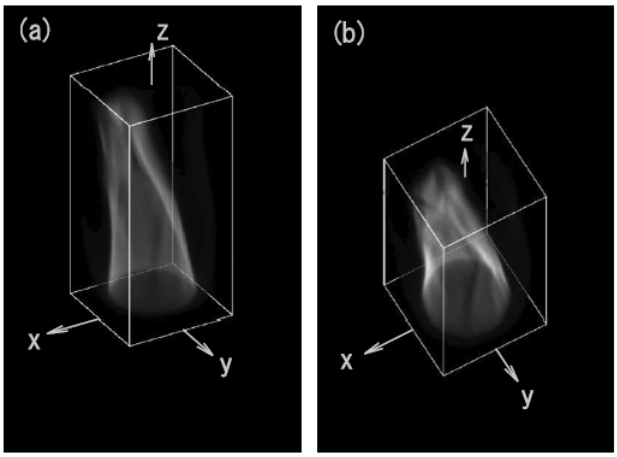

Figure 3.5: Displays of 3D chemiluminescence emission distribution data set. Figure (a) and (b): bird's eye views in the direction of $(\theta, \phi) = (60°, 30°)$ and $(60°, 60°)$. Adopted from Ishino and Ohiwa [42].

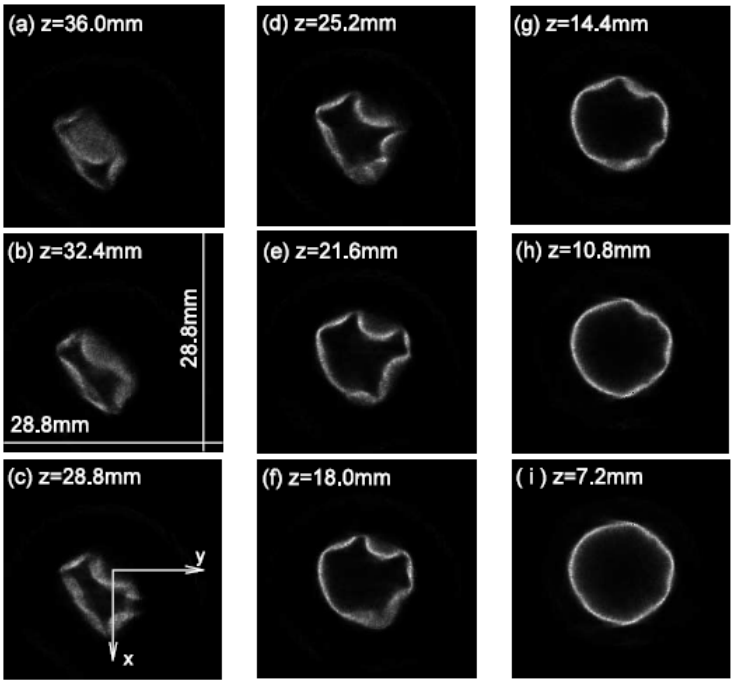

Figure 3.4: Samples of horizontal reconstruction of the turbulent premixed flame of the propane-air rich mixture. Adopted from Ishino and Ohiwa [42].

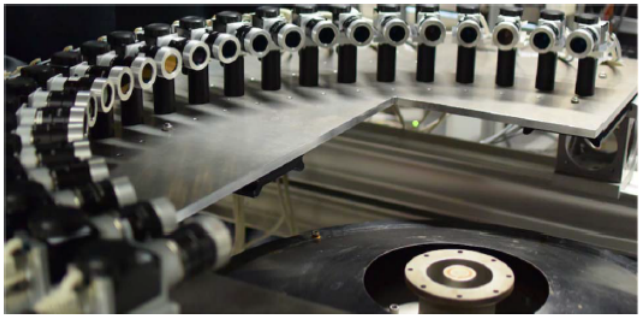

Figure 3.6: CTC setup constituting 24 CCD cameras with filters arranged around the swirl burner. Adopted from Mohri et al. [20].

In a separate investigation by Mohri et al. [20], they employed CTC to reconstruct a highly turbulent methane-air premixed swirl flame. The images were captured from a substantial array of CCD cameras (24 in total) to enable the three-dimensional reconstruction of both instantaneous and time-averaged chemiluminescence fields. Figure 3.6 shows the CTC experimental setup. Figure 3.7 presents the captured images for both instantaneous and time-averaged data. These images correspond to two distinct equivalence ratios (Φ). Flame I depicts a premixed methane-air flame at stoichiometric condition ($\Phi = 1.0$), while Flame II portrays a premixed flame at lean condition ($\Phi = 0.83$).

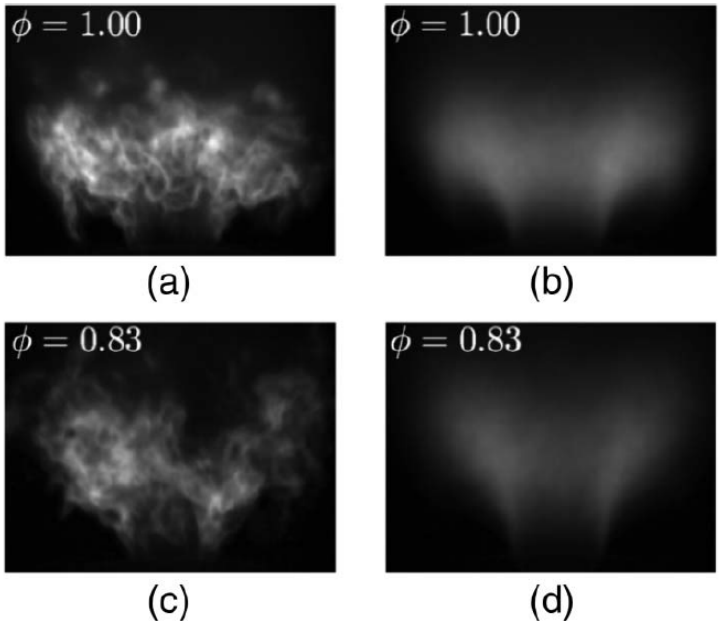

Figure 3.7: Examples of camera views for (a), (b) the stoichiometric Flame I and (c), (d) the lean Flame II, showing (a), (c) instantaneous snapshots and (b), (d) time averages. Camera exposure time is $t_{exp} = 0.4$ ms. Adopted from Mohri et al. [20].

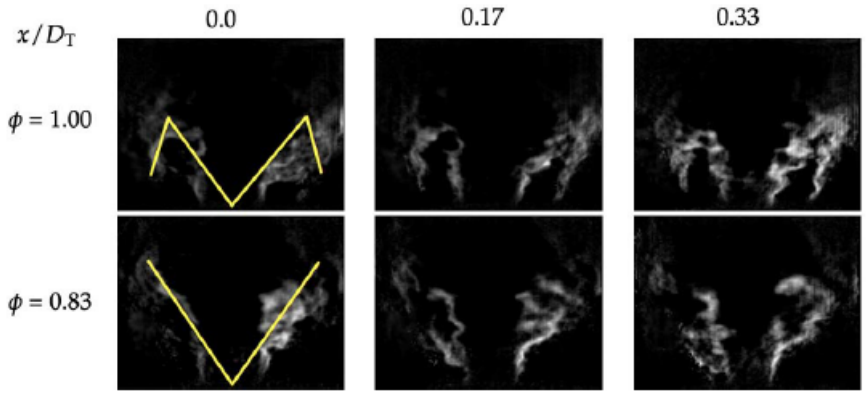

Figure 3.8: Vertical slices from 3D reconstructed chemiluminescence field of instantaneous swirl Flame I and II ($\Phi = 1.0$ and $\Phi = 0.83$, respectively), at the flame centerline relative to the bluff body diameter D_T, $x/D_T = 0$ and two other neighboring vertical planes. The dotted lines illustrate the M and V-shaped flames. Adopted from Mohri et al. [20].

The reconstruction was performed using the ART algorithm. To assess the accuracy of reconstructions, evaluations were conducted for both view-normal and view-parallel perspectives. Notably, comparing the projections of reconstructed images with the original is considered unreliable and should be cautioned against. This caution arises from the likelihood of close agreement between projections from the reconstructed view and the original view, a factor that has been overlooked in some prior studies that reported high resolutions despite otherwise impressive research efforts [32, 5, 21]. Figure 3.8 illustrates the vertical (aligned parallel to the measured views) reconstructed slices of Flame I and II. Additionally, Figure 3.9 illustrates the horizontal (aligned normally to the measured views) reconstructed slices of Flame I and II.

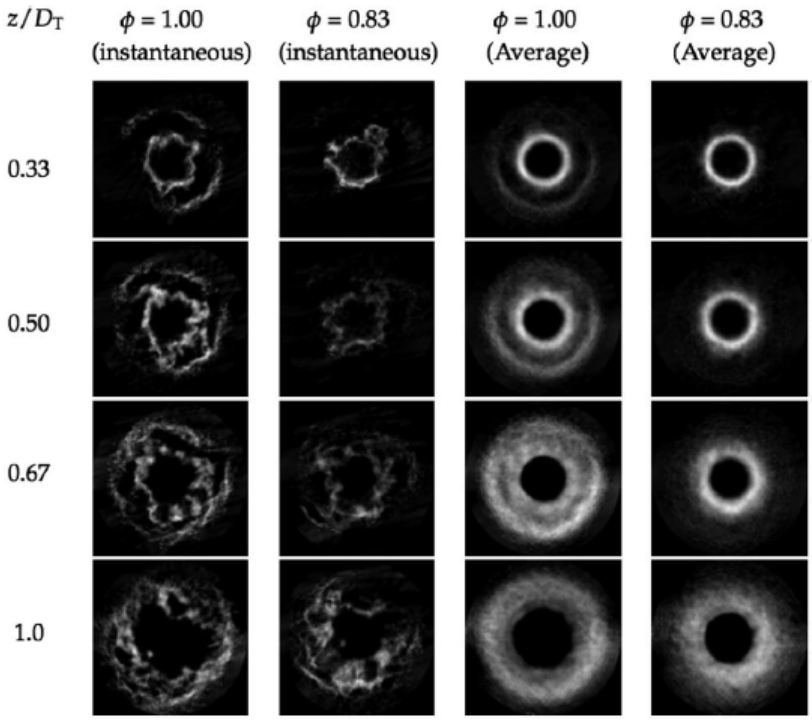

Figure 3.9: Horizontal slices from 3D reconstructed chemiluminescence field of instantaneous and averaged swirl Flame I and II ($\Phi = 1.0$ and $\Phi = 0.83$, respectively), at different heights z above the burner, relative to the bluff body diameter D_T. Adopted from Mohri et al. [20].

Using these reconstructed flame images, intricate structural details were extracted. From figure 3.8 it can be seen that at $\Phi = 1.0$ the flame front exhibited a distinctive folding pattern around the rim, resembling an M shape. Even in figure 3.9 $\Phi = 1.0$ the reconstruction demonstrates that the flame distinctly penetrates into the slow co-flow region and folds down around the rim toward the burner to form a 3D M shape. This was further inferred from a closer inspection of the horizontal plot at z/D_T = 0.33 and 0.5 where the two flame fronts are seen. Conversely, as can be seen from figure 3.8 at $\Phi = 0.83$, the flame exhibited a lower speed, preventing the formation of the folding pattern, and thus displaying a V-shaped burning configuration instead. Additionally, the analysis of horizontal slices from the reconstructed field revealed a notable increase in wrinkling as the height above the burner increased.

Menser et al. [19] employed CTC to reconstruct non-swirl stratified methane-air flames in an instantaneous manner (employed 30 CCD cameras) using ART algorithm and qualitatively compared these results with Direct Numerical Simulation (DNS) data. Qualitative comparisons were performed, and the authors concluded that the reconstruction technique was effective in capturing flame shapes. For a quantitative comparison, the flame front curvature was computed from reconstructed images and compared with DNS data. The authors found a favorable agreement between the two data sets. Nonetheless, it is important to highlight that, despite the utilization of 30 CCD cameras, line artifacts (line streaks) were introduced into the reconstructed image reducing its quality. Addressing this issue, Unterberger et al. [4] introduced a camera calibration method employing a Genetic Algorithm (GA) and ray tracing implemented within the same experimental setup as Menser et al. [19]. Through this proposed approach, camera parameters were calibrated with sufficient accuracy, leading to the elimination of visible line artifacts. It is worth noting that while the calibration routine effectively eliminated line artifacts, it was unable to rectify radial and tangential lens distortion, a common occurrence in real camera lenses due to their inherent pin-hole assumption. These findings highlight the critical significance of accurate camera calibration based on appropriate assumptions. Such calibration is vital not only for eliminating artifacts and enhancing reconstruction quality but also for maintaining distortion-free images, a crucial aspect in accurately capturing the distinctive features of the target flame.

Tomographic reconstruction of chemiluminescence distribution not only excels in depicting flame shapes but also holds the potential to offer insights into the broader domain of 3D flame dynamics. In a research conducted by Worth and Dawson [30] a single camera and intensifier were used to capture the OH^* chemiluminescence originating from two interacting bluff-body stabilized flames. The mean and phase-averaged chemiluminescence field was then reconstructed using the MART algorithm. This investigation carried out under both steady and acoustically forced conditions marked a significant achievement by capturing the intricate 3D interplay between vortices and flames in industrially relevant configuration. This work fundamentally unveils the intricate complexities of flame dynamics which would otherwise remain obscured when employing conventional planar measurement techniques.

Recognizing the potential of the CTC technique and its capacity to provide detailed information, numerous studies are currently dedicated to refining the method for faster and improved reconstruction outcomes. For example, researchers have explored the concept of stacking reconstructed 2D horizontal slices to create an entire 3D structure, aiming to minimize memory usage [42, 14]. Additionally, there have been advancements in the development of improved tomographic algorithms. Martins et al. [11] used an enhanced Evolutionary Reconstruction Technique (ERT) based on a genetic algorithm to reconstruct both instantaneous and time-averaged three-dimensional fields of CH^* chemiluminescence (indicating flame front) and Na emission from NaCl dissolved in the liquid solution (indicating hot spray-flame products). This reconstruction was carried out using 29 cameras, with 15 dedicated to CH^* chemiluminescence and 14 cameras dedicated to Na emission. The authors have reported successfully achieving a detailed depiction of flame morphology, capturing regions involving mixing and interaction between the flame front and the spray stream. To enhance the reconstruction algorithms, numerous researchers have integrated artificial intelligence techniques. Jin et al. [44] introduced a Convolutional Neural Network (CNN)-based approach to achieve rapid 3D reconstruction in a combustion system. They initially reconstructed a candle flame using the ART algorithm from projections obtained from 12 simultaneous views. This reconstructed flame was then treated as the ground truth for training the CNN model. The generated flame served as a reference for training the CNN model. Their results demonstrated that the CNN-based model effectively facilitates swift data processing and even enables real-time monitoring of 3D rapid CTC measurements. Zhang et al. [12] also proposed a neural volume reconstruction technique (NVRT) that uses neural networks to represent continuous flame luminosity. The authors have also acknowledged that the network had been trained by 2D flame projections by adopting a Differential Volume Rendering Technique (DVR), thereby eliminating any 3D supervision. Since the method eliminates the need to discretize the object into voxels the authors have confirmed to attain higher computational efficiency from NVRT than ART, especially in cases when high-resolution cameras are used and flame reconstructions of high spatial resolutions are needed. Additionally, the study has reported the ability of NVRT to preserve both high and low-frequency information, apart from being insensitive to random noise.

In conclusion, the referenced literature provides valuable insights into the capabilities of CTC and the attainable results. It is, in fact, the immense potential of this technique that has motivated numerous researchers to actively pursue its further refinement and enhancement.

4

Experimental setup and methodology

This chapter explores the experimental configuration employed in this study, offering an overview of the specific experimental scenarios that have been the primary focus of the work and the associated methodology.

The CTC experimental setup consists of a set of detector units (optical instruments) as a part of the imaging system, a burner, and a CT algorithm used to reconstruct the intensity field of the flame. The forthcoming section describes the imaging system highlighting the different imaging components involved.

4.1. Imaging system

In the present thesis, the imaging system consists of imaging software, a set of detector units, a programmable timing unit (PTU), and a computer.

4.1.1. Imaging software

LaVision's DAVIS 8.3.1 has been used as the imaging software for image acquisition, processing, and reconstruction. Utilizing DAVIS was crucial for the successful execution of the CTC experiments because it offers an indispensable tomographic module containing the selected CT algorithm MART eliminating the necessity of developing any separate reconstruction code.

4.1.2. Detector units

The quality of the results of the CTC experiments greatly depends on the input provided (captured images) therefore it was crucial to carefully choose the optical instruments for the setup. Previous studies have used either a large number of cameras [42, 20, 19] or a smaller number of these detector units combined with lenses and mirrors [14, 13]. However, in practical applications, combustion chambers frequently encounter optical constraints, making it challenging to install a high number of detector units for monitoring the instantaneous combustion process. Consequently, it becomes imperative to design a setup that strikes a balance between the number of detector units and the quality of results they can deliver. Therefore, this thesis focused on the development of a limited-view tomography setup. Six cameras were chosen as the sole detector units positioned around the flame to capture images from six distinct views. However, prior to settling on the number of cameras (which was based on availability), a critical consideration was to determine the type of cameras that would guarantee good-quality image acquisitions.

Constructing a CTC setup, even with a limited number of views, necessitates having more than three detector units, which, in this case, are the cameras. To maintain cost-effectiveness, a viable approach is to employ commercial cameras such as GoPro instead of more expensive scientific cameras. However, it was crucial to assess whether the chosen GoPro cameras could deliver high-quality raw images of the target object. This consideration is of utmost importance in ensuring the overall success and accuracy of the CTC experiment. For this, the specifications of the Hero 7 GoPro camera were assessed.

The Hero 7 GoPro camera features a CMOS type 6.17 mm $\times$ 4.55 mm sized sensor. It has an inbuilt wide-angle lens with a fixed f-stop of $f\# = 2.8$. This inherent wide-angle lens in the camera however causes the captured raw images, i.e., images taken without any filter or additional correction, to undergo significant fisheye distortion. The raw images are saved in both .gpr (GoPro raw) and .jpg image format. Fortunately, the presence of fisheye distortion can be corrected by switching the field of view (FOV) mode from default wide FOV to linear FOV. This change likely involves an internal calibration, which effectively corrects the distortion. Nevertheless, it is important to note that this switch in FOV mode comes with a trade-off: the images are no longer preserved in their original raw format. Instead, they are automatically saved in a compressed .jpg image format, owing to the internal processing carried out by the camera when adjusting the FOV. Indeed, the formatting of raw images in this manner can have significant implications for the accuracy and quality of image data, which is highly undesirable in CTC experiments that heavily depend on precise image data. The fisheye distortion correction and subsequent change in image format from .gpr to .jpg could have introduced potential artifacts or loss of information, compromising the reliability and effectiveness of the CTC experiments.

Figure 4.1 illustrates the difference between an image captured in wide FOV mode with the presence of fisheye distortion and an image captured in linear FOV mode.

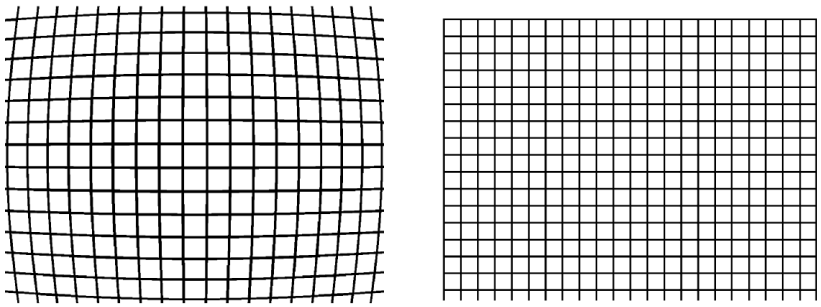

(a) Image captured in wide FOV mode showing fisheye distortion

(b) Image captured in linear FOV mode without fisheye distortion

Figure 4.1: A visual comparison showcasing the difference between an image captured in wide FOV mode and linear FOV mode.

Further, during video recordings GoPro employs a default auto mode of video stabilization which leads to cropping of 5% on each side of the video frame (resulting in a total cropping of 10%) during the capturing process. By applying this stabilization method the camera compensates for unintended movements or vibrations during recordings, resulting in smoother and more stable video footage. In the context of this work, the presence of such stabilizing features is considered highly undesirable because the primary goal is to reconstruct instantaneous flame images in a way that allows for the observation of intricate flame features and associated dynamics. The cropping and stabilization process introduced by GoPro's default video stabilization could potentially lead to the loss of critical details in the flame images, impeding the accurate analysis and observation of the flame's characteristics. Therefore, for this specific study's objectives, it was crucial to avoid using this stabilizing feature to ensure the reliability of the flame image reconstructions. While there is an option to disable the stabilization feature in the camera, this option is available for a limited number of spatial resolutions, and each resolution is associated with specific frame rates, the field of view (wide FOV and linear FOV), and aspect ratios. In other words, not all video settings support turning off the stabilization feature, which may have restricted the flexibility in choosing the desired combination of spatial resolutions, frame rates, field of view, and aspect ratio when attempting to disable the stabilization for specific recording purposes. In addition to the built-in stabilization feature, the GoPro camera was deemed unsuitable for the current flame imaging application since the shortest available exposure time (integration time) was 260.41 μs. For capturing instantaneous flame images in the context of this present application, such a long exposure time would have resulted in an averaged flame image thereby reducing the chances of extracting intricate flame features such as wrinkles. Furthermore, it was observed that the lowest available exposure time could have only been accessed at a single recording frequency of 240Hz. Moreover, this recording frequency was accessible only at lower resolutions.

Besides, even in case the available Hero 7 GoPro cameras did not have these constraints, there would have been limitations in the methods of operating these cameras. The GoPro cameras can be operated through physical controls, the GoPro mobile app, or a wireless remote. However, physically operating GoPro would not have been viable due to the risk of disturbing a calibrated setup. In contrast, the other two methods would have been suitable options for capturing images in case the primary objective was only image acquisition. Indeed an ideal scenario would have been the compatibility of GoPro cameras with DAVIS. Such compatibility would have streamlined the image acquisition process and facilitated seamless integration with the imaging software particularly concerning image processing and reconstruction.

In conclusion, despite their cost effectiveness and compact size, the significant challenges of image distortion, stabilization, limitations in terms of exposure time, and incompatibility with the imaging software DAVIS made GoPro cameras unsuitable for conducting CTC experiments in this work. As a result, other camera options such as the scientific ones were explored to address these limitations and ensure the reliability of the CTC setup for intended research purposes. Initially, the PCO Imager pro-X 4M was under consideration. This camera model features 2048 $\times$ 2048 pixels, with pixel pitch of 7.4 μm $\times$. Moreover, unlike GoPro, this scientific camera model was observed to be fully compatible with DAVIS and did not possess any inbuilt stabilization mode or distortions in raw image format. Additionally, the camera gave the advantage of flexibility in terms of attaching lenses of choice and operating at different f-stops (f#).

However, it was noted that the scientific PCO cameras were relatively bulky and not compact in size. Given the practical scenario of limited optical access within the combustion chamber, it would be more feasible to install compact-sized detector units. Owing to their reduced spatial occupancy in the chamber the installation of these compact-sized detector units would offer more flexibility in terms of adjusting viewing angles and positions compared to bulkier detector units. The space that a single bulky detector unit might occupy could be efficiently utilized by installing multiple sets of compact detector units. This arrangement could allow for an increase in a distinct number of available views. Therefore, it would be better to have compact-sized cameras with respect to the development of a combustion diagnosis setup. Apart from not being compact in size, the limited availability of these cameras (only 4 cameras were available) in the required quantity further rendered them unsuitable for the CTC experiments in this work. As a result, they were also eliminated as potential options for the setup.

Finally, the limitations of both the commercial Hero 7 GoPro camera and scientific PCO Imager pro-X 4M camera were addressed by the compact Imager LX 2MP cameras featuring 1628 $\times$ 1236 pixels with pixel pitch 4.4 μm CCD sensor. This camera selection offered an added advantage by ensuring a relatively faster reconstruction process since the algorithm only needed to process 2 Mega-Pixels. Furthermore, Tamron 75mm f/3.9 C-mount lenses with a minimum focusing distance of 0.5 m were selected to be attached to the cameras to achieve high-quality images. In total six of these cameras have been used in the setup. Figure 4.2 depicts the physical appearance of the selected Imager LX 2MP camera with a Tamron lens.

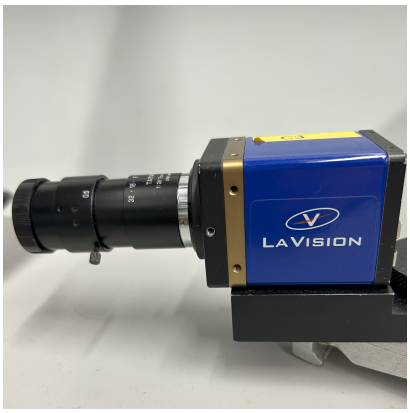

Figure 4.2: Imager LX 2MP camera with attached Tamron lens used in the CTC experiments.

4.1.3. Programmable timing unit

Given that a multi-camera setup is being utilized to capture instantaneous flame images in this study, there was a necessity to synchronize these cameras and ensure simultaneous triggering. For the purpose of synchronization and simultaneous triggering of the cameras, an external component PTU9 was connected to the Imager LX 2MP cameras.

In summary, the cameras were linked to the computer via Ethernet cables and were operated through LaVision DAVIS 8.3.1 software, in conjunction with a PTU9 timing unit, constituting an imaging system.

However, to confirm the suitability of the cameras for conducting the CTC experiments in terms of compatibility with the imaging software and the trigger unit, a small experiment was conducted using four Imager LX 2MP cameras. Figure 4.3 shows the four-camera setup built around a camping gas burner.

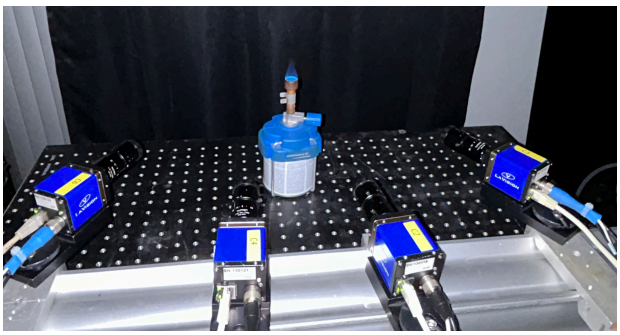

Figure 4.3: Four camera setup around a camping gas burner.

In the experiment the sequential images of premixed flame (propane-butane-air) from the burner were acquired from four viewing directions (as per the positions of four cameras). Images were acquired at different exposure times (such as 166 ms, 116 ms, 66 ms, 60 ms, and 30 ms) to assess the versatility in selecting exposure times. Nevertheless, it was observed that the software tended to become unstable when capturing a substantial number of images at the maximum recording rate of 8 Hz (frame rate). Conversely, when operating at a lower recording rate of 2.5 Hz, the process of acquiring numerous images proceeded more smoothly and without any software crashes. Given that the primary focus of the current experiment was to capture instantaneous flame images, and considering that the employed cameras are not high-speed cameras, it was already understood that recording the temporal evolution of the flame would not be feasible. Consequently, the decision was made to operate the cameras at a low recording rate while sequentially capturing as many images as possible. In addition to confirming the aspects related to exposure times and recording flexibility, the synchronization between the cameras was also verified. Synchronization, in this context, denotes the simultaneous triggering of the cameras, ensuring that they capture diverse views of the flame, corresponding to their respective perspectives, simultaneously. To assess the synchronization, the flame was suddenly extinguished during the ongoing image acquisition process. Subsequently, an examination was conducted to ascertain whether the frame numbers matched across all cameras at the point where no flame image was present. As the frame numbers (at which there was no flame image) across all cameras matched, it was deduced that the cameras were indeed synchronized.

Following the verification of the image acquisition process, a subsequent evaluation of the tomographic-PIV module within the DAVIS software was conducted which involved reconstructing the acquired flame images using the MART algorithm. This test confirmed the module's ability to effectively reconstruct the flame. Hence, it was conclusively affirmed that the components comprising the imaging system are mutually compatible and well-suited for conducting experiments within the scope of this study.

Once the components of the imaging system were established, the attention was directed towards addressing the other crucial aspects required for the execution of the CTC experiment. Consequently, the following section provides details of the burner setup.

4.2. Bunsen burner

For the experiments, a Bunsen burner has been employed. The Bunsen burner, characterized by a simple tubular design with a circular rim, closely resembles the configuration of a premixing tube. This choice was made also to uphold the simplicity of the experimental setup and to concentrate on reconstructing the flame with minimal geometric intricacies. Consequently, the experiments were conducted using a Bunsen burner setup available at the TU Delft Combustion Lab. This setup closely resembles the ones utilized in previous work by Willems [16] with the exception of the cyclone seeder unit, as seeding particles are not required for a CTC experiment. Figure 4.4 presents the schematic highlighting the main components of the Bunsen burner setup. Table 4.1 provides the details of the dimensions of the Burner setup used in the experiment.

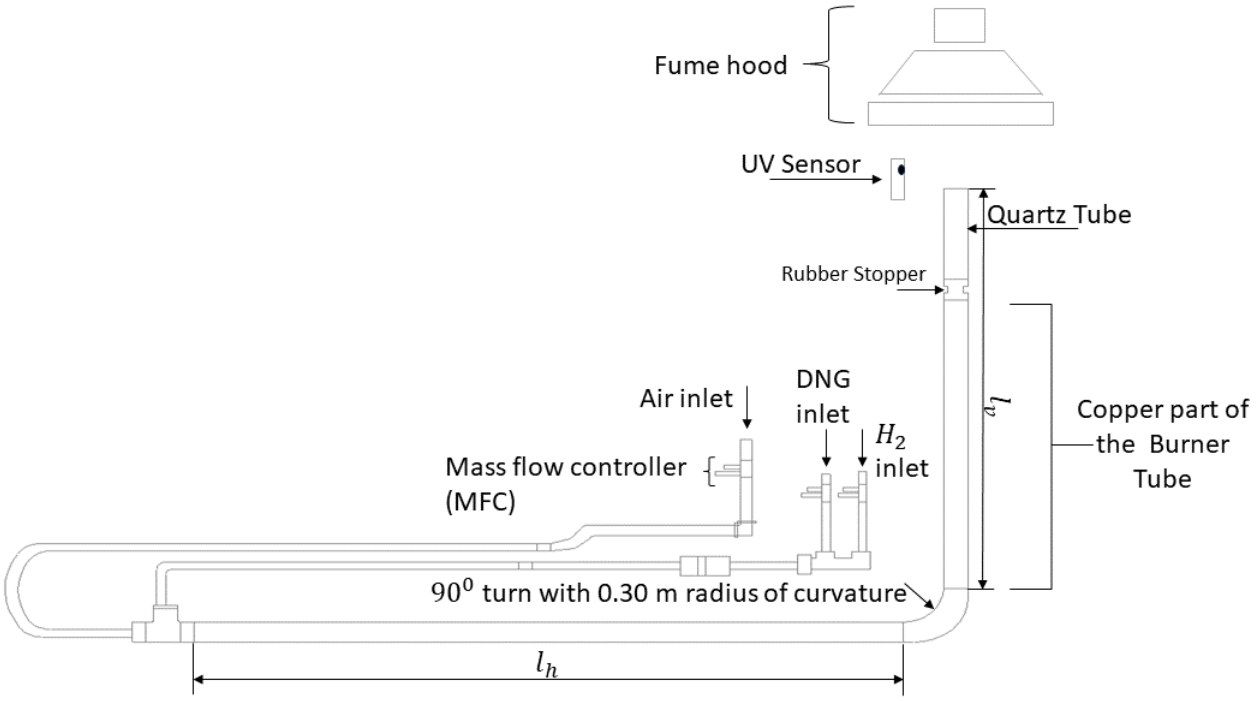

Figure 4.4: Schematic of the burner setup.

Bunsen Burner	**Horizontal tube**	**Vertical tube**	**Final tube**
Inner diameter D_b [mm]	25.0	25.67	25.16
Wall thickness t [mm]	2.0	1.1	1.47
Length l [mm]	2300	1000	219
Material	Copper	Copper	Quartz

Table 4.1: Details of the dimensions of the Bunsen burner setup used in the experiment.

The air and fuel mixture was regulated by three mass flow controllers, with communication established through a computer using a LabView control panel. For visualizing the flashback process optical access inside the tube was required. To simulate this condition just above the burner rim, a quartz tube was attached. In addition to the burner configuration, an external UV sensor was positioned near the rim of the quartz tube. The UV sensor served as a safety mechanism responsible for regulating the opening and closing of the main fuel line. This operation is basically dependent on the detection of the flame by the UV sensor. If a flashback occurs or the flame extinguishes, the UV sensor detects the absence of combustion and discontinues the fuel supply.

Upon finalizing the imaging system and burner to be used, the construction of the CTC setup was undertaken. The subsequent section provides a comprehensive account of the setup, encompassing its construction, reliability, and calibration details.

4.3. Computed Tomography of Chemiluminescence setup

With the installation of six Imager LX 2M cameras around the Bunsen burner, the CTC setup was constructed. Figure 4.5 presents a schematic depicting the camera numbers and arrangement around the burner, referred to as the target in the illustration. The camera numbers are specified as identified by the imaging software DAVIS. The schematic serves to define the angles at which the cameras were positioned with respect to the beam structure and the angles between adjacent cameras. Notably, cameras 1 and 2, being the farthest apart, were positioned at an angular separation of 96°, thus establishing the angular limitations of the entire tomographic setup. The angles were adjusted using a calibration plate installed just above the burner rim. This process ensured that each camera's field of view was optimized to cover the desired range of the flame contributing to accurate image acquisition for the tomographic process. Further details about the calibration plate and image calibration process are provided in Section 4.3.2.

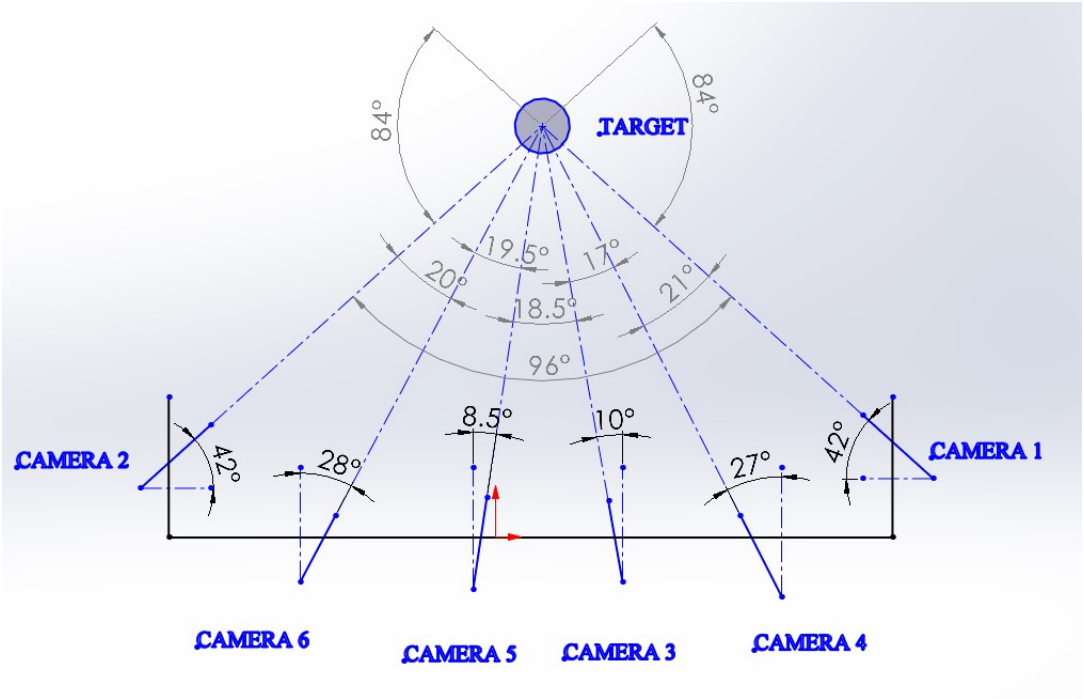

Figure 4.5: Schematic of camera arrangement around the target (Bunsen burner) - Top View.

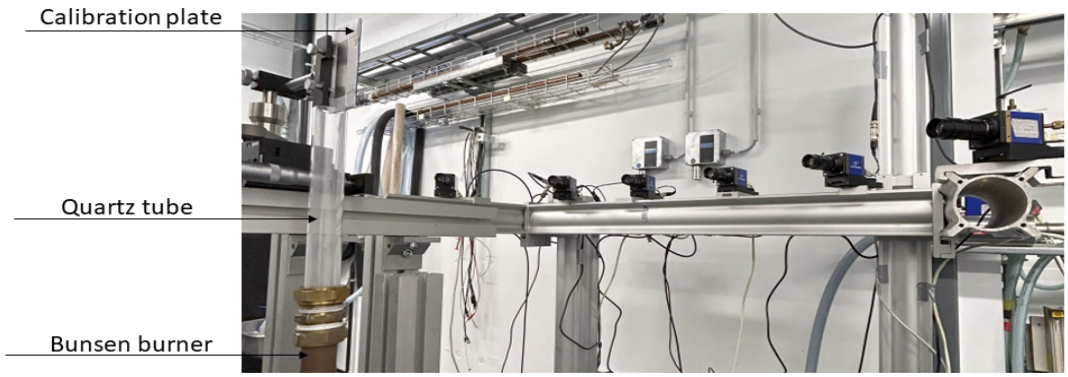

Figure 4.6: Computed tomography of chemiluminescence setup.

After finalizing the positions of the cameras, the focus of each camera was adjusted. To further enhance the focus, the aperture of the camera lens was slightly closed by adjusting the f-number (f#) value to 5.6. This adjustment helped optimize the sharpness and clarity of the captured flame images, ensuring that essential flame details could be observed and reconstructed.

Figure 4.6, presents the CTC setup featuring six cameras arranged around the Bunsen burner with an installed quartz tube and the calibration plate.

4.3.1. Phantom study

In order to evaluate the reliability of the established experimental setup and gain preliminary insights into the reconstruction outcomes, a phantom study was carried out (within the context of flame reconstruction, a phantom denotes a synthetically generated or simulated flame configuration that resembles relevant features of the real flame). The phantom was generated using MATLAB code, illustrating horizontal flame slices that replicate sections of a flame originating from a burner with a circular rim. A Gaussian intensity distribution was assigned to the flame slices to simulate the chemiluminescence emissions from the flame front region. Further, the projections of the phantom were generated at the same 6 camera locations (see Figure 4.5) as in the CTC setup, assuming an ideal lens with no distortion or image noise effect. While the primary source of chemiluminescence stems from the flame front region, it is important to acknowledge the presence of exhaust gases such as water vapor near the flame front. These exhaust gas emissions introduce an additional intensity signal with its own spatial distribution. In fact, this spatial distribution becomes increasingly prominent as one progresses downstream of the flame or farther from the burner rim. Due to the absence of filters such as water emission filters in the employed cameras, the emissions from thermally excited water and other exhaust gases were expected to contribute to the recorded image intensity. As a result, the generated phantom includes the presence of these exhaust gases by integrating intensity distribution (lower levels of intensity distribution compared to the intensity distribution assigned to the horizontal flame slice) around the flame slice, aiming to approximate the anticipated reconstruction results. Nevertheless, it is important to acknowledge that the spatial distribution of both chemiluminescence intensity and exhaust gas emissions could potentially exhibit variations in the actual experimental scenarios. The phantom study serves as an initial approximation of the expected reconstruction outcomes.

The phantoms have been reconstructed using both ART and MART algorithms to illustrate the disparities in the outcomes produced by each algorithm. The spatial resolution, determined based on the sensor specifications and the physical dimensions provided as input to the code, was calculated to be 0.024 mm/pixel horizontally and 0.032 mm/pixel vertically. Two separate phantoms were created: one characterized by a circular shape with wrinkles, having an amplitude of 0.1 mm, and another displaying wrinkles, with an amplitude of 1.5 mm. These selections were made to introduce heightened complexity to the flame further downstream [20] where the flame is less influenced by the structure of the burner exit and tends to have prominent wrinkles and thus understand potential challenges that might come up in the reconstruction process. Both the horizontal slices (phantoms) generated were characterized by a diameter of 25.16 mm and a thickness of 0.5 mm (to define the flame front thickness).

Similar to the reconstruction process in the DAVIS imaging software (used in this study), the phantom study's convergence criteria were also determined by the number of iterations. Each iteration cycle concluded upon accounting for all the projections. Furthermore, the decision regarding the number of iterations was made with careful consideration of achieving an optimal balance between approaching precise reconstruction results and ensuring computational efficiency. Therefore, in the present phantom study, five iterations were performed. Figure 4.7 shows the original phantom with the corresponding result from the MART algorithm and ART algorithm after the completion of all five iterations. The results give an initial idea about the flame structure that can be expected near the burner rim. From visual assessment, it is evident that MART is a more favorable choice compared to ART. This preference arises due to the presence of numerous line artifacts (which can be identified as high-intensity straight line streaks in the reconstructed images obtained from MART and ART algorithms) in the reconstruction results obtained using ART, which could be more pronounced in real experimental outcomes owing to the influence of the exhaust gas emissions. In practical experimental scenarios, it is possible that

even the MART algorithm's reconstruction outcomes could display subtle line artifacts, although their prominence is expected to be notably diminished (as can be seen from current reconstructed phantom results obtained through the MART algorithm in Figure 4.7) in comparison to the artifacts arising from the ART algorithm. Figure 4.8 illustrates another phantom with a flame front characterized by high-amplitude wrinkles resembling a plausible scenario further downstream of the flame. Visual inspection (see Figure 4.8) clearly indicates that again the MART algorithm (despite the presence of minor line artifacts) produces superior outcomes compared to ART. The MART-produced reconstructed phantom wrinkles (As also highlighted by red outlines in Figure 4.8) demonstrate a spatial distribution that resembles the original phantom wrinkles more closely than the ART-produced reconstructed phantom wrinkles. In addition to aiding in the selection of an appropriate algorithm, these phantom simulation results provided insight into the overall reconstructed flame image that can be expected based on the positioning of the six cameras. As evident from the reconstructed images (Figure 4.7 and 4.8), the regions corresponding to the top ($z \approx 35$ mm) and bottom ($z \approx 5$ mm) of the horizontal flame section do not seem to accurately depict the 3D distribution one would anticipate from a flame section situated

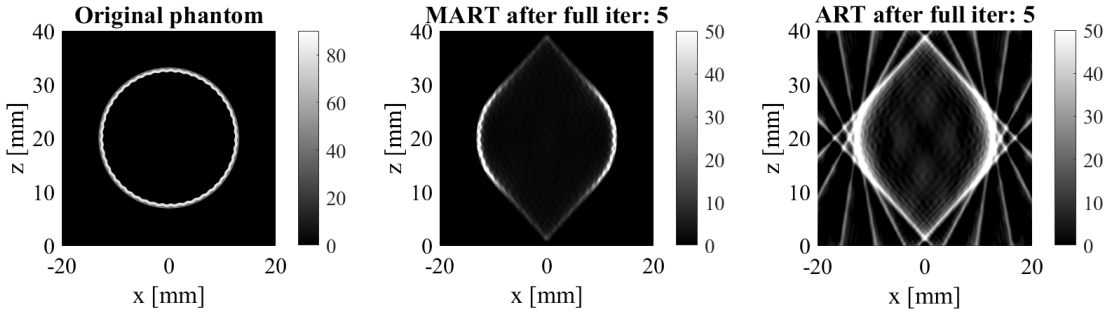

Figure 4.7: Small Amplitude Wrinkled Flames Phantom (resembling section near the exit of the burner): The white intensity distribution corresponds to the flame front in the original phantom, while the faint grey intensity distribution represents the surrounding exhaust gases.

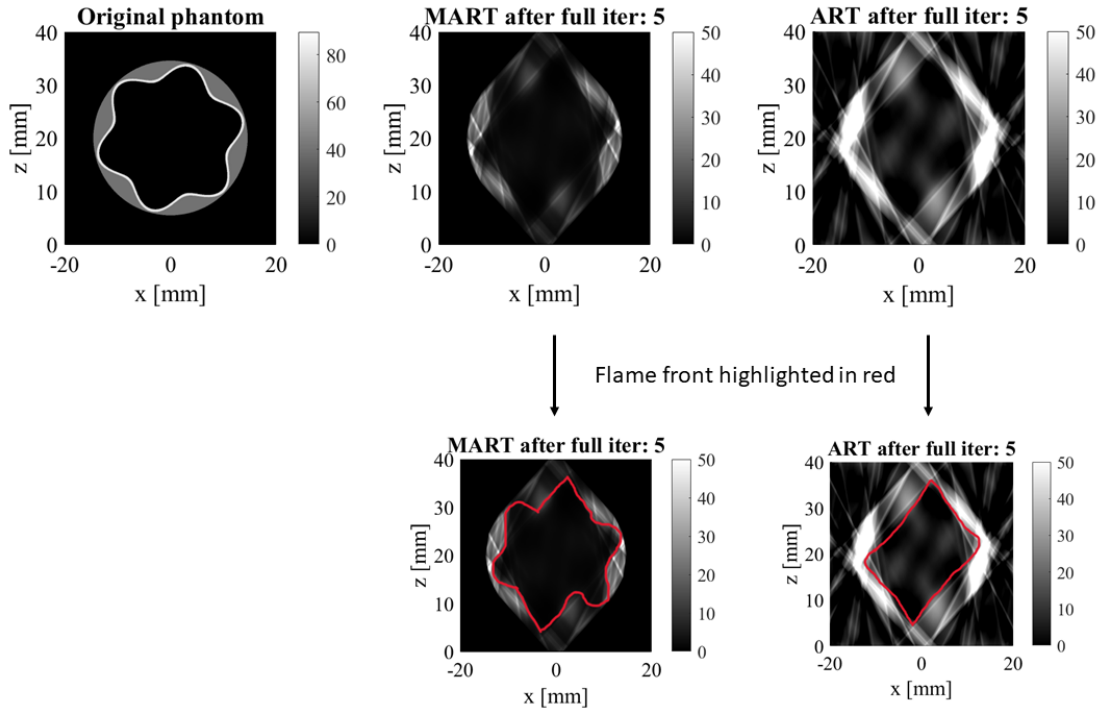

Figure 4.8: Large Amplitude Wrinkled Flames Phantom (resembling section further away from the exit of the burner): The white intensity distribution corresponds to the flame front in the original phantom, while the faint grey intensity distribution represents the surrounding exhaust gases. The flame front has been highlighted in red (visual aid and not a computed quantity).

near or further away from the exit of a burner with a circular rim. Such unexpected 3D distribution near the top and bottom of the horizontal section of flame is due to the absence of cameras directly looking at those sections. In such scenarios where there is extremely limited or no information available regarding a specific section of the object from the image acquisition process, it is possible that the reconstruction algorithm may struggle to converge to an exact solution. Nevertheless, relying on the available intensity data, the algorithm may still generate a 3D distribution of the section through interpolation.

In summary, when comparing the original phantom with the reconstructed phantom, the initial observation suggests that the MART algorithm is more suitable than the ART algorithm for flame reconstruction in the present study. This conclusion is primarily based on two key observations. Firstly, the MART algorithm exhibits fewer line artifacts in the reconstruction output compared to the ART algorithm. Secondly, MART demonstrates a superior ability to reconstruct the flame wrinkles, as evidenced by the closer resemblance in spatial distribution to the original phantom wrinkles when compared to the ART algorithm. Additionally, drawing insights from this phantom study, one can anticipate an unexpected 3D intensity distribution toward the front and back of the reconstructed flame during actual experiments as well. This is attributed to the absence of cameras with a direct line-of-sight at the front and back of the flame even in actual experiments (see Figure 4.5.).

Based on the results of this phantom simulation, it was established that the current CTC experimental setup is capable of delivering reliable results. Consequently, the subsequent phase involved camera calibration in preparation for conducting experiments. The following section outlines the specifics of camera calibration conducted in the present study.

4.3.2. Camera calibration

Camera calibration establishes a relationship between the image coordinates (projections) and object coordinates (reconstruction volume). The camera calibration steps using DAVIS software were performed before and upon completion of the experiments.

For the calibration procedure images of the target calibration plate were simultaneously captured from all six cameras at five different planes above the quartz tube (depth locations throughout the volume) as per the first step of the DAVIS calibration module. The calibration plate featured cross marks (+) with a height of 2 mm, and the distance between the centers of the marks was 2.4 mm. The calibration plate was securely positioned on a mounting assembly featuring a screw gauge, allowing for the translational movements of the plate. Initially, the plate was translated near the center section of the quartz tube, and the value on the screw gauge was noted. It was observed that the center section of the quartz tube corresponded to a 10 mm reading on the screw gauge of the mounting. With this, the first plane location (the starting position of the plate from where it would be translated to the other four locations), approximately positioned at the back of the quartz tube rim corresponded to a value of 0 mm on the screw gauge of the mounting. Subsequently, the plate was translated at four more planes, each at an interval of 5 mm (ΔZ), with the last plane (Plane 5) approximately corresponding to the front of the quartz tube at 20 mm. This sequence of positions ensured a calibration process, covering different sections above the quartz tube (several depth positions throughout the volume). Figure 4.9 illustrates a schematic of the top view of the quartz tube and the five different planes at which the calibration plate was translated. In this schematic, the direction of translation of the calibration plate from the starting position at Plane 1 (first depth location) towards Plane 5 (last depth location) has also been indicated.

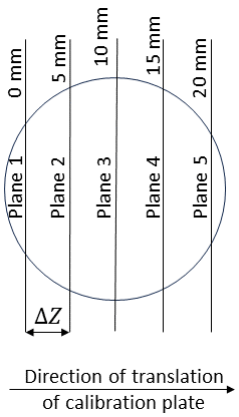

Figure 4.9: Schematic showing the top view of the quartz tube and the position (as per the values noted on the screw gauge of the calibration plate mounting) of five different planes at which the calibration plate was translated.

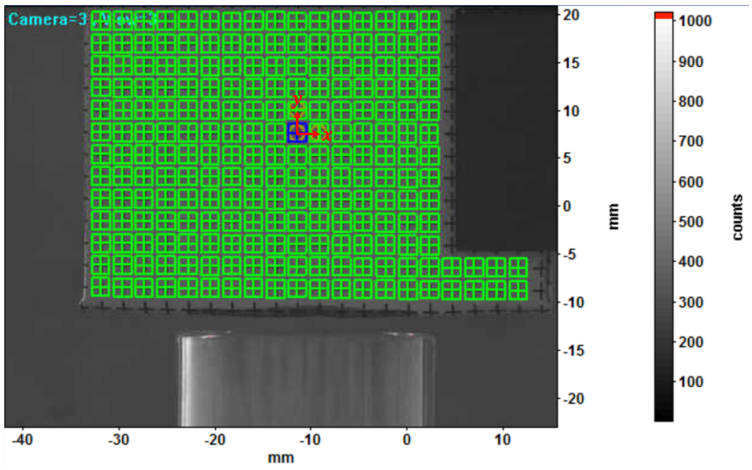

Figure 4.10: View of calibration plate positioned at Plane 3 from Camera Number 3. The green box markings denote the marks identified by the software. The blue box towards the center highlights the chosen origin on the plate from where the x and y coordinates were defined.

Once the images of the plate were captured at different planes following the next step in DAVIS, the origin, and corresponding x and y coordinates were specified by highlighting the cross marks (+) on the plate. Subsequently, the calibration module effectively detected all the cross marks from the images captured at all the planes by all six cameras. With the mark locations of the calibration target known, the next step involved fitting these mark locations or mapping physical space to the image coordinate system using a third-order polynomial function. The calibration process was thus completed establishing the necessary relation between the image coordinates system and the world coordinates system. Figure 4.10 shows the image of the calibration plate positioned at Plane 3 (refer to Figure 4.9 for identifying Plane 3) as captured by Camera 3. The green colored boxes highlight the detected cross marks of the calibration plate by the software. The blue-colored box (towards approximately the center of the plate) marks the origin chosen in the plate from where the x and y coordinates were defined.
For the sake of clarity in presenting both image acquisition (in 2D coordinates) and image reconstruction results (in 3D coordinates), an adjustment was made to the DAVIS 3D coordinate system (not within the software itself). This adjustment was executed in such a way that the center of the rim, the exit, and the center section of the quartz tube aligned with (x, y, z) = (0,0,0) for all the cameras. The results in the later section have been presented in this adjusted coordinate. Figure 4.11 shows the distinction between a 3D measurement coordinate system in DAVIS (as an example specifying the coordinates related to the quartz tube according to calibration results of Camera 3) and a 3D physical coordinate system used to display imaging results later on. The adjustment in the coordinate system was applied for images obtained from all six cameras to maintain consistency in the presentation of results.

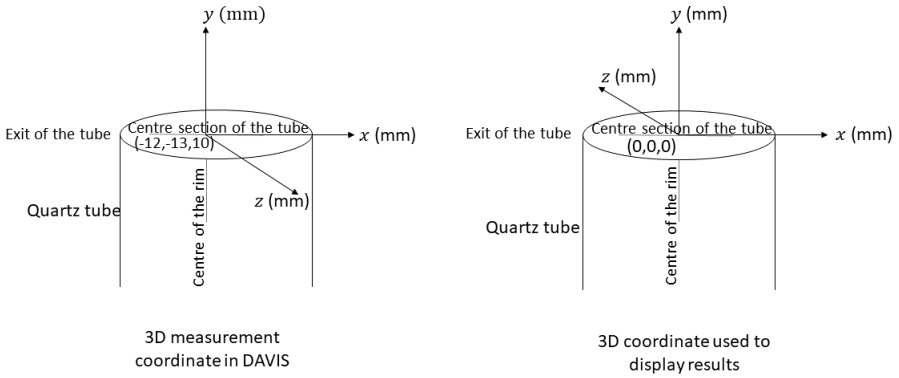

Figure 4.11: Distinction between 3D measurement coordinate as used in DAVIS (left) and 3D physical coordinate system used to display results in the report (right). The DAVIS measurement coordinates related to the quartz tube presented here are according to the calibration results of Camera 3. In both the figures the center of the rim, the exit, and the center section of the quartz tube rim have been indicated.

The calibration was performed for locations above the quartz tube. From this calibration procedure, the field of view (FOV) for all the cameras was obtained. Table 4.2 summarizes the field of view as well as spatial resolutions of all the six cameras. It was not feasible to conduct the calibration inside the quartz tube due to the unsuitability of the available plate for translation at various positions within the tube. However, considering that the cameras employed were not high-speed ones, it was already anticipated that capturing the propagation of flame during flashback inside the quartz tube would not have been possible. Consequently, calibration inside the tube was considered less critical as it would not have significantly impacted the overall calibration process and objectives of CTC experiments within the scope of the present work.

Camera Number	**FOV$_x$ [mm]**	**FOV$_y$ [mm]**	**Spatial resolution in x-direction [mm/pixel]**	**Spatial resolution in y-direction [mm/pixel]**
1.	47.6	35.6	0.095	0.041
2.	47.6	35.6	0.086	0.039
3.	47.6	30.8	0.044	0.041
4.	47.6	33.2	0.05	0.04
5.	42.8	35.6	0.042	0.041
6.	47.6	40.4	0.055	0.043

Table 4.2: Field of view and spatial resolutions of the six cameras.

4.4. Experimental cases

Experimental cases involved flames consisting of pure Dutch Natural Gas (DNG), a mixture of Hydrogen with DNG, and pure Hydrogen flames. While the phantom study provided an initial estimate of the reconstruction results using the defined camera angles in the experimental setup, it was deemed essential to commence the experimentation phase by examining the outcomes with Dutch Natural Gas (DNG) flames. Turbulent premixed flames exhibit distinctive wrinkled flame fronts and the intensity of these wrinkles amplifies notably with an increased hydrogen fraction [28],[45]. Hence, it was reasonable to deduce that flames composed purely of hydrogen would indeed exhibit an intricate and highly wrinkled flame front structure. Consequently, the decision to initiate the experimental phase with pure Dutch Natural Gas (DNG) flames, which present a relatively simpler flame structure in terms of flame front intricacies compared to pure hydrogen flames, was made. This approach ensured the acquisition of valuable insights into both the image acquisition and reconstruction processes before progressing to more complex experiments with hydrogen flames. The previous thesis work by Willems [16] played a significant role in establishing the experimental condition for the CTC study. The results obtained from flashback map analysis for both DNG and hydrogen flames provided valuable insights and guidance in setting up the experimental parameters. Table 4.3 summarises the experimental cases conducted in

this study.

Case Number	Fuel	Equivalence Ratio [-]	Fuel composition by volume fraction) [%]	Bulk Velocity (U_b) [m/sec]	Reynolds number ($\frac{U_b D_b}{\nu_{mix}}$) [-]	Flame type
1.	DNG	1	100%	2.13	3500	Stable
2.	DNG	1	100%	1.68	2750	Close to flashback
3.	DNG	1	100%	1.4	2300	Flashback
4.	Hydrogen and DNG	1	50% H_2 50% DNG	5.9	9000	Stable
5.	Hydrogen and DNG	1	60% H_2 40% DNG	6.71	10000	Stable
6.	Hydrogen and DNG	1	80% H_2 20% DNG	12.26	17000	Stable
7.	Hydrogen and DNG	1	80% H_2 20% DNG	11.54	16000	Close to flashback
8.	Hydrogen and DNG	0.5	100% H_2	11.49	16000	Stable

Table 4.3: Cases for the experiment.

4.5. Experimental methodology

The CTC technique comprises a two-step process. The first step involves capturing images (projections) of the flame from various perspectives, while the second step entails reconstructing the acquired images. The following section provides information about the image acquisition process.

4.5.1. Image acquisition process

Once the experimental cases were determined, the image acquisition parameters needed to be finalized. One of the crucial considerations was to prevent motion blur, which occurs when the target object moves rapidly within the exposure time, leading to positional variations between the start and end of the exposure. The longer the exposure time (integration time), the higher the chances of motion blur occurring. DNG flames are generally less dynamic than hydrogen flames meaning that changes in the features of DNG flames happen at a comparatively slower pace than in hydrogen flames. To address this difference in dynamic behavior two distinct exposure times were chosen for DNG and hydrogen flames to minimize or eliminate motion blur as much as possible while maintaining a sufficient flame intensity in the recordings. For DNG flames an exposure time of 60 ms was considered appropriate. On the other hand, for hydrogen flames, given their more rapid and dynamic behavior, an exposure time of 6 ms was considered suitable. Table 4.4 provides a summary of the exposure times and frame rates (recording rates) utilized for imaging the eight experimental cases.

Case Number	Exposure Time [ms]	Frame Rate [Hz]
1.	60	2.5
2.	60	2.5
3.	60	8
4.	6	2.5
5.	6	2.5
6.	6	2.5
7.	6	2.5
8.	6	2.5

Table 4.4: Exposure time and recording rates for the experimental cases.

As evident (from Table 4.4), the frame rates employed are notably low. This choice was necessitated by a technical problem with the DAVIS software, which unfortunately led to software crashes when attempting image acquisition at higher frame rates (as was also mentioned in Section 4.1). Consequently, a frame rate of 2.5 Hz was chosen to ensure system stability during image acquisition. However, for the specific case of flashback with DNG flames, the frame rate was increased up to 8 Hz. Due to the rapid nature of the flashback, the frame rate of 8 Hz proved inadequate for capturing the propagation of flame during the phenomenon.

During the image acquisition process, it was observed that as the hydrogen volume fraction increased, the flame tended to become less visible. It was anticipated that flame images with very low-intensity values (low visibility) might not yield high-quality reconstructions and, consequently, might not provide substantial information about the flame's features. Consequently, the final selection for experimental cases included only the first four cases (Cases 1-4), which involved pure DNG flames at three different Reynolds Numbers, and a 50% Hydrogen blended with 50% DNG flame. These cases were chosen for the reconstruction process and further analysis.

The subsequent section offers an explanation of the second step in CTC, which involves reconstruction. This section provides detailed insights into the input parameters supplied to the imaging software and explains how the reconstructed object is stored by the software.

4.5.2. Reconstruction Methodology

Prior to getting into the methodology, it is essential to understand the 3D reconstruction coordinate system employed in the study. Figure 4.12 illustrates the 3D coordinate system of the reconstruction domain (measurement volume). The X, Y, and Z coordinates describe the width, height, and depth of the flame respectively. Furthermore, the diagram depicts the manner in which a voxel with intensity $E(X, Y, Z)$ contributes a fraction $'w'$ to generate a pixel intensity $I(x, y)$ on the image plane.

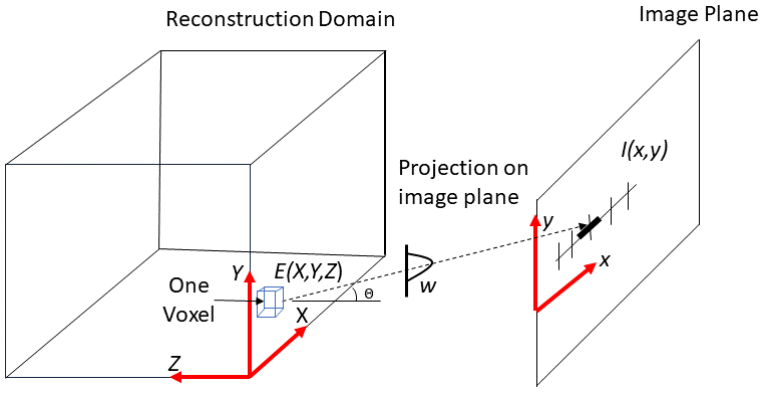

Figure 4.12: 3D Coordinate system used in the study.

Around 1000 instantaneous images were captured for each of the experimental cases mentioned in Section 4.4. However, considering the substantial time required for reconstructing 1000 images for a single experimental case (which could take months), only 150 images were selected from each experimental case for reconstruction. To improve the reconstruction process, image pre-processing was executed, which involved the removal of background intensity from the images. After image pre-processing the tomographic reconstruction was conducted using the DAVIS 8.3.1 tomographic-PIV module. As previously discussed in Section 2.2.3, the tomographic reconstruction process involves discretizing the measurement volume into cubic elements referred to as voxels. The DAVIS imaging software determines the number of voxels based on the user-specified dimensions of the measurement volume. In this study, the intensity distribution of the flame was reconstructed within a volume measuring 48 $\times$ 51.57 $\times$ 48.5 mm^3 discretized into 948 $\times$ 1019 $\times$ 958 voxels. This reconstruction process was carried out using the MART-precise algorithm (with a relaxation parameter of μ = 1) provided by the tomographic-PIV module. The specified measurement volume effectively covered the 3D distribution of the flames. The measurement volume's dimensions were chosen such that the 3D flame distribution near the rim of the quartz tube, where the flame front is thin and has minimal intensity contribution from exhaust gas emissions could be accommodated while being at a sufficient distance from the boundaries of the measurement volume. However, it was observed that the volume proved insufficient to fully encompass the 3D distribution of the upper sections of the flame while maintaining an adequate distance from the measurement volume's boundaries. These upper sections of flame, have a higher concentration of exhaust gases. As a result, the chosen dimensions of the measurement volume, based on the thin flame front structure near the quartz tube exit, were somewhat insufficient in completely encompassing the upper sections of the flame (situated further away from the quartz tube) while keeping a good distance from the volume's boundaries. However, in this study, the emphasis is on the 3D distribution of flame sections closer to the quartz tube exit, as they are expected to reveal features related to the events before flashback initiation. Therefore, the selected dimensions of the measurement volume were considered suitable for the reconstruction process. The reconstruction of 150 images took approximately 78-90 hours for each of the four experimental cases when executed on a PC.

After knowing the details of the inputs given for flame reconstruction in DAVIS it is important to understand how the specified algorithm in the software stores the reconstructed object. The DAVIS imaging software reconstructs the entire 3D domain of the object. However, it does not store an entire 3D volume in a single file. Instead, it stores the data plane by plane in depth or Z direction. The number of planes is equal to the number of voxels in the Z direction. In simple terms, these planes are vertical slices of the flame at different depth locations. If all these vertical slices are stacked up together the entire 3D volume of the flame can be visualized. To further extract the horizontal planes/slices of the flame at a specific height above the rim, the reconstructed intensity distribution of all the vertical planes at that particular height are stacked together.

Figure 4.13 illustrates this method of storing vertical cross-sections of the flame, presenting outcomes from a reconstructed image of a 100% DNG flame at Re = 3500, depicted at selected planes.

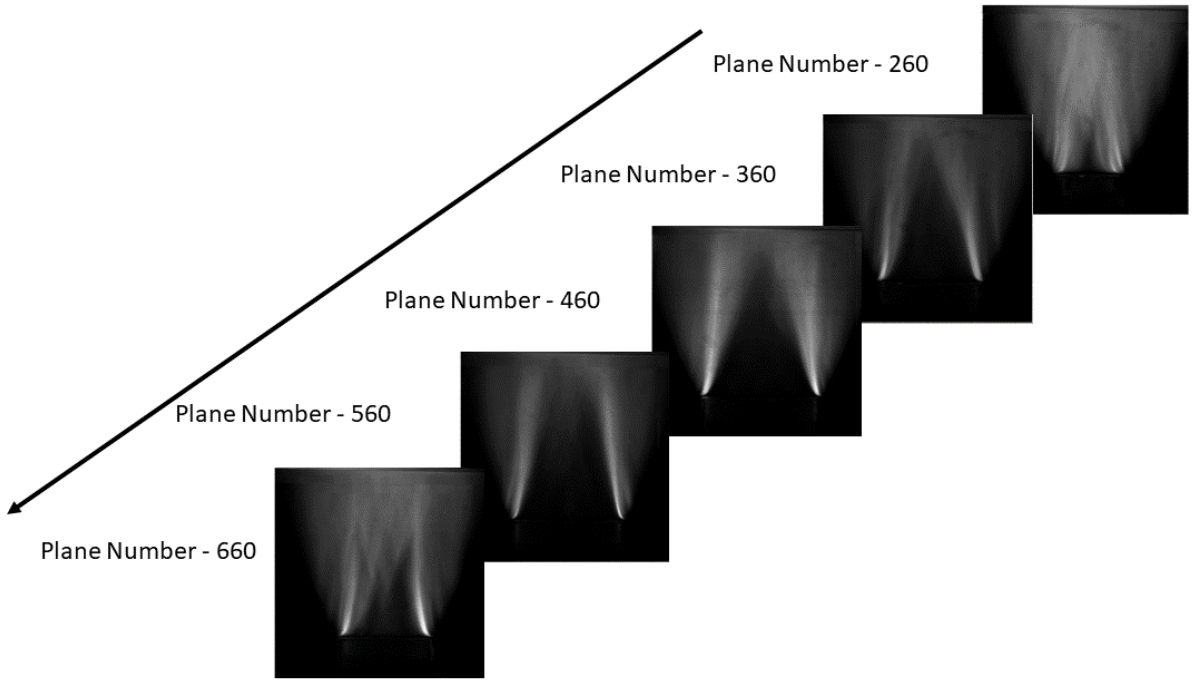

Figure 4.13: Visualization of how the software stores the reconstructed object as vertical slices (Only a few selected vertical slices are displayed). The vertical slices presented here are of 100% DNG flame at Re = 3500.

5

Results and discussion

This chapter explores the outcomes derived from the conducted experiments and is structured into two main sections. Section 5.1 presents the flame images captured by all six cameras, along with a discussion on their intensity distribution. Section 5.2, on the other hand, focuses on the results of tomographic reconstruction. These reconstruction results are subjected to qualitative analysis through visual assessment to identify specific flame features. Furthermore, a statistical analysis is conducted, and the cone angle of the flame is quantified and reported.

5.1. Image Acquisition

This section showcases instantaneous images captured by all six cameras, aiming not only to display images of DNG and hydrogen flames but also to highlight the disparity in signal strength of their captured chemiluminescence emissions. This difference in signal strength has been examined by analyzing intensity profiles of the instantaneous flame image as captured simultaneously by all six cameras.

Figure 5.1 and Figure 5.2 displays instantaneous images of a 100% DNG flame at Re = 3500 and of a 50% Hydrogen blended with 50% DNG flame as captured by all six cameras.The recorded (acquired) images of the other two cases of 100% DNG flame at Re = 2750 and Re = 2300 have been presented in the Appendix section (Section A). The acquired images provide multiple views of the flame, each captured from the unique perspective of an individual camera. In all these images, the flame is recognizable as the conical region depicted by intensity distributions at the upper range of the colormap. Nevertheless, there is also another significant intensity distribution surrounding the flame, which lies within the lower range of the colormap. These distributions correspond to the exhaust gas emissions (such as water vapor emissions). Due to the absence of filters on the cameras used in the experiments to suppress these emissions, these distinct intensity distributions are prominent in the images and are expected to also manifest in the reconstruction results. Additionally, from these images, it can be noticed that the entire height of the flame is not visible. Furthermore, the image obtained from Camera 5 appears to be cropped on the right side somewhere above y = 25 mm. These limitations in image coverage result from the chosen field of view. The field of view was selected based on the present interest in investigating flame sections closer to the quartz tube rim. Considering the anticipation that certain distinctive flame front features related to events preceding the flashback might be discernible in the region closer to the quartz tube rim, this field of view was deliberately chosen to encompass these regions. Additionally, close to the rim, the flame front is thin, and the chemiluminescence emissions from it are minimally influenced by exhaust gas emissions (which become more prominent downstream of the flame). Consequently, it is possible to estimate the strength of chemiluminescence emission intensity from the flame front with reasonable accuracy from this near-quartz tube rim region.

Comparing the flame images of 100% DNG and one blended with 50% Hydrogen a notable intensity difference is apparent. To further understand this difference between pure 100% DNG flame and the one blended with 50% Hydrogen their intensity distributions have been examined.

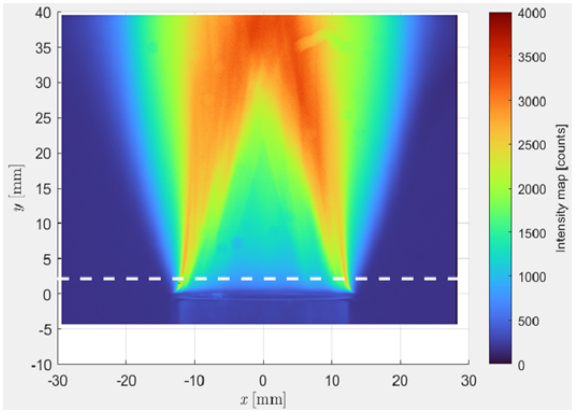

(a) Camera 1

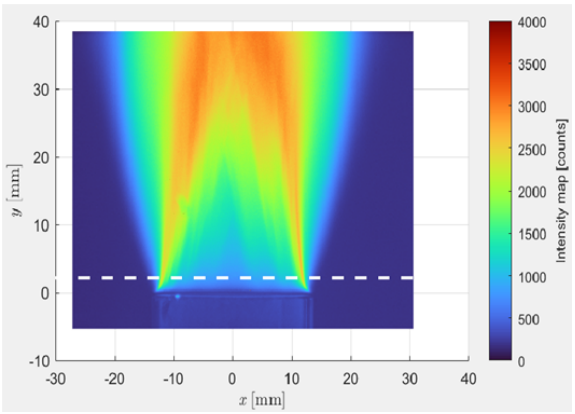

(b) Camera 2

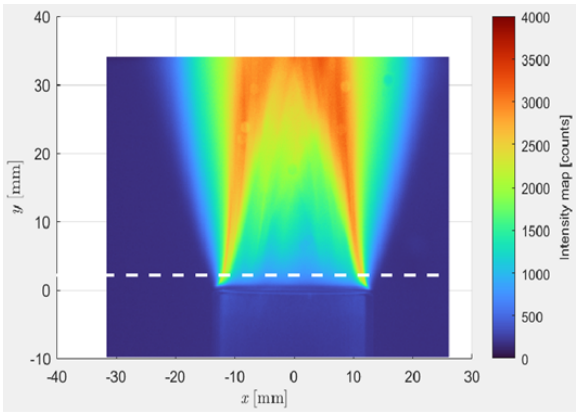

(c) Camera 3

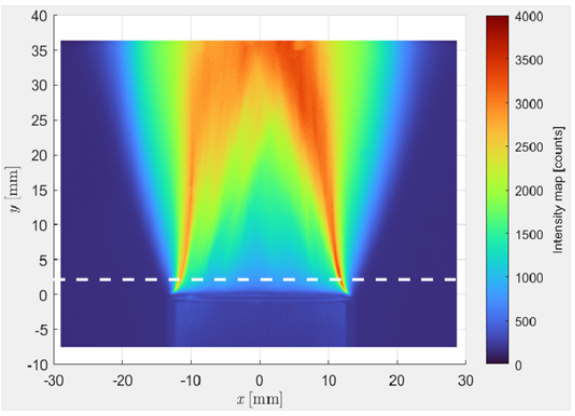

(d) Camera 4

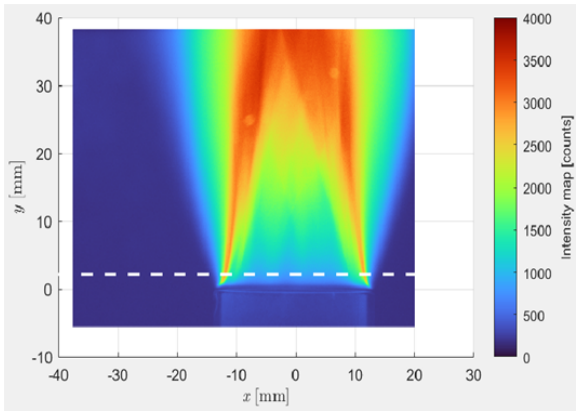

(e) Camera 5

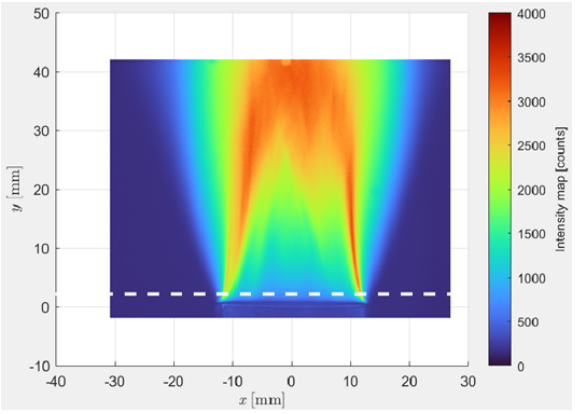

(f) Camera 6

Figure 5.1: Set of simultaneous images acquired for 100% DNG flame at Re = 3500 from all six cameras. The white-dashed line represents the section at which intensity profiles have been extracted.

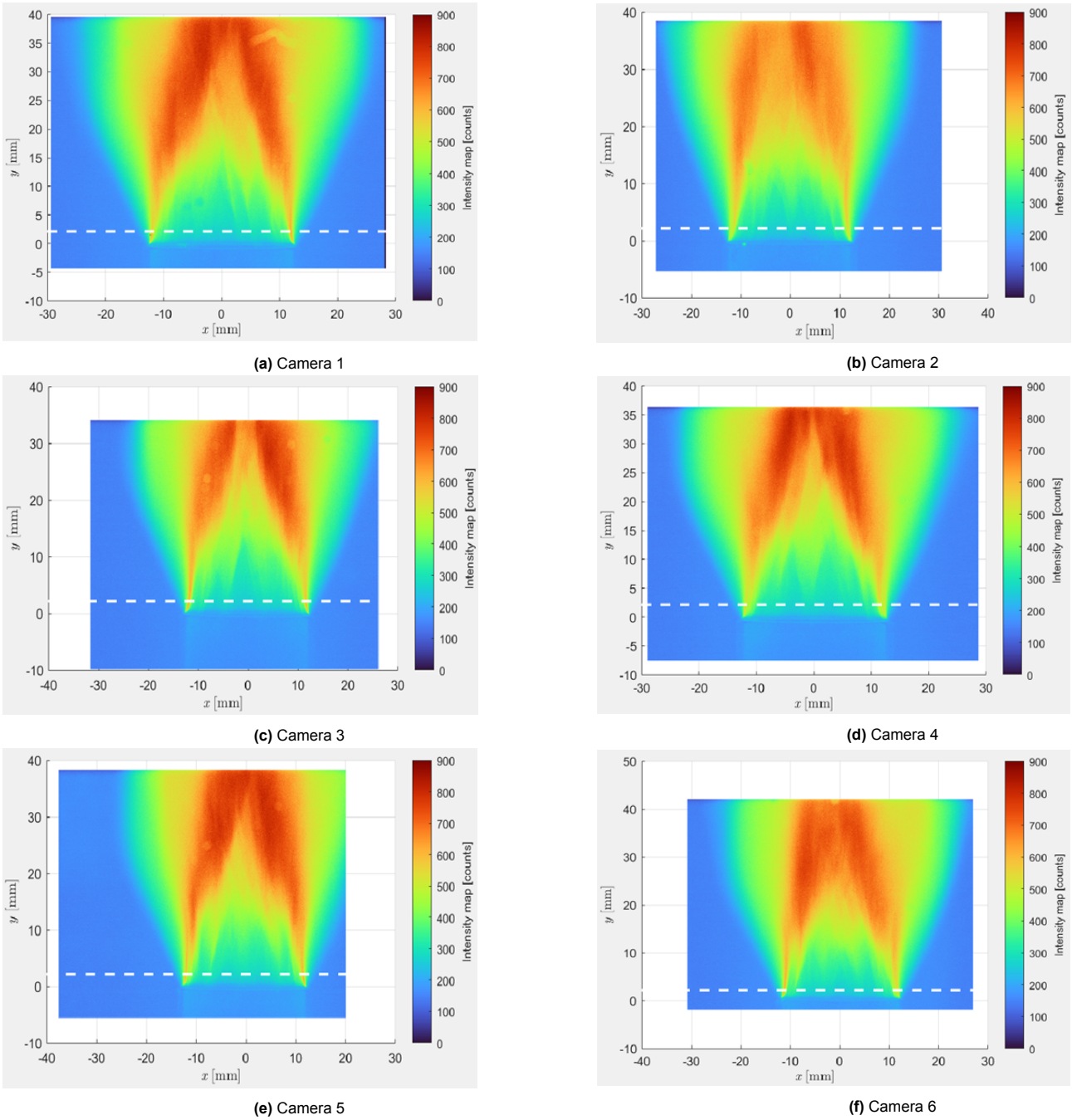

(a) Camera 1

(b) Camera 2

(c) Camera 3

(d) Camera 4

(e) Camera 5

(f) Camera 6

Figure 5.2: Set of simultaneous images acquired for 50% DNG and 50% Hydrogen flame at Re = 9000 from all six cameras. The white-dashed line represents the section at which intensity profiles have been extracted.

The intention behind analyzing the intensity distribution is to justify the difference in the visibility of 100% DNG and 50% Hydrogen flame through signal-to-noise ratios and to examine the intensity of the background region of the flame such that it can removed from the acquired flame images. The intensity in these images is a superposition of background illumination (in addition to offset introduced by the sensor) and the chemiluminescence emissions (also exhaust gas emission intensities when focusing downstream of the flame) from the flame. Since the objective of the study is to reconstruct chemiluminescence emissions (although exhaust gas emissions around the flame front also get reconstructed since cameras are not equipped with suppression filters as will be seen in Section 5.2) of the flame front there is a requirement to remove the background illumination to attain better quality reconstruction. This is based on the assumption that noise fluctuation in the background is uniform over the entire

image such that similar noise levels (as in the background) are present within the flame region as well.

5.1.1. Intensity distributions

To examine the intensity variations of the 100% DNG and 50% Hydrogen flames as observed from different cameras, intensity distributions were extracted near the quartz tube rim (2.17 mm above the rim as indicated by white-dashed solid lines in Figure 5.1 and5.2). In this region, the presence of emissions from the hot exhaust gas is quite low, resulting in a predominant chemiluminescence intensity signal. This section explores the intensity distribution and the chemiluminescence signal strength of the two flames, quantified through the signal-to-noise ratio (SNR). In the scope of this section, the term ”noise” pertains to illumination in the background (Bg) region. Hence, the signal-to-noise ratio (SNR) is determined as the ratio of the Mean of the signal to the Root Mean Square (RMS) of the background region. To define the background region, intensity values towards both the far left and right regions (away from the signal region) were sampled. The average of the sampled noise values was then established as the baseline for calculating other metrics, including the peak of the signal (can be identified in the intensity profiles in Figure5.3), RMS of the background, Mean of the Signal, and consequently the SNR. In all the intensity plots the baseline has been marked with a solid red line while the signal region has been bounded by solid black lines with the background region outside these solid black lines (refer Figure 5.3,5.4).

100% DNG flame at Re = 3500

Figure 5.3 presents the extracted intensity profiles of a segment of 100% DNG flame (at Re =3500) positioned 2.17 mm above the quartz tube rim and recorded simultaneously by all six (Refer to Chapter A, Figure A.3 and A.4 for the intensity profiles of 100% DNG flame at Re = 2750 and 2300 extracted at the same height of 2.17 mm above the quartz tube rim). In the intensity profile of the flame image captured by Camera 1 (Figure 5.3a), a sudden fluctuation is evident in the background region toward the extreme right, indicated by a black-dashed highlight. While this fluctuation does not significantly impact the calculated values of various parameters (the SNR value, including this fluctuation, was found to be 21 and increased to 22.08 after eliminating the fluctuation), it was deemed more appropriate to perform calculations for parameters after removing this fluctuation.

Table 5.1 compiles the essential parameters derived from the intensity profiles, including the mean and RMS values of the background region, as well as the peak and mean of the signal. (For corresponding parameters of the 100% DNG flame at Re = 2750 and Re = 2300, refer to Chapter B, Tables B.1 and B.2.). An initial observation that can be inferred from these intensity profiles is that the RMS of the background region (refer Table 5.1) is notably higher in the scenario where the image was captured by camera 1 followed by camera 2. However, among the remaining cameras, the RMS of the background region exhibits relatively consistent values.

In order to understand the strength of chemiluminescence emissions from 100% DNG flames the SNR values were calculated. It is important to emphasize that the calculated SNR values do not represent exact values (since it is based on sampling of data), but rather an approximation of the possible order of magnitude for the values. These SNR values have been summarized in Table 5.2. Upon careful examination of the values presented in Table 5.2, it becomes evident that the signal-to-noise ratio (SNR) values for all three experimental cases involving DNG flames are nearly similar. Nevertheless, particular SNR values stand out, such as at Re = 2750 for Camera 2 and at Re = 2300 for Camera 4, showcasing slightly heightened values in comparison to the 100% DNG at Re = 3500. This discrepancy could be attributed to the fact that the SNR value comparison is conducted for a specific instantaneous image or snapshot. Consequently, in one scenario, for example in the case of the 100% DNG flame at Re = 3500, the cameras might have captured a relatively stable flame image with minimal dynamics. In contrast, in other scenarios, such as the 100% DNG flame at Re = 2750 and 2300, the cameras might have recorded a more dynamic flame, potentially exhibiting a tilt in a particular direction. This tilt could have led to certain cameras capturing a high signal while others recorded a low signal, resulting in variations in the SNR values derived from the images of the 100% DNG flame at Re = 3500, all of which were taken using the same cameras.

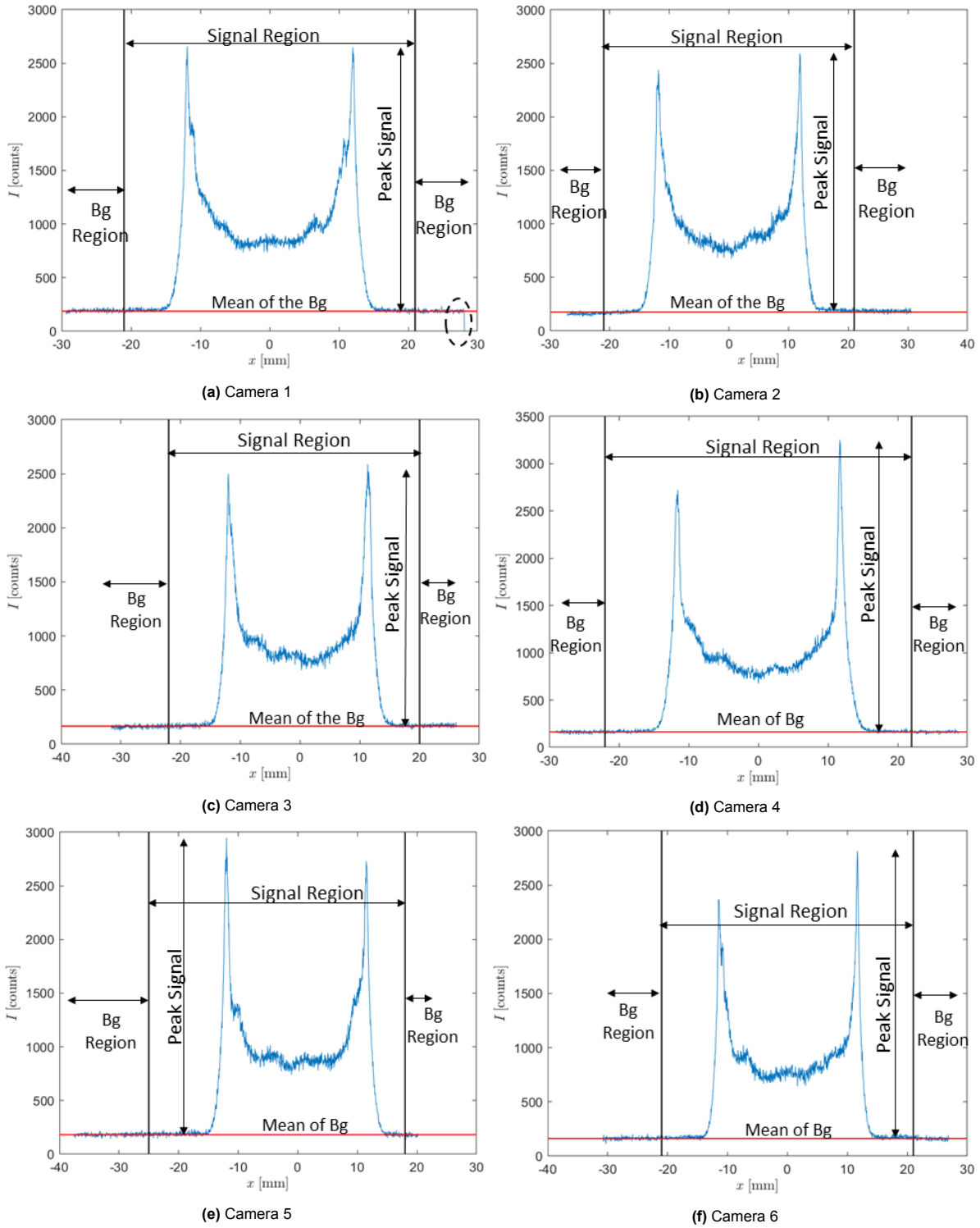

(a) Camera 1

(b) Camera 2

(c) Camera 3

(d) Camera 4

(e) Camera 5

(f) Camera 6

Figure 5.3: Set of intensity profiles of simultaneous images acquired for 100% DNG flame at Re = 3500 from all six cameras. The profiles have been extracted from a segment of flame positioned at a height of 2.17 mm above the quartz tube rim as marked by white dashed lines in Figure 5.1.

Camera Number	Mean of background [counts]	Peak of signal [counts]	Mean of signal [counts]	RMS of background [counts]
1.	187.84	2470.15	596.04	26.98
2.	175.66	2418.33	565.37	17.77
3.	166.5	2422.49	563.32	14.67
4.	162.74	3091.25	575.84	12.01
5.	182.05	2766.94	575.89	13.4
6.	162.32	2650.67	506.19	13.43

Table 5.1: Relevant parameters of intensity profile (Figure 5.3) for simultaneously captured images of 100% DNG flame at Re =3500.

Camera Number	SNR [Re = 3500]	SNR [Re = 2750]	SNR [Re = 2300]
1.	22.08	22.77	21.52
2.	31.81	41.53	35.63
3.	38.38	42.33	43.16
4.	47.94	48.67	55.08
5.	42.97	47.89	48.65
6.	37.66	40.64	44.22

Table 5.2: Signal-to-noise ratio of intensity of 100% DNG flames captured from six cameras.

50% H_2 and 50% DNG flame at Re = 9000

A similar analysis of the intensity distribution has been performed for the case of 50% Hydrogen blended with 50% DNG to establish a comparison in signal strength as captured by the same set of cameras. Figure 5.4 depicts the extracted intensity plots obtained from a segment of the flame positioned 2.17 mm above the rim of the quartz tube (as marked by white dashed lines in the real image in Figure 5.2). At first glance, it is evident that the cameras captured a lower level of chemiluminescence emission from the 50% hydrogen flame. To gain a better understanding of this reduction in signal, various parameters (similar to those in Table 5.1) were computed for the intensity profile. These values are summarized in Table 5.3. Similar to the previous case of the 100% DNG flame at Re = 3500, where there was a pronounced fluctuation on the far right side of the intensity profile in the flame image from Camera 1 (as seen in Figure 5.3a), in this case as well, this strong fluctuation can be observed as indicated with black dashed highlights in Figure 5.4a. Therefore, here as well the calculations were performed after eliminating this fluctuation.

Analyzing the intensity distribution parameters for the scenario involving 50% hydrogen blended with 50% DNG flame, it is evident that the background level remains largely within a comparable range to that of 100% DNG. Nevertheless, a distinct reduction in signal strength becomes apparent when observing the peak signal and SNR values. This reduction in peak signal exhibited a decrease by approximately a factor of five when compared to peak signal values of 100% DNG flame at Re = 3500 in Table 5.1. However, it is essential to note that this comparison does not directly evaluate the chemiluminescence intensity strength between DNG and hydrogen flames.

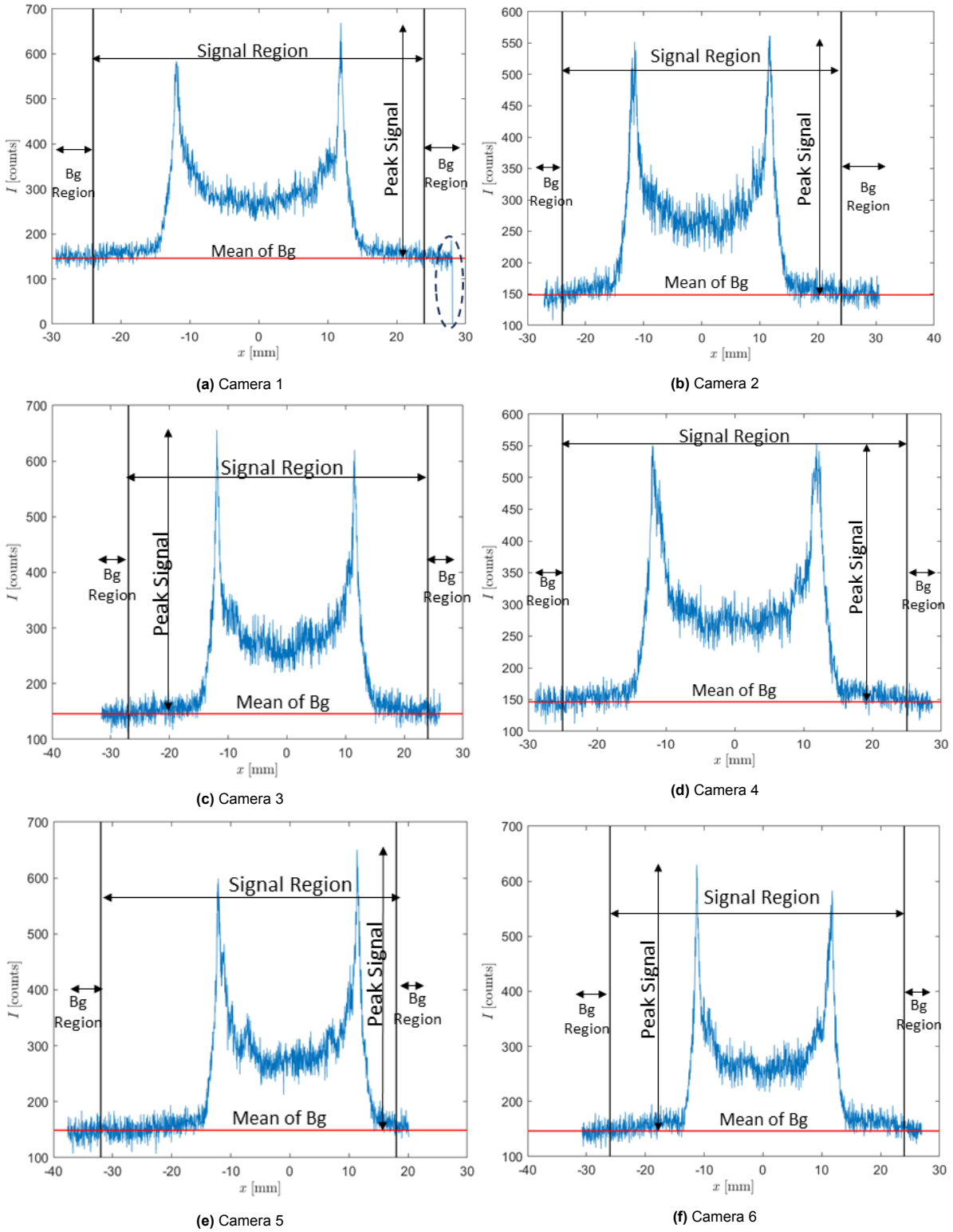

(a) Camera 1

(b) Camera 2

(c) Camera 3

(d) Camera 4

(e) Camera 5

(f) Camera 6

Figure 5.4: Set of intensity profiles of simultaneous images acquired for 50% Hydrogen and 50% DNG flame at Re = 9000 from all six cameras. The profiles have been extracted from a segment of flame positioned at a height of 2.17 mm above the quartz tube rim as marked by white dashed lines in Figure 5.2.

Camera Number	Mean of background [counts]	Peak of signal [counts]	Mean of signal [counts]	RMS of background [counts]	SNR [-]
1.	146.57	523.03	105.41	26.58	3.94
2.	148.57	413.42	95.37	11.85	8.04
3.	145.81	510.18	92.66	13.60	6.81
4.	146.4	406.59	98.83	12.25	8.06
5.	148.89	502.01	96.45	14.61	6.60
6.	146.44	483.55	87.68	12.31	7.12

Table 5.3: Relevant parameters of intensity profile (Figure 5.4) for simultaneously captured images of 50% Hydrogen and 50% DNG flame at Re = 9000.

This is because the chemiluminescence spectrum of a hydrogen flame differs significantly from that of natural gas combustion. In hydrogen-air flames, the most prominent emission features arise from OH^* radicals in the ultraviolet (UV) wavelength range and from excited H_2O molecules in the infrared region. Consequently, an increase in hydrogen content leads to a decrease in chemiluminescence emission within the 'visible region' of the electromagnetic spectrum, while the emission shifts towards the 'ultraviolet (UV) region' of the spectrum [34, 36]. Since the cameras employed are not equipped with UV-transparent lenses, therefore, the captured chemiluminescence emissions seem to diminish for 50% hydrogen and 50% DNG flame as compared to 100% DNG flame. Owing to this visibility limitation, cases involving higher hydrogen percentages and pure hydrogen flames were excluded from the subsequent reconstruction process. The anticipation was that the results would appear excessively noisy and provide minimal details about the flame structure. Hence, image reconstructions were exclusively conducted for the four cases, where the first three involved 100% DNG flames and the fourth one featured a 50% Hydrogen and 50% DNG flame. In the subsequent section, all the reconstruction outcomes are discussed.

5.2. Image Reconstruction

In this section, the results of the reconstruction process for the four chosen experimental cases are presented in detail. In Section 4.5.2, the storage of reconstructed images as planes (vertical slices) was explained, with the number of planes corresponding to the number of voxels in the Z direction. In the present study, the measurement volume has been discretized into 958 voxels along the Z direction. Consequently, the reconstructed image was saved as 958 planes (vertical slices). Due to the impracticality of displaying all these planes (vertical slices), only the center plane (Plane number 479), representing the flame's symmetry axis, has been presented and discussed. Furthermore, 150 images (recorded sequentially), have been reconstructed for each of the four selected experimental cases. This implies that for each experimental case, there are 150 center planes (central vertical slices). Therefore, when discussing instantaneous reconstructed images, only a limited number of central vertical slices are presented for each experimental case.

In addition to examining the central vertical slices of the reconstructed images, horizontal slices of the reconstructed flame are also presented and discussed. The horizontal slices of the reconstructed flame were extracted at four heights above the quartz tube rim for each of the selected experimental cases. Figure 5.5 indicates the heights above the quartz tube rim (positioned at y = 0 mm) at which the horizontal slices were extracted. These heights are marked with blue solid lines on an averaged central vertical slice of a reconstructed 100% DNG flame at Re = 3500 (Note that the horizontal slices for all the selected experimental cases have been extracted at these same four heights; therefore, in the following sections of the document, this figure will be referenced when discussing the heights at which the horizontal slices have been extracted for all the experimental cases).

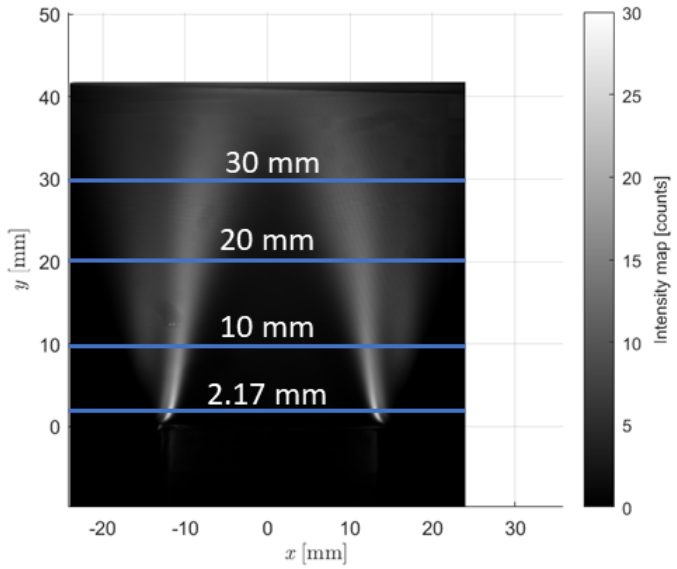

Figure 5.5: Heights above the quartz tube rim at which horizontal slices have been extracted as marked with blue solid lines on an averaged central vertical slice of a reconstructed 100% DNG flame at Re = 3500.

Furthermore, as mentioned earlier, for each selected experimental case, 150 images recorded in sequence have been reconstructed. Therefore, it can be understood that 150 horizontal slices at each of the mentioned heights above the quartz tube rim (refer to Figure 5.5) were extracted. Consequently, only a limited number of horizontal slices at each height have been presented in the discussions related to instantaneous reconstructed images.

5.2.1. Qualitative Analysis

The qualitative analysis has been conducted by visually assessing the central vertical slice and horizontal slices extracted at various heights above the quartz tube from the reconstructed flame images. The analysis has been performed over instantaneous reconstructed images (reconstructions of flame images captured at different instances in time) as well as averaged reconstructed images (the image formed from the average intensity distribution values of multiple instantaneous reconstructed images).

Case 1: 100% DNG flame at Re= 3500

In Figure 5.6, ten sequential images of the instantaneous central vertical slice of the reconstructed flame images are shown. Images presented are at a time interval of 0.4 sec which is according to the recording rate of the imaging device. It is also important to highlight that in all the center vertical images (both instantaneous and average) of pure DNG flames, the intensity counts have been kept in a range of 0-30 counts as also indicated by the upper and lower limits of the intensity map (see Figure 5.5 as an example).

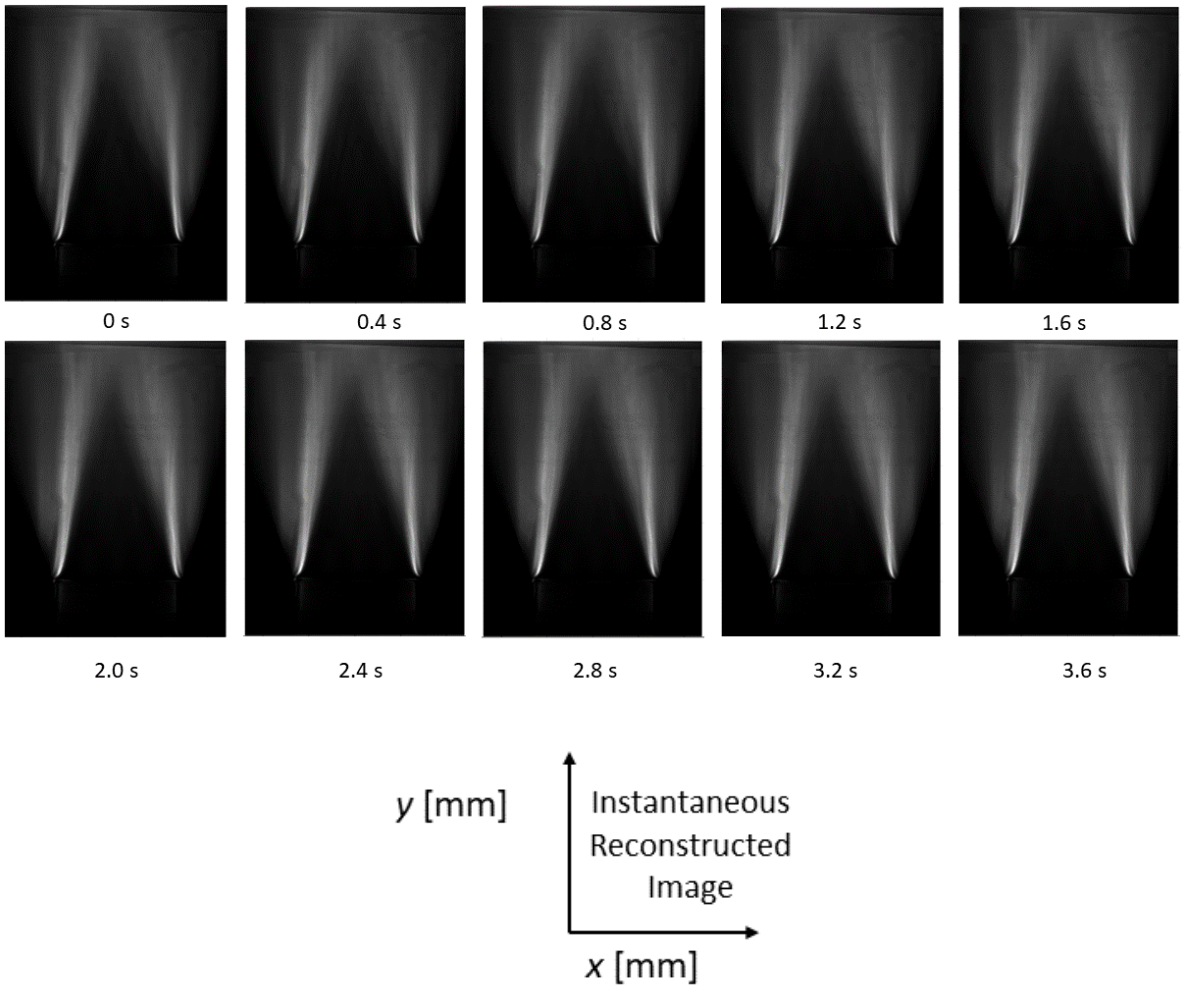

Figure 5.6: Visualization of instantaneous central vertical slices. These ten slices have been extracted from reconstructions of ten sequentially recorded images of a 100% DNG flame at Re = 3500. The time interval between each image is 0.4s as per the recording rate of the imaging device.

From these central vertical slices, the most apparent observation is the conical shape of the flame. Furthermore, since these are instantaneous slices, they also help to visualize the differences in the features of the flame at various instances in time. However, to gain an understanding of the overall shape of the flame and to verify if any consistent feature persists throughout the reconstructed flame images, all 150 central vertical slice images were averaged. Figure 5.7 illustrates the averaged central vertical slice of the flame. Compared to the instantaneous reconstructions (instantaneous central vertical slices), the averaged reconstruction (average central vertical slice) exhibits a notably smoother appearance where finer details (such as enhanced wrinkles) may not be readily apparent. Nonetheless, the averaged reconstructed image affirms the fundamental cone shape of the flame. The flame front region within the image can be identified by tracing the highest intensity values (corresponding to the highest chemiluminescence intensity values) at various heights (y) of the flame. Furthermore, this averaged reconstructed image validates the presence of exhaust gases, as evidenced by regions displaying lower-intensity values surrounding the flame front. Thus, it can be concluded that the presence of exhaust gases is consistent throughout the recorded images, rather than being a characteristic limited to a few of the flame images.

Visual inspection of vertical slices can provide a limited set of information. Further, vertical slices alone might not offer a complete illustration of the algorithm's performance. This is especially true when attempting to assess the quality of reconstruction. As Mohri et al. [20] have noted in their work, even

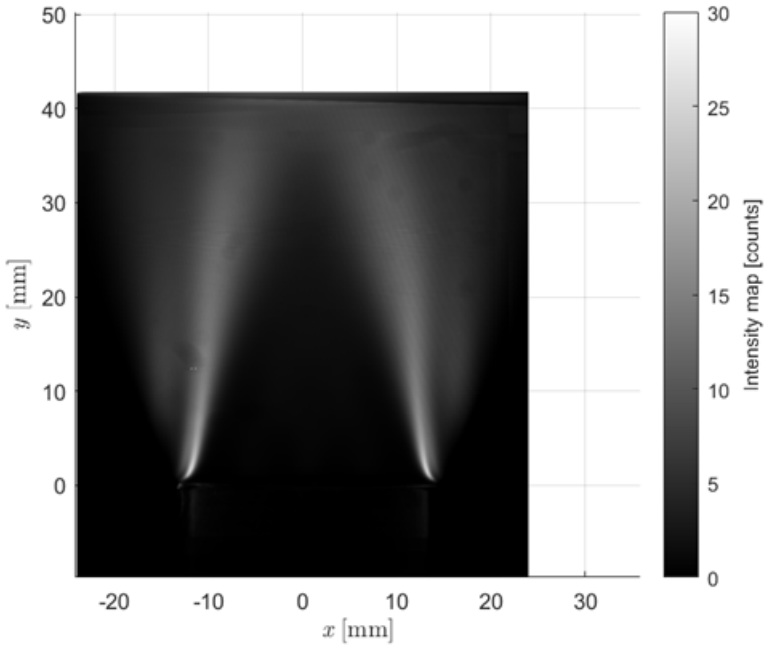

Figure 5.7: Visualization of averaged central vertical slice. The averaged central vertical slice is obtained by averaging the 150 instantaneous central vertical slices of a reconstructed 100% DNG flame at Re = 3500.

if the number of cameras in the CTC setup is reduced, the decrease in reconstruction quality may not be as apparent when examining the vertical slices. However, the reduction in reconstruction quality resulting from the decreased number of views becomes distinctly noticeable in the horizontal slices extracted from the reconstructed volume. Thus, extracting the horizontal slices from the reconstructed flame image in the present work was also essential. Horizontal flame slices have been acquired at different heights above the burner to depict the changing flame structure downstream. The specific heights are indicated in Figure 5.5. It is worth emphasizing that for all cases involving DNG flames, the intensity values in the images were kept within the range of 0-30 counts for a height of 2.17 mm, 0-20 counts for a height of 10 mm, and 0-15 counts for heights of 20 mm and 30 mm. Opting for a similar intensity range would not have been ideal. With increasing distance from the quartz tube rim, the chemiluminescence emission intensity from the flame front weakens while being surrounded by an increased concentration of exhaust gas emissions. The purpose of maintaining different ranges was to ensure that no significant flame features (for example flame front wrinkles, and exhaust emissions such as water vapor emissions) were suppressed. Figure 5.8 illustrates the instantaneous horizontal slices extracted at the mentioned heights (see Figure 5.5) from the reconstruction of seven sequentially captured flame images.

The horizontal slices extracted from the reconstructed intensity field offer a clearer comprehension of the change in the structure of the flame at different time instances and different heights above the quartz tube rim. The flame front in these images can be identified as regions with high-intensity values (bright white color) while the exhaust gas emissions (such as water vapor emissions) can be identified as regions with slightly low-intensity values (faint white color) surrounding the flame front. These reconstruction outcomes (especially those near the rim) largely align with the phantom simulations discussed in Section 4.3.1 (see Figure 4.7). The shape of the flame near the rim (y/D_b = 0.086) is approximately time-independent which allows an assessment of the reliability of the obtained reconstructions. In this near-rim region, the horizontal structure of the flame should be similar to the shape of the quartz tube rim. Given that the rim has a circular configuration, it is expected that the reconstructed flame front would also manifest this circular shape. Indeed the left (towards lower x coordinate values) and right (towards higher x coordinate values) sections of horizontal slices of the flame front appear to follow the circular configuration of the quartz tube rim. However, it is clearly visible that the top (towards higher z coordinate value) and bottom (towards lower z coordinate value) sections do not appear to follow the configuration of the quartz tube rim. As was also identified and hence explained in Section 4.3.1 this

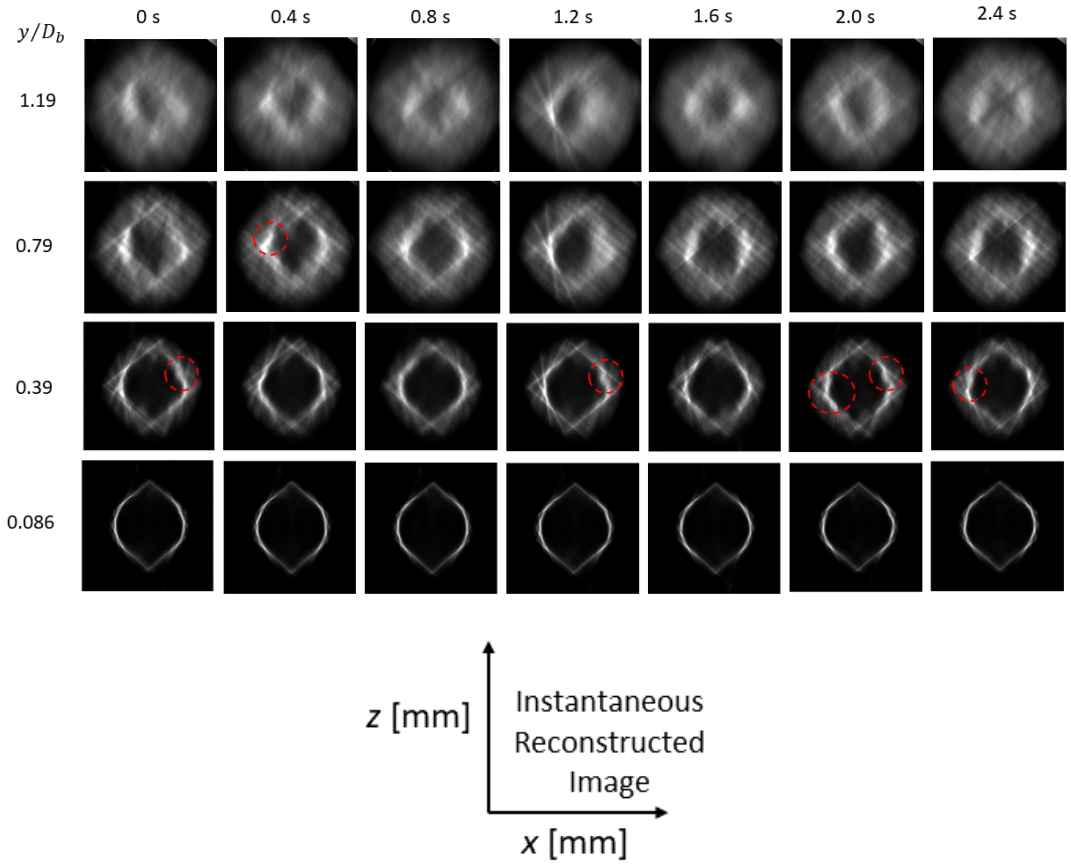

Figure 5.8: Visualization of instantaneous horizontal slices. The horizontal flame slices have been extracted at different heights above the quartz tube rim, where the heights are non-dimensionalized by the inner diameter (D_b) of the quartz tube. These seven slices at each height have been extracted from reconstructions of seven sequentially recorded images of a 100% DNG flame at Re = 3500. In a few of these images, the red dashed highlights (visual aids and not computed quantities) indicate the wrinkles of the flame.

inaccurate reconstruction of the top and bottom sections of the flame front is due to the absence of cameras with a line-of-sight directly towards the front and back of the quartz tube as can be seen in the schematic of CTC setup (Figure 4.5). Therefore, in situations where there is extremely limited or no information available about a particular section of the object during the image acquisition process, it is possible that the reconstruction algorithm may face challenges in converging to an exact solution. Nonetheless, based on the available intensity data, the algorithm can still produce a 3D distribution of the section through interpolation. Hence, based on the interpolation results of the algorithm the top and bottom sections of the horizontal flame front regions do not appear to exactly follow the circular shape of the quartz tube rim.

As the observation point shifts downstream (towards $y/D_b = 1.19$) away from the quartz tube rim, it becomes apparent that the concentration of exhaust gases becomes more prominent. Despite the visibility of the flame front characterized by the heightened chemiluminescence intensity distribution, it is notable that this region appears crowded due to the presence of exhaust gas emissions. Furthermore, the visibility of line artifacts (which can be noticed as straight bright line streaks) reflects the challenges the MART algorithm encountered due to the limited number of views. Nonetheless, the obtained results still manage to capture intricate details, such as wrinkles of the flame. In Figure 5.8, these wrinkles in some of the images have been indicated using red dashed highlights (Note: These red dashed highlights are visual aids and are not computed quantities). Wrinkles become more evident in the reconstruction results of the second experimental case, which features a 100% DNG flame at Re = 2750 (Figure 5.12). This second case (5.2.1) will be discussed later in detail.

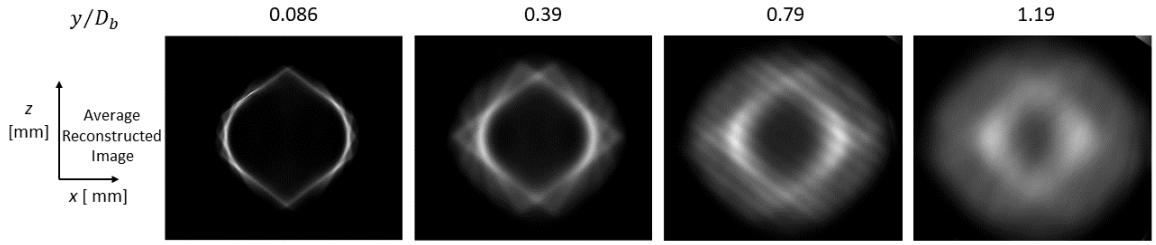

Figure 5.9: Visualization of the averaged horizontal slice at different dimensionless heights above the quartz tube rim. The averaged horizontal slice is obtained by averaging the 150 instantaneous horizontal slices of 100% DNG flame at Re = 3500 at each corresponding dimensionless height above the quartz tube rim.

At each of the four heights, an average image from the 150 instantaneous reconstructed images is computed to get a better understanding of the overall shape of the flame. Figure 5.9 presents the average shape of horizontal slices of the flame at different non-dimensionalized heights above the quartz tube rim. These averaged reconstructed images confirm the circular shape of the horizontal slice of the flame in the region where reconstruction is reliable (left and right sections of the horizontal slice). These averaged reconstructed images further confirm a noticeable transition as the vertical distance from the quartz tube rim increases which was also apparent in the instantaneous reconstructed images. The inner area surrounded by the flame front appears to decrease (Figure 5.9), implying a cone-like three-dimensional volumetric structure of the flame. This observation aligns with the insights derived from the analysis of the vertical slices of the flame which revealed the conical shape of the flame.

This particular illustration of a stable DNG flame has been presented with the specific purpose of demonstrating that the devised experimental setup and employed tomographic methodology can reconstruct a flame providing its volumetric structure. An important objective of analyzing this case was to highlight fundamental visual observations that can be drawn from the reconstructed flame images.

Case 2: 100% DNG flame at Re = 2750

Knowing that the reconstruction technique indeed provides good three-dimensional insight, the technique was applied to a more complex case involving 100% DNG flame close to a flashback condition. This investigation aimed to understand the alterations in the structure of the flame as it approaches the close-to-flashback conditions. Similar to the previous stable DNG flame case, this section presents central vertical and horizontal slices of both instantaneous and averaged reconstructed flame. Figure 5.10 presents ten sequential images of the central vertical slice of the reconstructed 100% DNG flame at Re = 2750. At first sight, the reconstructed vertical slices of the flame at Re =2750 seem to closely resemble those of the previous case (100% DNG at Re = 3500). However, upon closer inspection, distinctive streak-like features become apparent in this close-to-flashback condition, as indicated by the red dashed highlights in Figure 5.10 (Note: These red dashed highlights visual aids and not computed quantities). These streak-like characteristics may indicate prominent flame wrinkles. However, this assessment is based on a visual examination of the instantaneous central vertical slice of the reconstructed flame and although these streaks may not be readily observable in an averaged image, further validation of this notion regarding increased wrinkles may be obtained by examining the instantaneous horizontal slices of the reconstructed flame.

Nevertheless, to confirm the overall shape of the flame the 150 instantaneous images of central vertical slices of the reconstructed flame are averaged. Figure 5.11 illustrates the average central vertical slice of the reconstructed 100% DNG flame at Re = 2750.

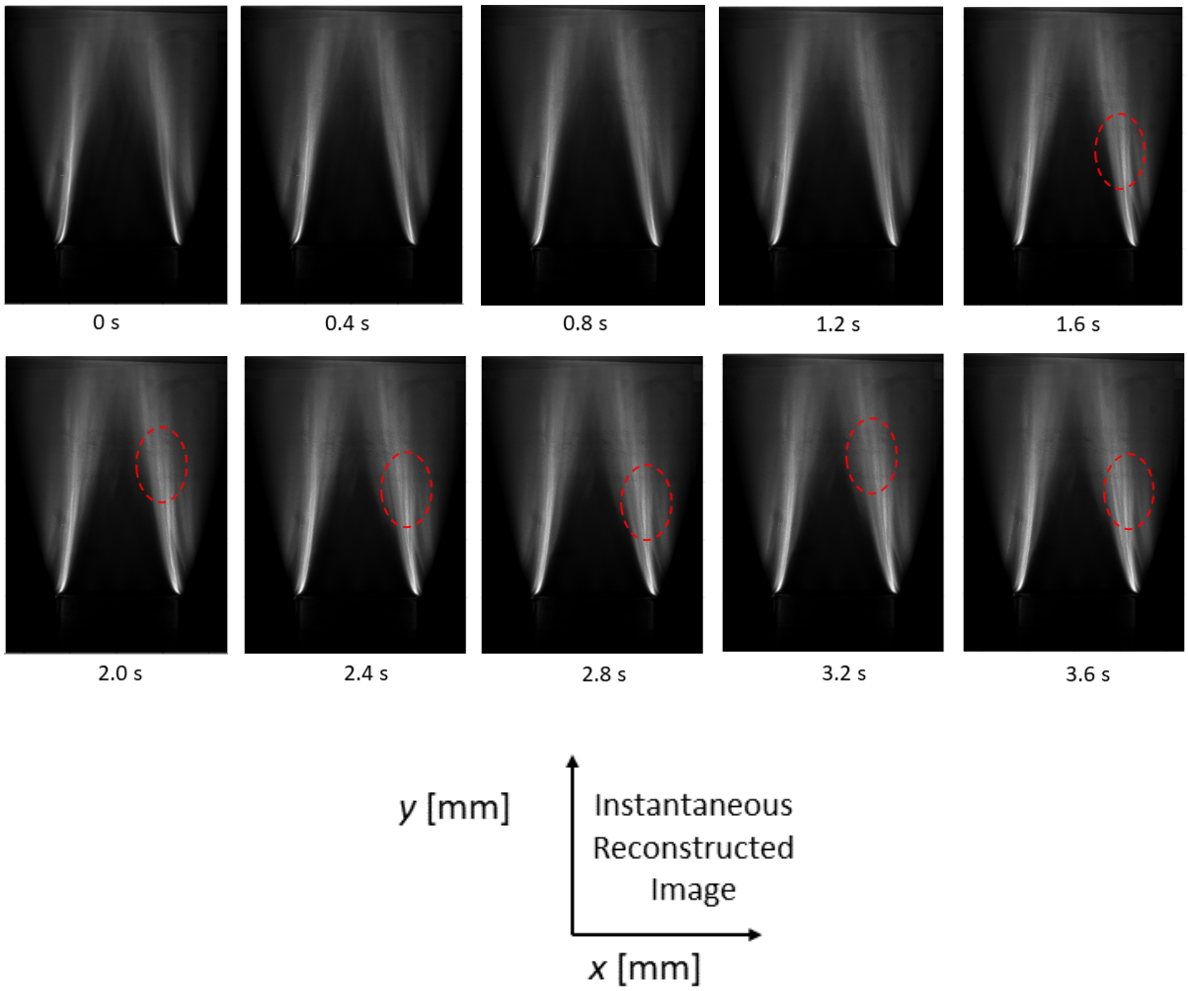

Figure 5.10: Visualization of instantaneous central vertical slices. These ten slices have been extracted from reconstructions of ten sequentially recorded images of a 100% DNG flame at Re = 2750. The time interval between each image is 0.4s as per the recording rate of the imaging device. The red dashed highlights (visual aids and not computed quantities) marked in a few of the images indicate the streak-line characteristics.

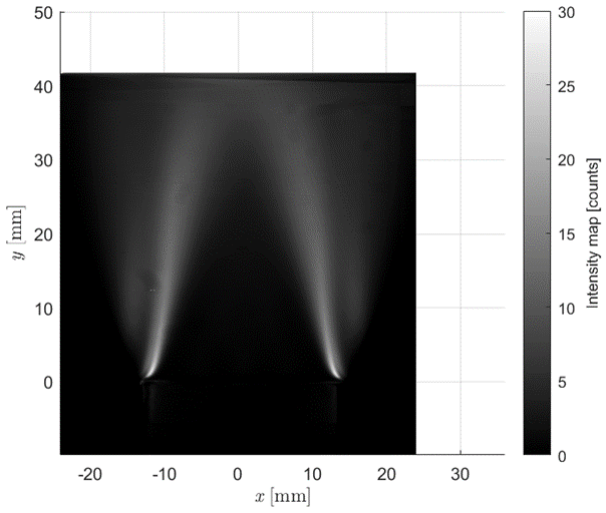

Figure 5.11: Visualization of averaged central vertical slice. The averaged central vertical slice is obtained by averaging the 150 instantaneous central vertical slices of a reconstructed 100% DNG flame at Re = 2750.

As evident in Figure 5.11, the conical shape of the flame persists, along with the presence of exhaust gases around the flame front especially towards the downstream of the flame. Furthermore as expected the streak-like features have vanished in this averaged depiction. Therefore, to get more details about the flame shape when subjected to a situation close to a flashback, the horizontal slices were also studied.

Figure 5.12 presents the horizontal slices extracted at the same heights (see Figure 5.5) as in the previous case. From the extracted horizontal slices the immediate observation that can be made (particularly for the cases away from the quartz tube rim), is that the wrinkles in the flame appear more prominent when compared to the wrinkles in the previous case (Figure 5.8). Furthermore, the wrinkles appear to be displacing or moving inwards, as pointed out by the red dashed highlights (Note: These red dashed highlights are visual aids and not computed quantities). Upon a closer and more detailed examination, it becomes apparent that the flame structures at y/D_b = 1.19 resemble the area near the tip of the cone. This is notable because, in this scenario, the inner area surrounded by the flame front (region indicated by high-intensity values or regions with bright white colors) seems to be smaller than the inner area surrounded by the flame front of 100% DNG flame at Re = 3500 (see Figure 5.8) for the same height above the quartz tube rim. This observation implies the possibility of a reduced flame height in comparison to the previous case. In order to confirm characteristics such as being in closer proximity to the tip of the cone, all 150 instantaneous images of horizontal slices extracted from the reconstructed image of 100% DNG flame at Re = 2750 were averaged. The results are depicted in Figure 5.13.

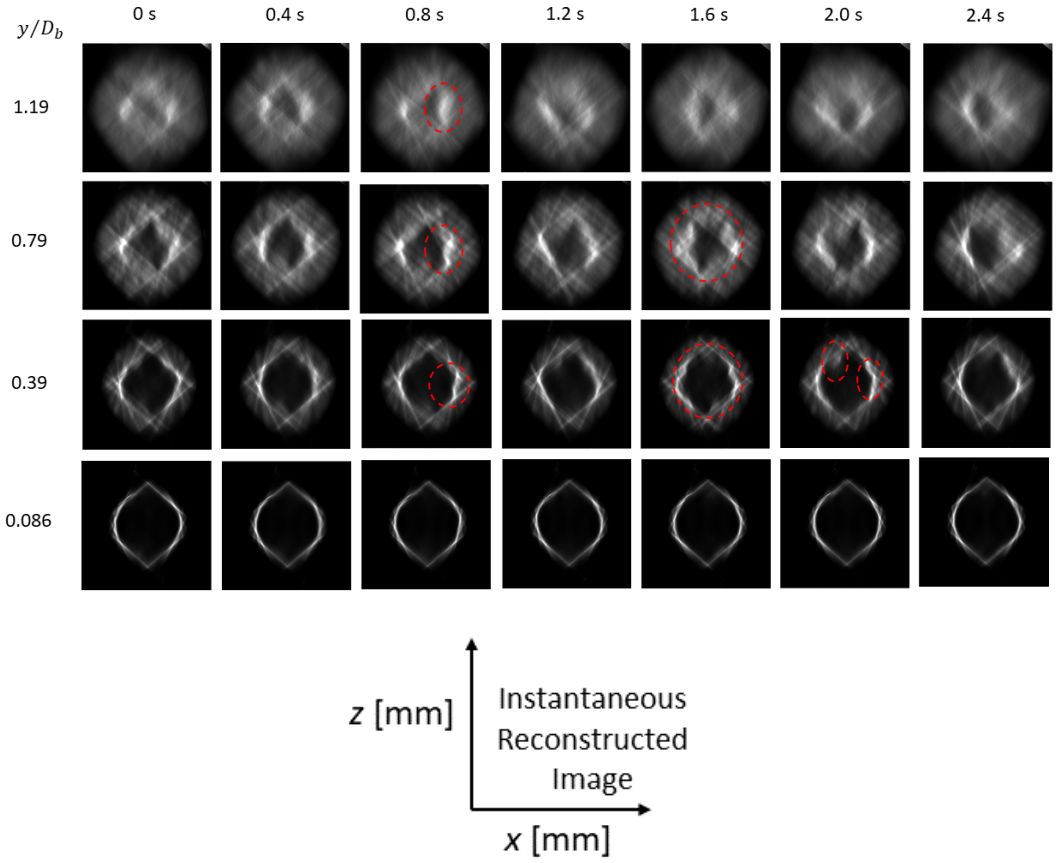

Figure 5.12: Visualization of instantaneous horizontal slices. The horizontal flame slices have been extracted at different heights above the quartz tube rim, where the heights are non-dimensionalized by the inner diameter (D_b) of the quartz tube. These seven slices at each height have been extracted from reconstructions of seven sequentially recorded images of a 100% DNG flame at Re = 2750. In a few of these images, the red dashed highlights (visual aids and not computed quantities) indicate the wrinkles of the flame displacing inwards.

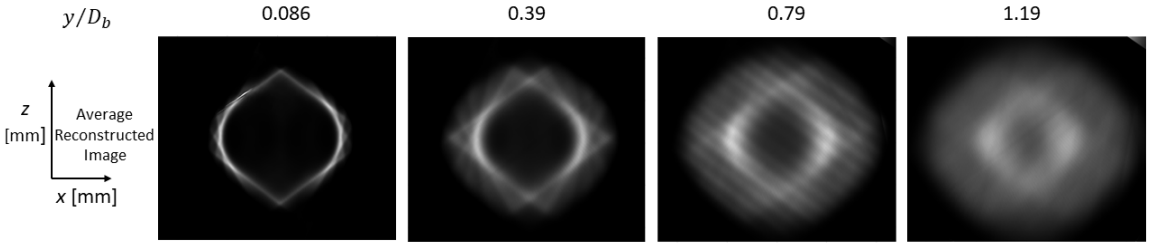

Figure 5.13: Visualization of the averaged horizontal slice at different dimensionless heights above the quartz tube rim. The averaged horizontal slice is obtained by averaging the 150 instantaneous horizontal slices of 100% DNG flame at Re = 2750 at each corresponding dimensionless height above the quartz tube rim.

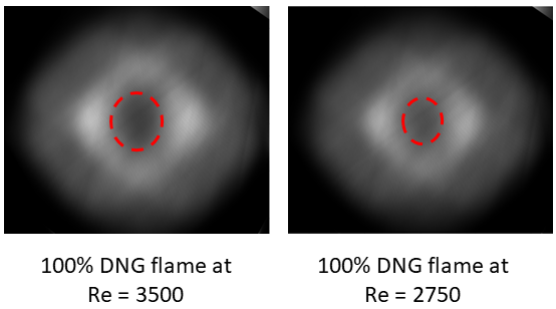

Figure 5.14: Comparison between averaged horizontal flame slices at y/D_b = 1.19 of 100 % DNG flame at Re = 3500 and Re = 2750. The red dashed highlights (visual aids and not computed quantities) roughly indicate the inner area surrounded by the flame front region.

Averaging the horizontal slices tends to obscure the flame's wrinkles. However, it does reveal that at y/D_b = 1.19, the structure of the 100% DNG flame at Re = 2750 resembles the region near the cone tip, as can be observed in the instantaneous reconstructed images as well. This conclusion can be explained better with a comparison between averaged horizontal slices of the reconstructed image of 100% DNG flame at Re = 3500 and Re = 2750. Figure 5.14 illustrates this comparison. The inner region surrounded by the flame front region has been roughly marked by red dashed highlights (Note: These red dashed highlights are visual aids and not computed quantities), and it seems to be smaller for 100% DNG flame at Re = 2750 than 100% DNG flame at Re = 3500. This implies that in the present case, the region is closer to the section near the tip of the cone and gives an indication that the cone tip has shifted downwards towards the quartz tube rim.

These findings affirm the proficiency of the 3D reconstruction technique in capturing intricate flame characteristics, even in the presence of conditions close to flashback. Consequently, the study was expanded to explore a more intricate scenario: inducing flashbacks.

Case 3: 100% DNG flame at Re= 2300

In this case, the initiation of flashback for the 100% DNG flame was achieved by decreasing the Reynolds Number of the flow to 2300. The objective here is to identify features that are distinctive to the events before the onset of the flashback (The characteristics of flame propagation during flashback within the quartz tube can not be identified due to the restrictions imposed by the frame rate, which hindered the capturing of the progression of flame during the flashback event.). The forthcoming analysis will concentrate on only the reconstruction outcomes derived from the final few images acquired immediately prior to the flashback event, with the expectation that these results might unveil certain distinctive features. As was done in the previous cases, here as well the instantaneous and averaged central vertical slice of the reconstructed flame images have been extracted. Based on the acquired images, no flame was observed after 18.625 seconds from the start of the recording, indicating the occurrence of a flashback where the flame had propagated upstream into the burner. Therefore, the instantaneous central vertical slices presented in Figure 5.15 here are from the reconstructions of ten flame (100% DNG at Re = 2300) images recorded sequentially just before the flashback. The images are at an interval of 0.125s based on the recording rate of the cameras.

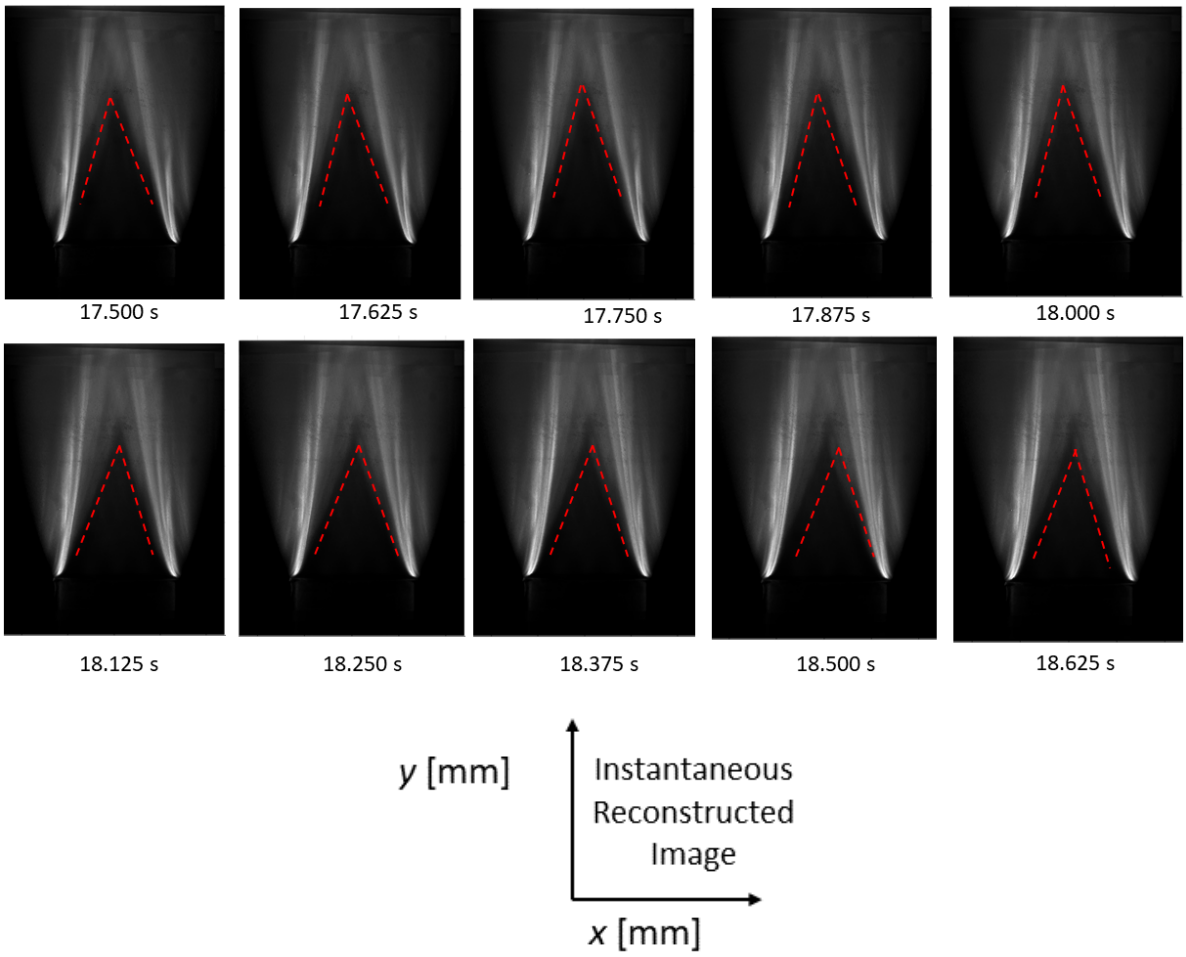

Figure 5.15: Visualization of instantaneous central vertical slices. These ten slices have been extracted from reconstructions of ten sequentially recorded images of a 100% DNG flame at Re = 2300 before flashback. The time interval between each image is 0.125s as per the recording rate of the imaging device. The red dashed highlights (visual aids and not computed quantities) marked in a few of the images attempt to point out the subtle tilting of the flame towards the right side moments before the flashback.

Visual examination of these vertical slice images reveals that in the moments just before flashback (bottom row in Figure 5.15), the flame exhibits a subtle tilt to the right, as compared to the vertical slice images of the flame still seconds away from experiencing flashback (top row in Figure 5.18). This distinction is further emphasized by the red dashed highlights (Note: These red dashed highlights are visual aids and not computed quantities). Additionally, the line streaks that were observed in the previously discussed case of 100% DNG flame at Re = 2750, are also present in this case involving flashback, but they appear even more pronounced. This might be an indication that the wrinkles around the 100% DNG flame at Re = 2300 have become even more prominent as compared to the previous two cases. Figure 5.16 presents the averaged central vertical slice from the reconstructed flame image. As expected, the tilted flame is not distinctly visible in this image. Nevertheless, the overall conical shape of the flame remains consistent with observations from earlier cases along with the increased concentration of exhaust gases around the flame front downstream of the flame. To confirm whether the flame tilts to one side before the event of the flashback, an average of only the last ten instantaneous central vertical slice images of the reconstructed flame was generated (Figure 5.15). Figure 5.17 displays the result obtained when averaging only the last ten images of the instantaneous central vertical slice of the reconstructed flame. The tilting of the flame may suggest that the flashback might have initiated from the left section of the flame. Careful observation reveals that the left slant height of the cone appears to be displaced to the right, particularly in the upper section (see the zoomed-in image in Figure 5.17), while the right slant height remains relatively consistent in position when compared to either the

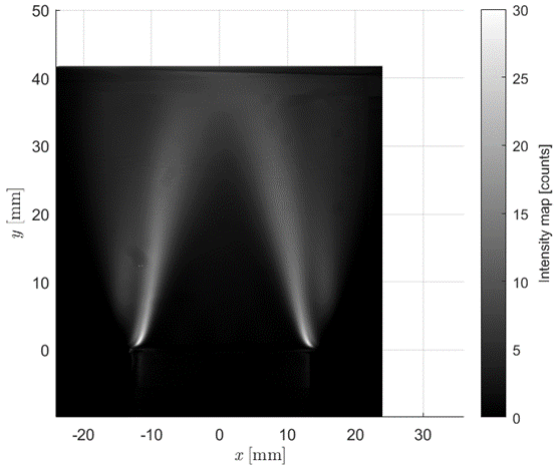

Figure 5.16: Visualization of averaged central vertical slice. The averaged central vertical slice is obtained by averaging the 150 instantaneous central vertical slices of a reconstructed 100% DNG flame at Re = 2300.

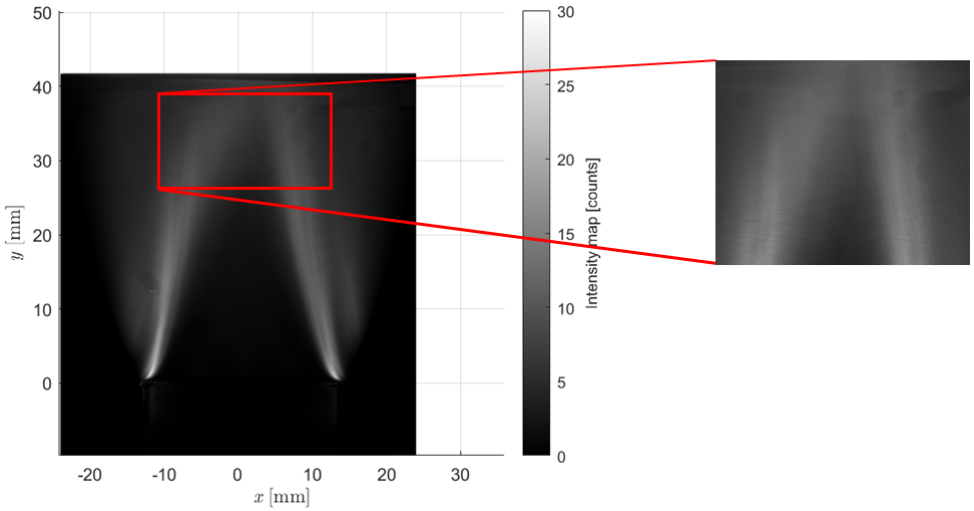

Figure 5.17: Left: Visualization of averaged central vertical slice. The averaged central vertical slice is obtained by averaging the ten instantaneous central vertical slices (prior to the event of flashback) of a reconstructed 100% DNG flame at Re = 2300. Right: A zoomed-in image of the top section of the flame (y > 25 mm) as pointed out by red highlights (visual aid and not a computed quantity). A subtle tilt of the flame towards the right side can be seen in this zoomed-in image.

overall average of vertical slices for this specific case or the previous two cases. These interpretations are derived from the examination of central vertical slices of the reconstructed flame. To validate and uncover additional characteristics related to the events before the onset of the flashback, horizontal slices were also obtained at various heights above the quartz tube rim (see Figure 5.5 to identify the heights above the rim at which the horizontal slices have been taken). Figure 5.18 presents the instantaneous horizontal slices extracted from the reconstruction of the last seven sequentially recorded 100% DNG flame (at Re = 2300) images prior to the event of flashback. As depicted in Figure 5.18, particular red dashed highlights (Note: These red dashed highlights are visual aids and not computed quantities) have been utilized to draw attention to specific features. The distinctive features are mainly the wrinkles in the flame front which seem to be more pronounced as compared to the wrinkles in the previous two discussed cases (100% DNG at Re = 3500 and Re = 2750). Furthermore, these wrinkles exhibit an inward displacement toward the center. Similar to the trend observed during the analysis of the central vertical slices of the reconstructed flame, a comparable pattern emerges from the horizontal slice images. The displacement of the flame is more pronounced from the left side, as evident from the sequential images of the horizontal slice of the flame at y/D_b = 1.19. In fact, even when observing wrinkles at different heights their inward displacement is more prominent from the left section of the flame.

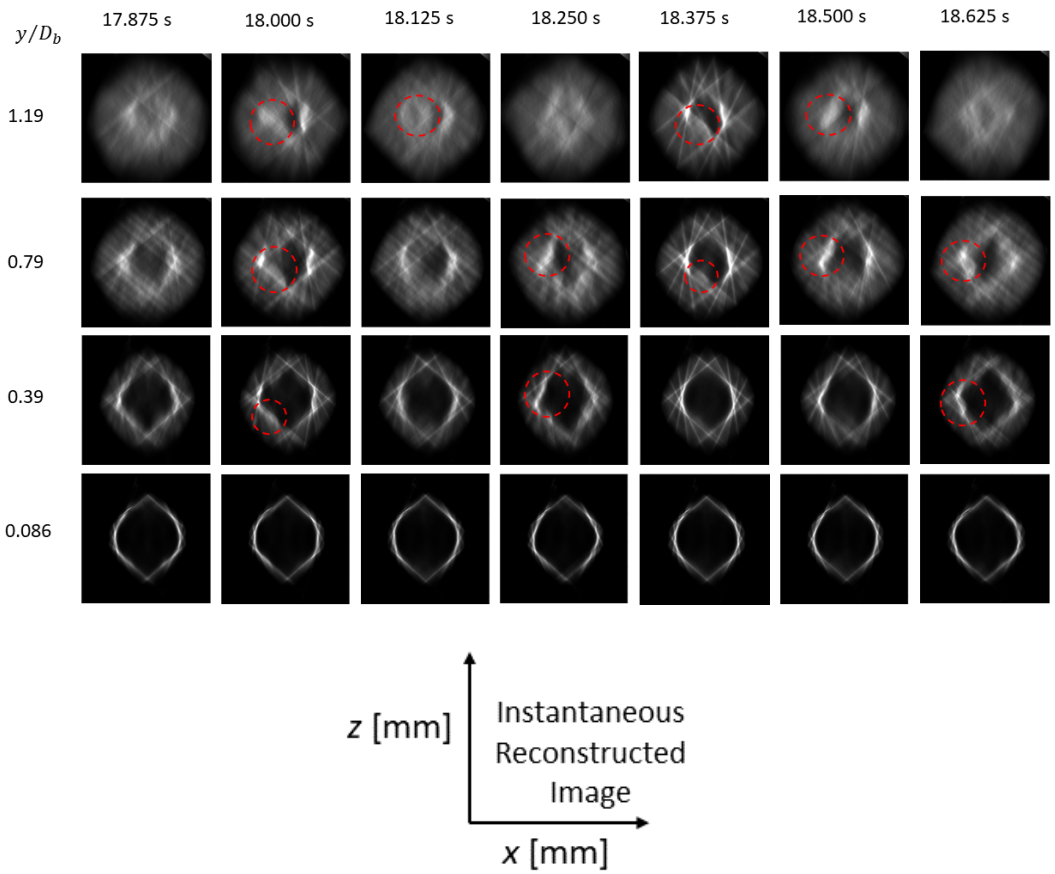

Figure 5.18: Visualization of instantaneous horizontal slices. The horizontal flame slices have been extracted at different heights above the quartz tube rim, where the heights are non-dimensionalized by the inner diameter (D_b) of the quartz tube. These seven slices at each height have been extracted from reconstructions of seven sequentially recorded images of a 100% DNG flame at Re = 2300 before the event of a flashback. In a few of these images, the red dashed highlights (visual aids and not computed quantities) indicate the wrinkles of the flame displacing inwards, particularly from the left section of the slice.

For example, when examining the horizontal slices at 18.00 seconds, it becomes apparent that at y/D_b = 0.39, there is a wrinkle on the left side moving inward, as indicated by the red dashed highlights. As we shift our focus downstream, it becomes evident that this wrinkle continues to move inward, affecting the left side of the flame more significantly. This suggests that the flame is getting disturbed more from the left side. Therefore, it can be speculated for this particular experiment, and from the reconstruction results obtained here that a flashback might have initiated from the left section of the flame. However, it is important to acknowledge that definitive confirmation of the location of the initiation of the flashback is challenging due to the limitations of the low imaging frame rate, which prevented capturing of all flame activities for conducting tomographic reconstruction. Moreover, it is crucial not to make the assumption that the flashback will always originate from the left section for 100% DNG flames. Flashback exhibits stochastic behavior and it is the experiments conducted in this study, along with the obtained reconstruction results, which suggest that the flashback might have been triggered from the left section due to heightened activities observed in the wrinkles of the flame front. Additionally, in order to confirm that the case depicts the condition with an even more diminishing inner area surrounded by the flame front region as compared to previous cases, all 150 instantaneous horizontal slices of reconstructed flame images were averaged. Figure 5.19 presents these averaged horizontal slices at different dimensionless heights above the quartz tube rim. On comparing the averaged horizontal slice at y/D_b = 1.19 for the three 100% DNG cases (for reference see Figures 5.9,5.13 and 5.19), it can be noticed that the inner area surround by the flame front (as identified by regions with high-intensity values or bright white color) has reduced the most in the present case of 100% DNG at Re = 2300, indicating that the tip of the cone has displaced the most towards the quartz tube rim as compared to previous two cases.

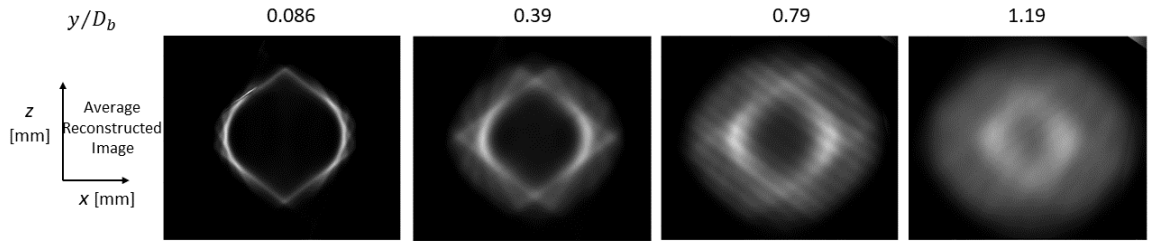

Figure 5.19: Visualization of the averaged horizontal slice at different dimensionless heights above the quartz tube rim. The averaged horizontal slice is obtained by averaging the 150 instantaneous horizontal slices of 100% DNG flame at Re = 2300 at each corresponding dimensionless height above the quartz tube rim.

Having examined the reconstruction results from the 100% DNG flame cases, and recognizing the potential of CTC, the technique was then applied to study hydrogen flames.

Case 4: 50% H_2 and 50% DNG flame at Re = 9000

In Section 5.1 it was discussed how hydrogen flames have a significant contribution of their chemiluminescence intensity in the Ultraviolet range of the spectrum, therefore making it difficult for the cameras that are not equipped with UV-transparent lenses to record chemiluminescence of the hydrogen flame. Thus, it was already anticipated that the reconstruction of the 50% hydrogen and 50% DNG flame might yield somewhat noisy outcomes. However, analyzing this case was crucial to assess the reconstruction quality, with the expectation that certain distinctive features of hydrogen flames could still be discernible at least when blended with DNG. It is also important to highlight, that to make a fair comparison and understand the scope of improvement in the employed setup itself the input parameters (measurement volume dimensions) for reconstructing the flame in the Tomographic-PIV module of DAVIS were kept the same as in the cases of DNG flames.

Figure 5.20 showcases the instantaneous central vertical slices obtained from the reconstructions of ten flame (50% Hydrogen and 50% DNG) images recorded sequentially. The images are at an interval of 0.4s based on the recording rate of the cameras. The impact of the low chemiluminescence strength is evident in the reconstruction outcomes, justifying the compression of the intensity map from a range of 0-30 counts to 0-5 counts for better visualization. On closer examination, the central vertical slices do not exhibit a cone shape originating directly from the quartz tube rim, as seen in the case of pure DNG. Instead, the flame appears to maintain a more or less parallel straight-line configuration until a certain point downstream, after which it gradually forms the cone shape. This has been highlighted in Figure 5.20 using the red dashed highlights (Note: These red dashed highlights are visual aids and not computed quantities). Furthermore, contradicting the conclusion drawn by Halter et al. [10] that an increase in hydrogen content leads to a reduction in flame front thickness, the presented reconstruction results suggest otherwise. This discrepancy can be attributed to the limited availability of chemiluminescence emissions from the flame front as a result of employing cameras not equipped with UV-transparent lenses. In this case of 50% Hydrogen and 50% DNG flame, the high-intensity region is influenced more by emissions from exhaust gas (such as water vapor emissions) rather than the chemiluminescence of the flame. Therefore, the region typically identified as the flame front (the region earlier identified with high-intensity values or bright white colors) looks extremely smeared due to the influence of these exhaust gas emissions. However, it still can be concluded that the flame front (with a reasonable thickness relating to a hydrogen flame) will follow a somewhat similar shape of forming a cone-like structure after a certain distance from the burner/quartz tube rim. This is because the exhaust gas emissions near the flame front (which is not visible but is otherwise present), appear to have this particular shape.

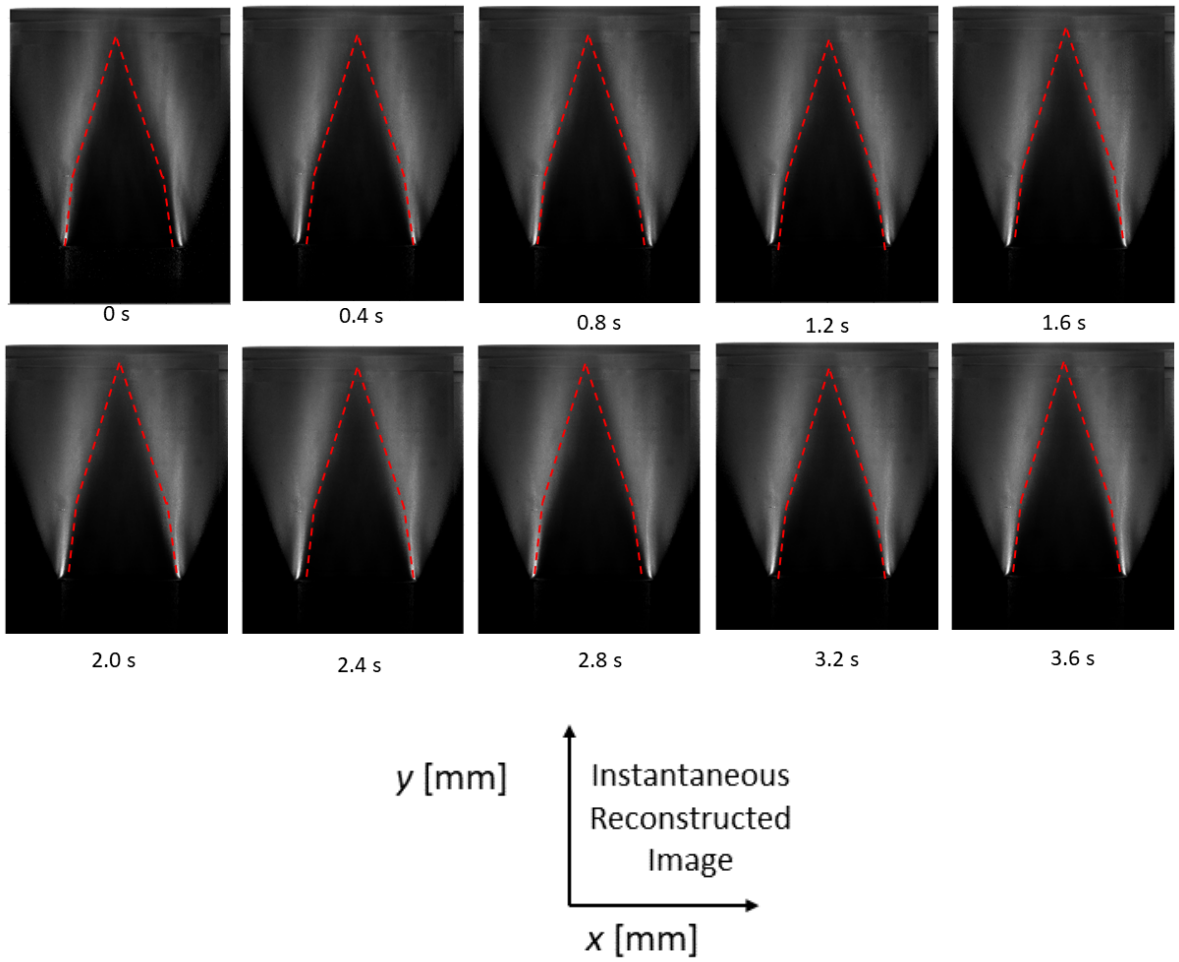

Figure 5.20: Visualization of instantaneous central vertical slices. These ten slices have been extracted from reconstructions of ten sequentially recorded images of a 50% Hydrogen and 50% DNG flame at Re = 9000. The time interval between each image is 0.4s as per the recording rate of the imaging device. The red dashed highlights (visual aids and not computed quantities) marked in the images attempt to indicate that the cone shape by the flame is taken after a certain height (y) from the quartz tube rim.

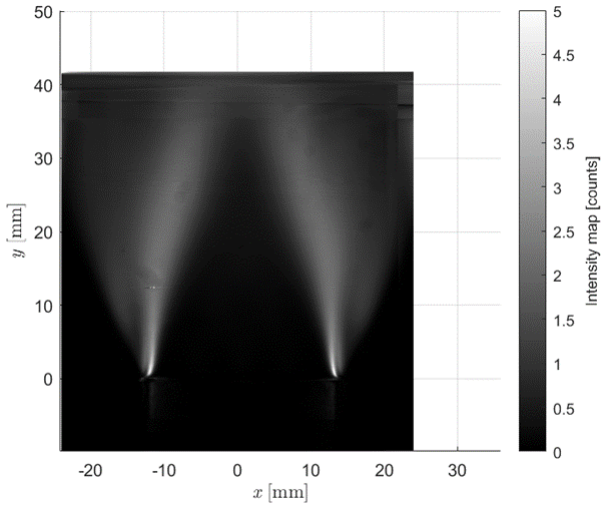

Figure 5.21: Visualization of averaged central vertical slice. The averaged central vertical slice is obtained by averaging the 150 instantaneous central vertical slices of a reconstructed 50% Hydrogen and 50% DNG flame at Re = 9000.

The formation of a cone-shaped flame after a certain distance can be attributed to the high flow velocity in this scenario. With a Reynolds Number of 9000, the flame emerges from the burner as a high-velocity jet and gradually transforms into a cone shape. These observations are based on the instantaneous central vertical slices from reconstructed flame images. However, to confirm if this trend is a part of all the reconstructed flame, an average of all the 150 central vertical slices of the reconstructed flame was taken. Figure 5.21 presents the averaged central vertical slice from the reconstructed flame image. The averaged flame shape depicted in Figure 5.21 also demonstrates the initiation of cone formation slightly above the rim of the quartz tube. Therefore it can be concluded that such a configuration is consistent throughout the recorded images of 50% Hydrogen and 50% DNG flame. As previously emphasized, relying solely on central vertical slices may overlook crucial details of the complex structure of flame. To conduct a more detailed analysis, horizontal slices were also extracted from the reconstructed flame at various heights (see Figure 5.5 to identify the heights above the rim at which the horizontal slices have been taken). Figure 5.22 presents the instantaneous horizontal slices extracted from the reconstruction of seven sequentially recorded 50% Hydrogen and 50% DNG flame (Re = 9000) images. It is worth emphasizing that for this case involving hydrogen flames, the intensity map values were kept within the range of 0-5 counts for a height of 2.17 mm and 0-3 counts for a height of 10 mm, 20 mm, and 30 mm. Upon inspecting the reconstructed images, a noticeable distinction in the quality of the obtained results between pure DNG and hydrogen-blended DNG flames becomes evident. Even at a height close to the quartz tube rim (y/D_b = 0.086), where the influence of exhaust gas emissions is significantly diminished compared to other heights, the reconstructed chemiluminescence distribution appears considerably noisy. However, it does manage to approximate the circular shape (in the regions of reliable reconstruction results) consistent with the structure of the quartz tube. This provides some optimism that the shapes of flame fronts can still be fairly approximated. Nonetheless, estimating the thickness of the flame front proves challenging since it is unclear what portion of the high-intensity region stems from the chemiluminescence intensity distribution and what fraction originates from the exhaust gas emissions. Further moving away from the burner at y/D_b = 0.39 some interesting features can be observed. The flame front seems to have a finer wrinkled structure as compared to the wrinkled structure of any of the pure DNG cases. This finer wrinkled structure aligns with a common characteristic of flames with hydrogen content [29, 10, 24].

This outcome strongly supports the assertion that tomographic reconstruction remains a valuable technique for extracting fine structures, even under signal strength limitations, but with a somewhat reduced quality as compared to pure DNG flame.

As the observation points shift in the downstream direction, the horizontal slices look even noisier. Indeed, at the y/D_b = 0.79, the wrinkles, while still present, are not captured in a detailed manner. Another notable observation is the densely packed appearance of the horizontal slices, especially at y/D_b = 1.19 to the extent that the edges of these slices seem to almost touch the boundaries of the measurement volume. Considering that the measurement volume has remained consistent across the four cases, therefore, the densely packed appearance of the horizontal slices implies an expanded coverage of the exhaust gas emissions in the present case. This expansion could be a result of increased production of these emissions in the case of hydrogen flames when compared to the cases involving DNG. Hence, these outcomes provide additional confirmation that in the combustion of hydrogen, there is increased production of exhaust gases which may be due to an increased concentration of water vapor in the exhaust gases. In the context of the tomography, it can be concluded that using the same measurement volume for both DNG and hydrogen flames might lead to sub-optimal reconstruction quality, particularly at downstream sections of the flame. The situation of densely packed horizontal slices can also be observed in images of averaged horizontal slices at different dimensionless heights above the quartz tube rim (See Figure 5.23.), especially at y/D_b = 1.19.

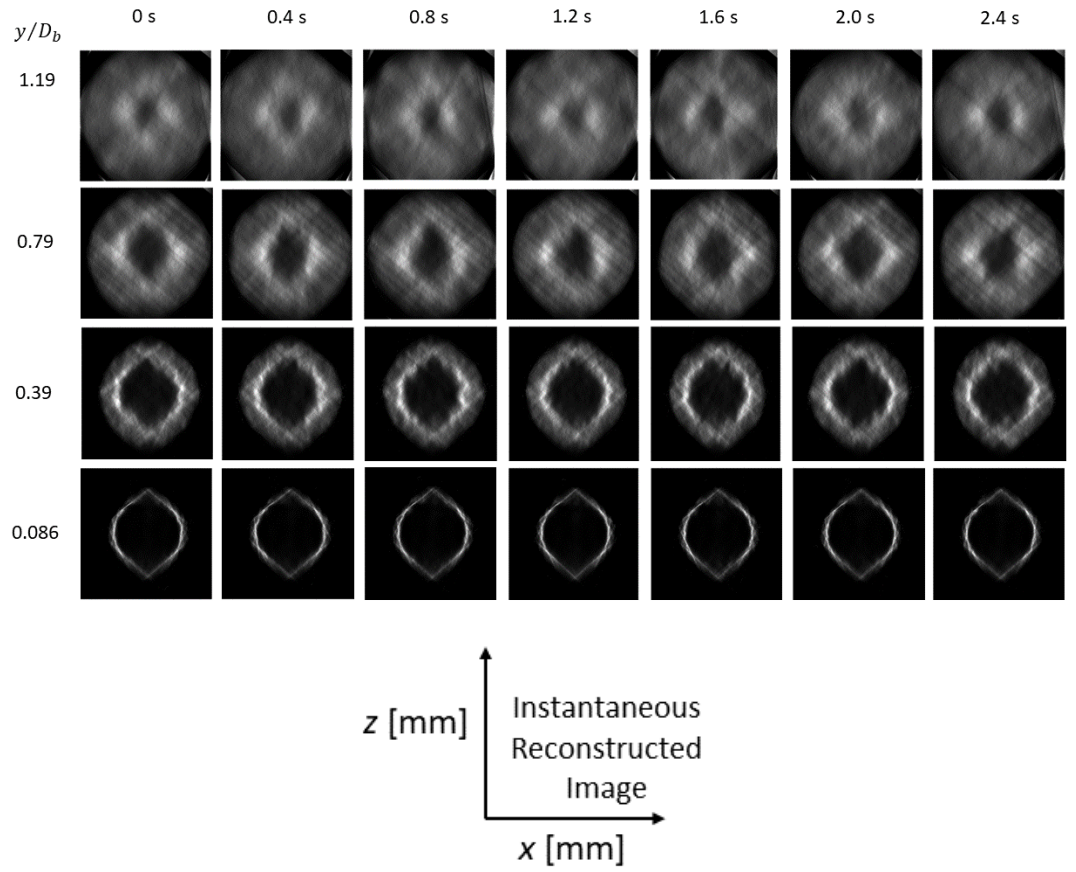

Figure 5.22: Visualization of instantaneous horizontal slices. The horizontal flame slices have been extracted at different heights above the quartz tube rim, where the heights are non-dimensionalized by the inner diameter (D_b) of the quartz tube. These seven slices at each height have been extracted from reconstructions of seven sequentially recorded images of 50% Hydrogen and 50% DNG flame at Re = 9000.

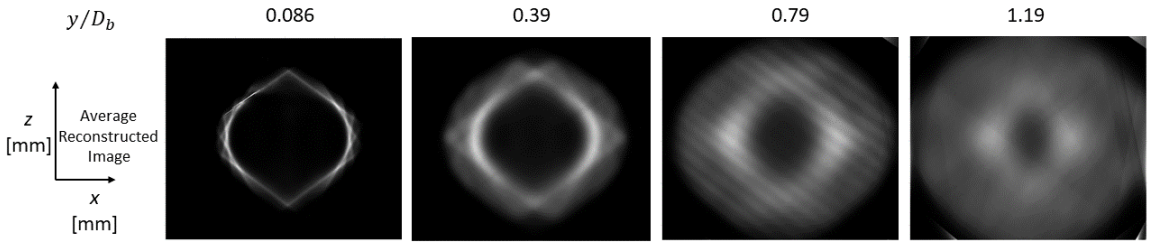

Figure 5.23: Visualization of the averaged horizontal slice at different dimensionless heights above the quartz tube rim. The averaged horizontal slice is obtained by averaging the 150 instantaneous horizontal slices of 50% Hydrogen and 50% DNG flame at Re = 9000 at each corresponding dimensionless height above the quartz tube rim.

The qualitative analysis in the present section, carried out through visual assessments, provides crucial insights into the flame structures. However, to substantiate the accuracy of these interpretations, it was deemed essential to conduct a statistical analysis.

5.2.2. Statistical Analysis

Statistical analysis has been performed on the central vertical slice of the reconstructed flame at the same heights above the quartz tube burner (see Figure 5.5 for identifying these heights) where horizontal slices were extracted in previous cases. The analysis includes an examination of both the average and the standard deviation of the intensity distributions.

Average of intensity distribution

To compute the average intensity distribution, the intensity values of 150 instantaneous central vertical slices were summed together, and each value was divided by 150. Figure 5.24 shows the average intensity distributions as extracted against four heights above the quartz tube rim for all four cases. These plots give the average intensity distribution $\bar{I}$ of the central vertical slice from the reconstructed flame at different dimensionless heights above the quartz tube burner. An initial observation drawn from these plots indicates that the average intensity peaks among the four dimensionless heights reach their maximum at y/D_b = 0.086. Subsequently, these average intensity peaks gradually diminish as the dimensionless height increases. This trend substantiates that in close proximity to the quartz tube rim, the signal strength of chemiluminescence is indeed higher in comparison to the signal strength at greater distances from the quartz tube rim. The same was also observed in the qualitative analysis of the horizontal slices extracted from the reconstructed flame.

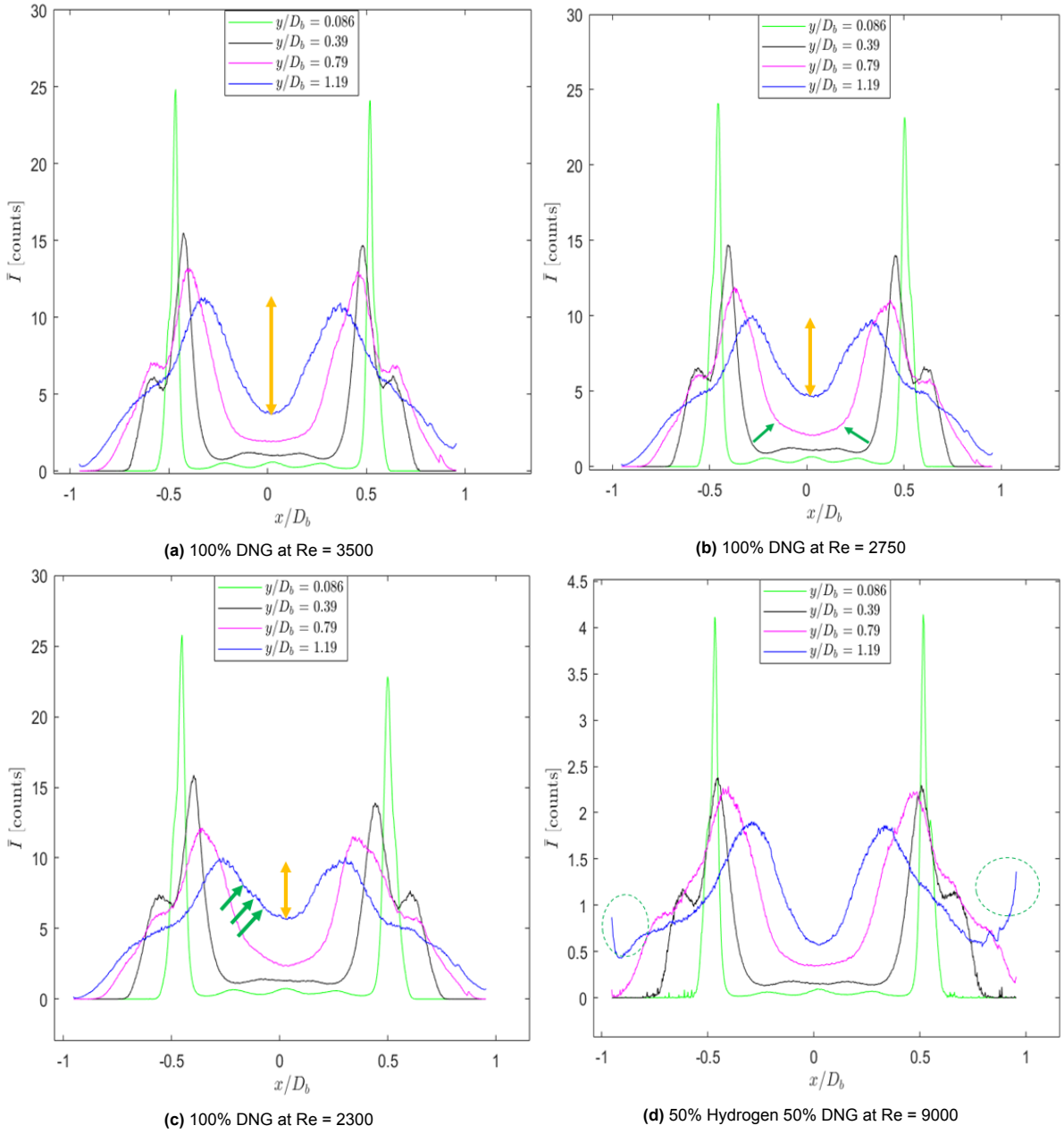

(a) 100% DNG at Re = 3500

(b) 100% DNG at Re = 2750

(c) 100% DNG at Re = 2300

(d) 50% Hydrogen 50% DNG at Re = 9000

Figure 5.24: Average intensity distributions at four different dimensionless heights in a central vertical slice of the reconstructed flame images.

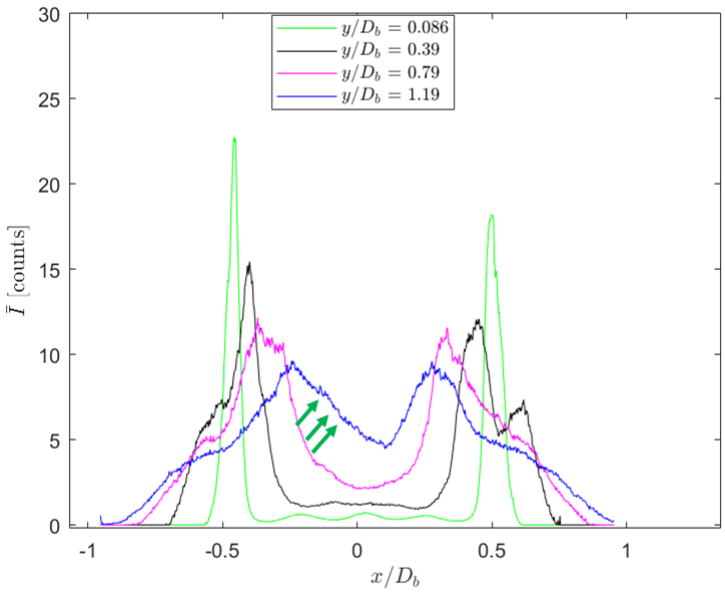

Figure 5.25: Average intensity distribution in the central vertical slices of the reconstruction of the last ten sequentially captured images of 100% DNG at Re = 2300.

Additionally, with increasing heights, the distance between the two peaks appears to be reduced implying a conical geometry of the flame. Now, when observing the plots of the DNG flame at y/D_b = 0.79, it becomes evident that for the DNG flame at Re = 3500, the section (at the bottom) between the two peaks has an approximately flat profile. However, at the same height (y/D_b = 0.79) the section (at the bottom) between the two peaks for the DNG flame at Re = 2750 seems to have a slightly curved profile. This feature has been pointed out with two green arrows in Figure 5.24b. For the case of DNG flame at Re = 2300 section (at the bottom) between the two peaks at y/D_b = 0.79 appears to have an even more pronounced curved profile compared to the other two DNG cases. This difference of having a flat and curved profile suggests that the distance between the two peaks diminishes as the conditions change from stable conditions (Re = 3500) to flashback conditions (Re = 2300). This reduction in the distance between the two peaks implies that the tip of the flame cone has shifted in the upstream direction, signifying that the flame is approaching the flashback condition. This similar deduction of the tip of the cone shifting in the upstream direction with decreasing Reynolds number can be made more clearly from the plots at y/D_b = 1.19. It is notably clear how the distance between the two peaks and the region between them gradually diminishes as the flame approaches the flashback condition. The same has been highlighted with the vertical two-headed orange arrow in all three DNG flame cases. This suggests a reduction in the average intensity difference between the flame front (it is assumed that the flame front emits the maximum chemiluminescence intensity [20], therefore, the highest peaks on both sides correspond to the location of the flame front at every dimensionless height) and the area enclosed within it. Hence, it can be concluded that the tip of the flame cone has indeed shifted in the upstream direction.

Furthermore, on observing Figure 5.24c, it can be noticed that at y/D_b = 1.19, the valley region is slightly towards the right side. The right slope of the plot appears to be slightly steeper than the left slope, as indicated by the three green arrows. It seems that the difference in average intensity between the top left peak (representing the left side of the flame front) and the entire region enclosed by the flame front is diminishing at a faster rate compared to the difference in average intensity between the top right peak (representing the right side of the flame front) and the area enclosed within the entire flame front. To strengthen this deduction, the average intensity distribution at various dimensionless heights above the quartz tube rim within the central vertical slice of the reconstructed flame image was examined for the ten images acquired prior to the flashback event. Figure 5.25 shows this average intensity distribution of central vertical slices from the last ten reconstructed flame images. From the figure, it is even more evident that the slope is less steep on the left side (indicated by three green arrows) than on the right side at y/D_b = 1.19. This suggests that flashback might have initiated from the left side (note that this

deduction is with respect to the experiments conducted in this work and may not be always the case since flashback is a stochastic process). A similar situation was observed with visual assessment from Figure 5.18 in Section 5.2.1.

When examining the average intensity plot (Figure 5.24d) for the case of a 50% Hydrogen and 50% DNG flame, at y/D_b = 1.19, additional rising average intensity can be observed at both the left and right ends unlike at other dimensionless heights where the extremes have close to zero average intensity. This phenomenon has been enclosed within dashed green circles. The observed increase in average intensities at the extremities can be linked to reconstruction artifacts. The production of exhaust gases in hydrogen flame was more than in any of the DNG flame cases (may be due to increased concentration of water vapor). Consequently, the specified reconstruction volume dimensions could contain the entire flame region for the DNG flame, without making it appear densely packed. However, the reconstruction volume size was insufficient to fully accommodate the entire hydrogen flame region (especially in the downstream direction). As a result, there was some light intensity in the images which originated from regions outside the reconstruction volume. The tomographic reconstruction algorithm tried to distribute these intensity values within the reconstructed flame volume, and this process resulted in the appearance of artifacts at the boundaries. Therefore, when analyzing the intensity distributions these spikes at the boundaries can be ignored. Furthermore, a decrease in intensity levels becomes notably apparent in the case of hydrogen flame (Figure 5.24d). As in the plots of previous cases of DNG flames, here as well the two peaks (left and right) decrease with increasing dimensionless heights. However, on comparing the peak locations at y/D_b = 0.086 and y/D_b = 0.39 (on both left and right sides), it can be noticed their x/D_b values appear almost equal. This suggests between these two heights the hydrogen flame front does not shift a lot which is clearly not the case with DNG flames (observe the x/D_b values of peaks on both sides at different dimensionless heights for DNG flames). Such a difference may be because of the difference in shapes of the pure DNG (formation of cone-like shape from the quartz tube rim) and hydrogen blended with DNG flames (jet-like shape near the quartz tube rim exit till a certain height from the rim and then takes a cone-like shape).

Standard deviation of intensity distribution

The standard deviation serves as a measure of data dispersion in relation to the mean. A low standard deviation implies that the data is tightly clustered around the mean, while a high standard deviation indicates that the data is more widely scattered. In the context of the present work, the standard deviation values represent the spread of intensity values at different heights of the central vertical slice extracted from the reconstructed flame image. To compute the standard deviations σ Equation 5.1 was used. In this equation, I represents the instantaneous intensity distribution, $\bar{I}$ denotes the average intensity distribution, and N represents the number of reconstructed images.

$$\sigma(I) = \sqrt{\frac{\sum(I - \bar{I})^2}{N - 1}} \tag{5.1}$$

Based on Equation 5.1 the standard deviations were calculated and Figure 5.26 presents the standard deviations of the intensity distribution at various heights above the quartz tube rim of the central vertical slice from the reconstructed flame image. The figures have profiles quite similar to the average intensity plots with two peaks on the sides representing the location of the flame front and the region between them representing the area enclosed within the flame front. Higher peak standard deviation values at y/D_b = 0.086 can be expected due to the greater chemiluminescence intensity value near the quartz tube rim compared to heights further away from it.

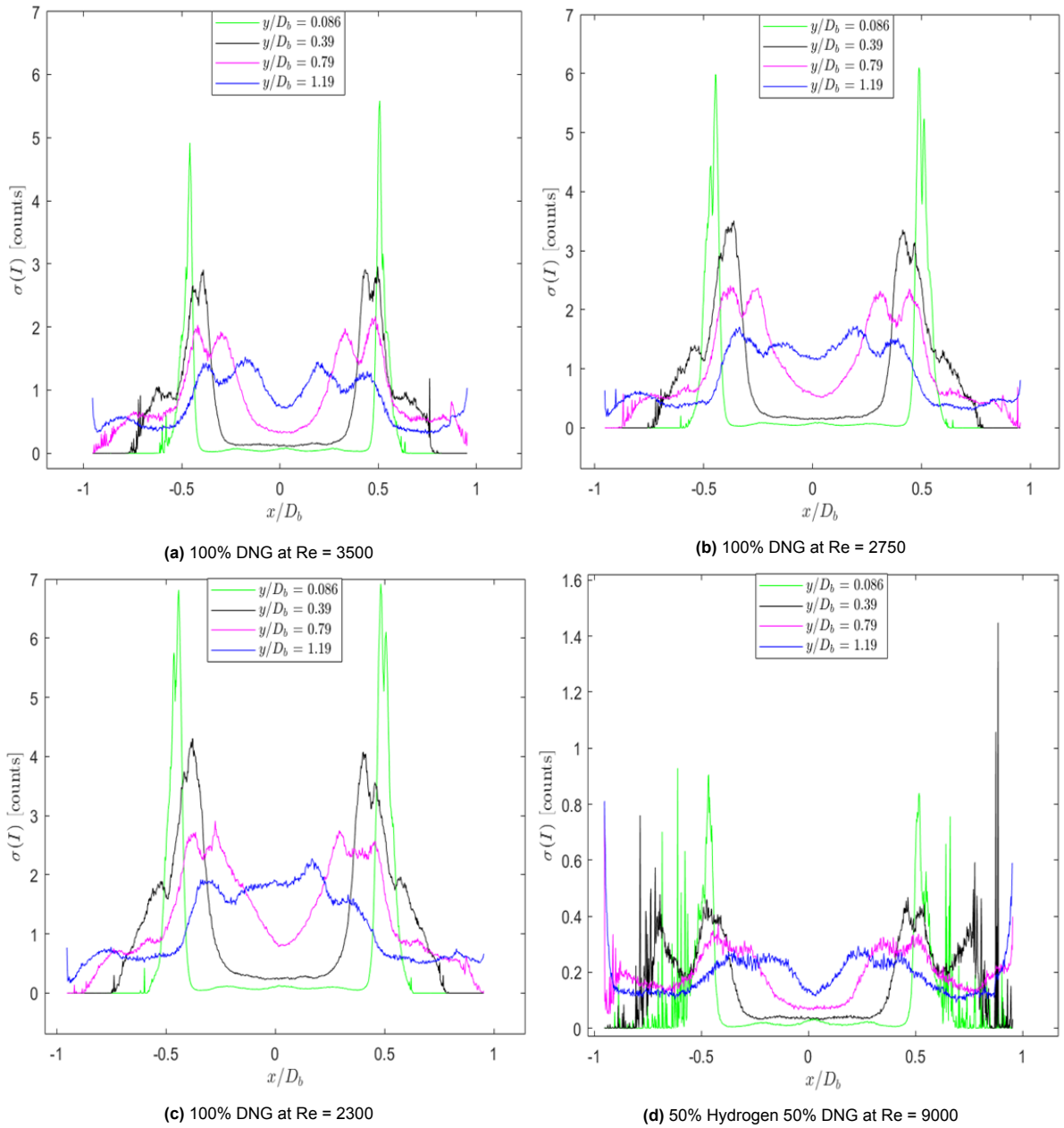

(a) 100% DNG at Re = 3500

(b) 100% DNG at Re = 2750

(c) 100% DNG at Re = 2300

(d) 50% Hydrogen 50% DNG at Re = 9000

Figure 5.26: Standard deviations of intensity distributions at four different dimensionless heights in the central vertical slice of the reconstructed flame images.

Examining Figure 5.26a, it becomes evident that each peak (both left and right) appears to split into two with a valley in between them. This is seen for all heights. It suggests that the flame front oscillates around its mean position which is associated with the wrinkles seen in the instantaneous horizontal slices, and the prominence of these oscillations increases with height. This is indicated by the more pronounced splitting of peaks when moving in the downstream direction.

If this interpretation of the double peaks in terms of flame front oscillations, is accurate, then the location of the valleys between these split σ- peaks (left and right) should be close to the location of the average intensity peak (both left and right). The locations of the peaks at the two extremes in the average intensity plots (refer to Figure 5.24a) at different heights above the rim have been summarized in Table 5.4 and the location of the valleys at two extremes in the standard deviation plots (refer to Figure 5.26a) at different heights above the rim have been summarized in Table 5.5. Comparing the values in Table 5.4 and Table 5.5, it becomes apparent that the locations of peaks from average intensity plots and

valleys from standard deviation plots are indeed close. With this, it can be confirmed that the double σ-peak is consistent with an oscillating flame front. Additionally, the widening separation between these split peaks at greater distances from the quartz tube rim indicates an increase in the amplitude of oscillations and hence the amplitude of wrinkles. This supports the earlier observation that these wrinkles become more prominent with an increasing distance from the quartz tube rim.

Dimensionless heights above quartz tube rim (y/D_b)	**Location on the x-axis of the left peak (x/D_b)**	**Location on the x-axis of the right peak (x/D_b)**
0.39	-0.42	0.48
0.79	-0.4	0.45
1.19	-0.31	0.36

Table 5.4: Average intensity peak value locations (non-dimensionalized by the inner diameter of quartz tube) for 100% DNG flame at Re = 3500.

Dimensionless heights above quartz tube rim (y/D_b)	**Location on the x-axis of the left peak (x/D_b)**	**Location on the x-axis of the right peak (x/D_b)**
0.39	-0.41	0.47
0.79	-0.36	0.4
1.19	-0.31	0.32

Table 5.5: Valley locations (non-dimensionalized by inner quartz tube diameter) from the standard deviation plots for 100% DNG flame at Re = 3500.

Additionally, It can be noticed in the other two standard deviation plots of the 100% DNG flame at Re = 2750 and Re = 2300, that there is an increase in the number of fluctuations (smaller peaks) in these split peaks. This may be due to the presence of noise or an increased number of oscillations. Furthermore, it is important to note that the overall standard deviation values in the central vertical slice image of a reconstructed 100% DNG flames show a noticeable increase as the Reynolds number decreases. This indicates that the intensity distribution deviates more from the average intensity values as the Reynolds number decreases for flames with the same composition.

Given that the intensity scale for the hydrogen flame significantly differs from that of the DNG flame, limited insights can be drawn from the standard deviation plots of the hydrogen flame. However, the overall profile does exhibit similarities to the standard deviation profiles of the DNG flames.

Intensity distributions: Recorded vs Reconstructed images

The average and standard deviation intensity profiles analyzed previously (Figure 5.24 and 5.26) were based on the intensity distribution of the central vertical slice of the reconstructed image. They give important insights into the features of the flame (such as oscillating flame front, cone shape of flames, and tilting of the flame). However, to confirm if indeed there is an advantage of performing 3-D reconstruction, profiles of the average and standard deviation of the intensity from the recorded images were also evaluated. The analysis has been performed for all four flame images as acquired by Camera 3. The average and standard deviation values have been calculated in the same way as was done previously for the reconstructed images. Figure 5.27 presents the average intensity distributions as extracted against four heights above the quartz tube rim for the images recorded from Camera 3.

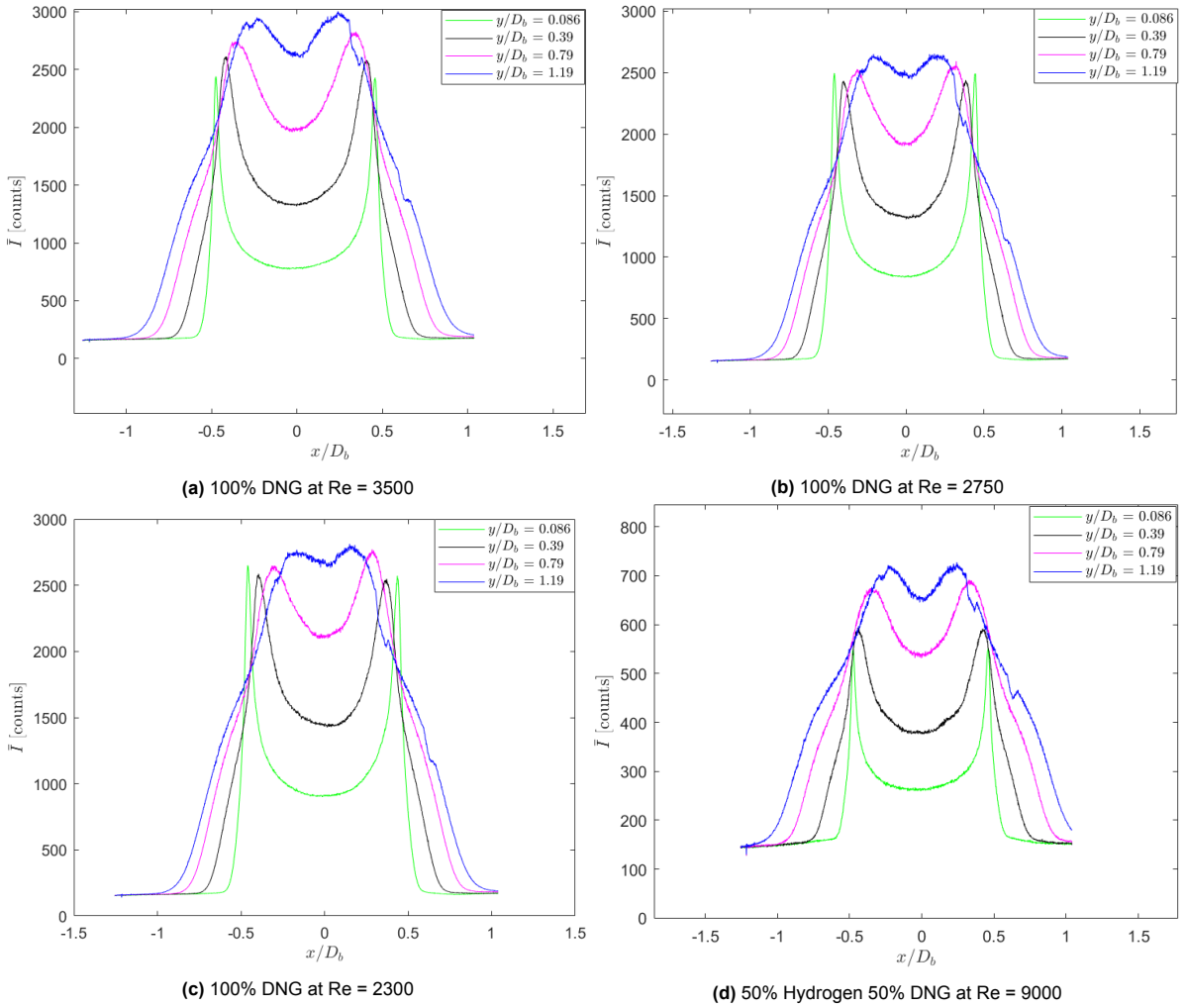

(a) 100% DNG at Re = 3500

(b) 100% DNG at Re = 2750

(c) 100% DNG at Re = 2300

(d) 50% Hydrogen 50% DNG at Re = 9000

Figure 5.27: Average intensity distributions at four different dimensionless heights in the image captured by Camera 3.

The observed trend in the figure, where the average intensity peaks (both left and right) do not necessarily decrease with increasing height, contradicts what was observed in the analysis of the reconstructed images (see Figure 5.24). This discrepancy can be explained by the nature of the recorded images, which essentially represent projections or depth-integrated intensities. Near the downstream of the flame, there is a large flame volume with low-intensity values, but because these low values are integrated over the entire depth, the intensity values can still appear high. On the other hand, near the rim, although the intensity values are high, the flame volume is smaller (due to the thin flame front), resulting in lower integrated intensity values compared to the top sections. The reconstructed images, on the other hand, provide a more accurate representation of the expected intensity distribution within the flame (where the highest intensity peaks are for regions close to the rim). Figure 5.28 presents the standard deviations of the intensity distribution at various heights above the quartz tube rim of images recorded by Camera 3.

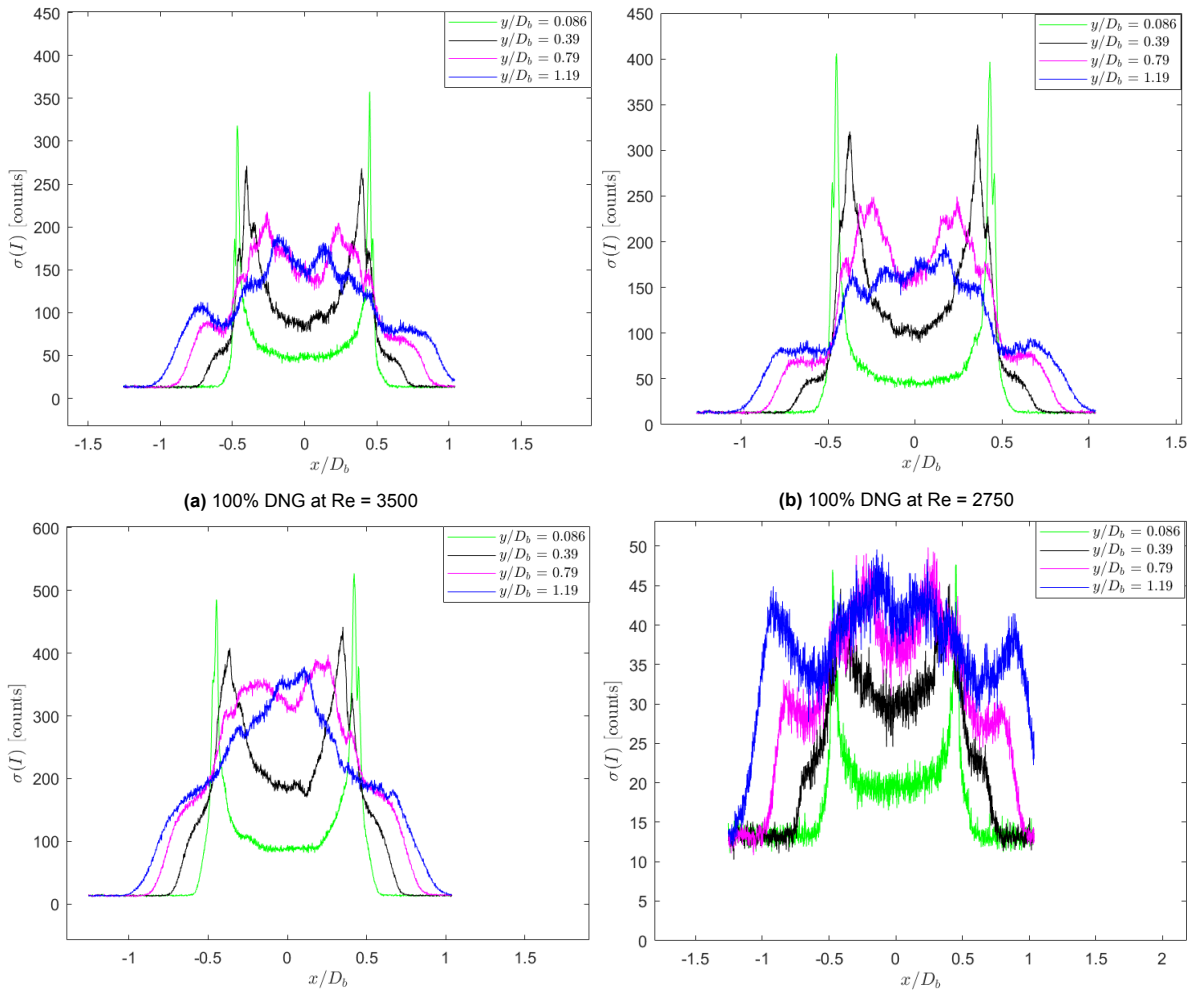

(a) 100% DNG at Re = 3500

(b) 100% DNG at Re = 2750

(c) 100% DNG at Re = 2300

(d) 50% Hydrogen 50% DNG at Re = 9000

Figure 5.28: Standard deviations of intensity distributions at four different dimensionless heights in the image captured by Camera 3.

From standard deviation plots of the recorded images, it can be observed that the split double peaks representing oscillating flame front are not very evident. These split double peaks were clearer in the standard deviation plots of the reconstructed images (Figure 5.26). Moreover, near the rim, the core is not expected to have chemiluminescence emissions (zero mean and standard deviation values), which is approximately the case for reconstructed images but can not be observed in the intensity distributions of the recorded images.

Based on the differences between the intensity profiles of recorded and reconstructed images it can be confirmed that the reconstructed images provide insights that can be expected from the real physical structure of the flame at different conditions (different Reynolds numbers). Therefore, indeed there is an added advantage of performing 3D reconstruction to study the structure of flame.

5.2.3. Cone Angles

To further assess the reliability of the reconstruction results in providing an accurate representation of the flame structure, the cone angle, was determined. The cone angle was computed using the averaged central vertical slice of the reconstructed flame. For the cases of 100% DNG at Re = 3500 and 2750 and 50% Hydrogen and 50% DNG flame, the averaged central vertical slice considered was obtained by averaging the 150 instantaneous central vertical slice of the reconstructed flame images recorded sequentially. Whereas for 100% DNG at Re = 2300, the averaged central vertical slice presented here was obtained by averaging the last ten instantaneous central vertical slices of the reconstructed flame

images captured sequentially prior to the event of the flashback. In all cases, the procedure involved identifying the maximum intensity points towards the positive and negative x-direction at various heights. This approach was adopted with the understanding that the maximum intensity points would correspond to different locations on the flame front. Then two straight lines were fitted through these located points. Consequently, it allowed for tracking the slope of the flame front. With the dimensions of the slope, the cone angle (2α) was calculated as:

$$2\alpha = tan^{-1}\left(\frac{1}{m_1}\right) + tan^{-1}\left(\frac{1}{m_2}\right) \tag{5.2}$$

In Equation 5.2 2α is the cone angle, m_1 and m_2 are the two slopes corresponding to the left and right slope of the flame front. The angles have been calculated in degrees.

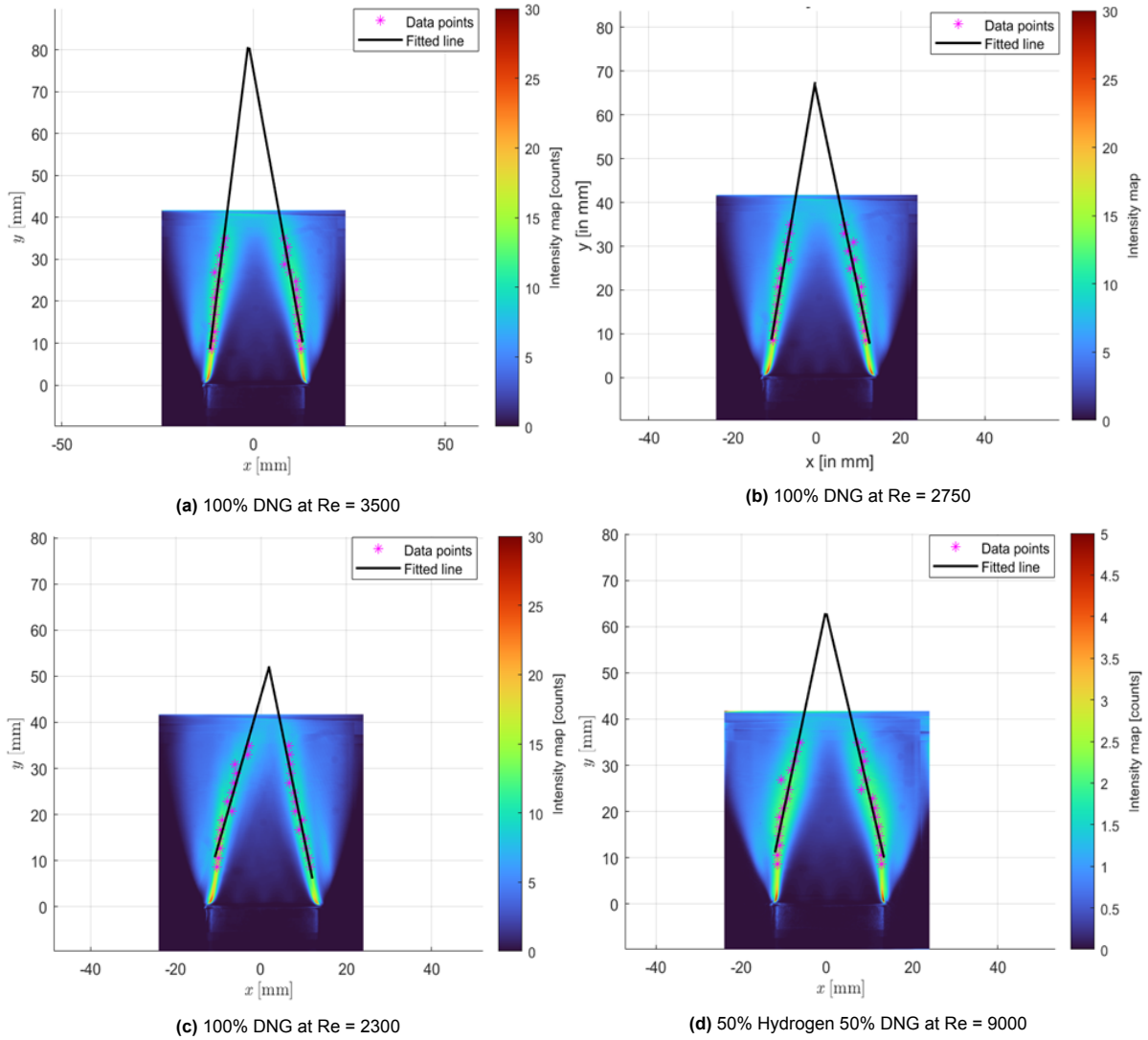

(a) 100% DNG at Re = 3500

(b) 100% DNG at Re = 2750

(c) 100% DNG at Re = 2300

(d) 50% Hydrogen 50% DNG at Re = 9000

Figure 5.29: Cone shape representation through fitted lines in the vertical slices from the average central vertical slice of reconstructed flame.

Case Number	Fuel	Equivalence Ratio	Fuel composition (by volume fraction)	Reynolds number	Cone Angle (degree)
1.	DNG	1	100%	3500	19.01
2.	DNG	1	100%	2750	22.46
3.	DNG	1	100%	2300	29.60
4.	Hydrogen and DNG	1	50% H_2 50% DNG	9000	27.07

Table 5.6: Cone Angles.

Based on Equation 5.2, the cone angles obtained have been summarized in Table 5.6. From the values obtained, it can be noticed that with a decrease in the Reynolds Number for 100% DNG flame, the cone angle increases, indicating that the cone is shifting upstream towards the quartz tube rim. This observation aligns with the findings of qualitative and statistical analyses in this study. Furthermore, in previous studies as well ([16], [9]), it was observed that the average cone angles of flames with the same composition increased as the Reynolds number decreased. Additionally, the value of cone angle for a 50% hydrogen and 50% DNG flame is higher than the 100% DNG flames at Re = 3500 and 2750, which indicates that hydrogen flame may be slightly wider and this may be due to the highly diffusive nature of hydrogen.

6

Conclusion and future work

6.1. Conclusion

The present work was performed to obtain the 3D topology of a Bunsen burner flame using Computed Tomography of Chemiluminescence. Three cases of pure (100% DNG by volume fraction) DNG flame at different Reynolds numbers corresponding to stable, close to flashback and flashback conditions have been studied. Additionally, a case of 50% by volume fraction hydrogen blended with 50% DNG flame was also studied. The 3D structure for all four cases was obtained using the technique of computed tomography of chemiluminescence. Based on the results obtained from CTC, it can be concluded that the technique is effective and capable of providing valuable insights into the structure of flame. While the image acquisition step was conducted on 100% DNG at various Reynolds numbers, hydrogen at various volume fractions blended with DNG, and 100% Hydrogen flames, the reconstruction process only considered four cases: 100% DNG at Re = 3500 (stable), 100% DNG at Re = 2750 (close to flashback) and 100% DNG at Re = 2300 (flashback) and 50% Hydrogen and 50% DNG flame. The decision to exclude flames with a higher hydrogen composition from reconstruction was due to a decreased visibility of the hydrogen flame. The cameras used in this study were not equipped with UV-transparent lenses. Since a significant contribution of the chemiluminescence intensity from the hydrogen flame falls within the UV range of the spectrum, it was not possible to capture the entire chemiluminescence intensity. This limitation resulted in reduced visibility of the flame as the hydrogen content increased. Given that the quality of the reconstruction results depends largely on the quality of the acquired input images, it was considered preferable in the case of hydrogen flames to focus only on the case of 50% hydrogen blended with 50% DNG. This approach aimed to achieve less noisy and reasonably good quality reconstructions, facilitating an examination of flame features. The reconstruction results were analyzed using a sequence of methods: qualitative analysis, statistical analysis, and quantification of the cone angle of the reconstructed flame.

In the qualitative analysis visual assessment of the reconstructed flame was conducted both on its central vertical slice and horizontal slices extracted at different heights above the quartz tube rim. In the case of 100% DNG flame with a decreasing Reynolds number, distinctive streak-like features emerged in the central vertical slice of the flame front region, suggesting an increase in flame front activity or the possible presence of pronounced wrinkles. Furthermore, in the case of a flashback, the central vertical slices just moments before the flashback displayed a slight tilt towards the right side, indicating heightened activity on the left side or the possible initiation of the flashback from the left side. These observations regarding increased pronounced wrinkles and speculations about the onset of flashbacks from the left side were subsequently studied through the analysis of horizontal slices of the flame. When examining the horizontal slices of the flame, it indeed was observed that the flame front displayed more pronounced wrinkles compared to the flame fronts of the 100% DNG flame at Re = 3500 and 2750. Additionally, the frequent inward displacement of wrinkles towards the center suggested that the flashback might have started from the left side of the flame. The vertical and horizontal slices of hydrogen flames were also analyzed. As expected, the reconstruction results exhibited a high level of noise. Despite the noisy results, the discernible difference in flame structure between hydrogen and DNG, characterized by finer wrinkles in the hydrogen flame front, was evident.

The results of the visual assessment were subsequently validated by the findings from the statistical analysis of the intensity distribution in the central vertical slice of the reconstructed image. The average intensity plots offered additional evidence to support the conclusions drawn regarding the conical shape of the flame, the increasing shift in the tip of the cone towards the quartz tube rim with decreasing Reynolds number, and the tilting of the flame towards the right side during events before flashback. Furthermore, the standard deviation plots helped recognize the presence of oscillating flame fronts which can be associated with the wrinkles in the flame front. A brief comparative statistical analysis between the intensity distributions of recorded images by Camera 3 and the central vertical slice of the reconstructed images further revealed the added advantage of performing 3D reconstructions to study the structure of the flames.

Finally the cone angles were calculated from the averaged central vertical slice of the reconstructed flame for all four cases. The values of cone angles were observed to decrease for 100% DNG flame with increasing Reynolds number implying the shifting of the tip of the cone upstream towards the quartz tube rim. It was also noticed that the cone angle of 50% hydrogen blended with 50% DNG flame at a Re = 9000 was greater than the cone angle of 100% DNG flame at Re = 3500 and 2750 indicating the diffusive nature of hydrogen flames.

6.2. Future Work

While the goal of uncovering the structure of premixed pure hydrogen flame at flashback may not have been achieved in this thesis, the work has provided valuable insights, indicating that the objective is within reach with certain enhancements and refinements. This section, therefore, highlights improvements that can be made in the current experimental setup and reconstruction outcomes.

6.2.1. Recommendation for experimental setup

The current experimental configuration utilizes six cameras. Future work could involve expanding the setup to include eight or more cameras, arranged with different angular distributions, to explore potential improvements in the resulting image acquisition and reconstruction outcomes. Once the optimal number of cameras is established, further enhancements can be pursued by considering the changes to the type of camera itself. In the present study, Imager LX has been employed due to its compact size and other advantages as mentioned in Chapter 4 (Section 4.1.2). However, they are low-speed cameras. This led to a substantial loss of information, particularly the details of flame propagation during flashback. Therefore, for enhanced future results, it is suggested to explore options such as employing compact-sized high-speed cameras or potentially constructing an endoscopic CTC setup using fiber bundles and high-speed cameras, drawing inspiration from the work of Liu et al. [23].

Moreover, in future experiments, it is advisable to explore the implementation of colored glass filters, such as Schott BG40 [20], to effectively suppress exhaust gas emissions, thereby enhancing the precision of chemiluminescence signals. Furthermore, since a substantial portion of chemiluminescence intensity emitted by hydrogen flame resides in the ultraviolet (UV) spectral wavelength region, careful consideration should be given to utilizing UV-transparent lenses for the cameras.

6.2.2. Recommendation for flame reconstruction

Upon finalizing all aspects of the experimental setup, potential improvements can be sought in the subsequent step of CTC, which involves flame reconstruction. In the current study, emphasis was placed on utilizing the Multiplicative Algebraic Reconstruction Technique (MART), as an iterative algebraic reconstruction algorithm. However, in the subsequent project phase, exploration of alternative algorithms, including those mentioned at the end of Chapter 3 such as the Evolutionary Reconstruction Technique (ERT) and artificial intelligence-integrated approaches like Neural Volume Reconstruction Technique (NVRT), could be undertaken. This step could determine whether there are alternative algorithms capable of unveiling additional intricate flame features that might not be achievable through the MART algorithm.

Apart from obtaining the reconstruction outcomes to attain the 3D structure of flame, there is a scope and need to improve the data analysis part (post-processing) while maintaining computational efficiency. One promising strategy for enhancing both the data analysis of reconstruction outcomes and computa-

tional efficiency lies in the adoption of Convolutional Neural Networks (CNNs). As a specialized class of deep learning algorithms, CNNs are designed to process pixel data, making them well-suited for image recognition and processing tasks. In fact, Convolutional Neural Networks (CNNs) is a proficient pattern recognition tool that may offer a viable approach to successfully identify distinctive flame characteristics closely associated with the phenomenon of flashbacks. Developing a CNN model for intricate flame structures could pose initial challenges; however once implemented, it holds significant promise for enabling comprehensive analysis of the reconstructed results.

6.2.3. Recommendation for validation of CTC results

While the reconstruction outcomes may capture distinct 3D pure hydrogen flame characteristics relevant to flashback phenomena, there exists no prior three-dimensional data to serve as validation for such findings. Hence, in the subsequent project phase, it is advisable to extract a 2D cross-section from the reconstructed results and compare it with 2D measurement techniques like Mie-scattering images taken at the corresponding flame cross-section. This approach could offer valuable insights and aid in validating the accuracy of the reconstructed flame features.

A

Appendix 1: Images Acquired and Intensity profiles

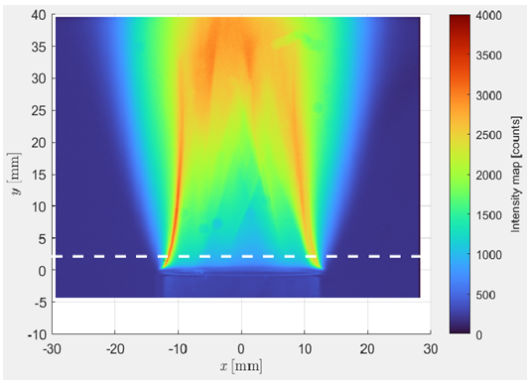

(a) Camera 1

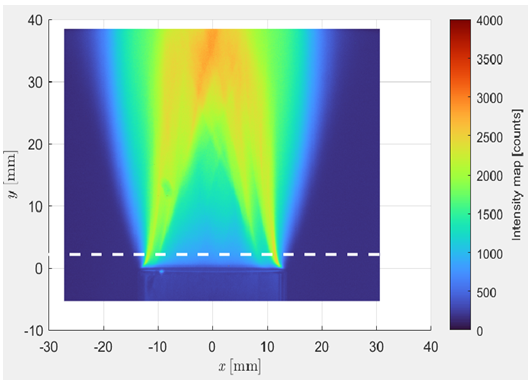

(b) Camera 2

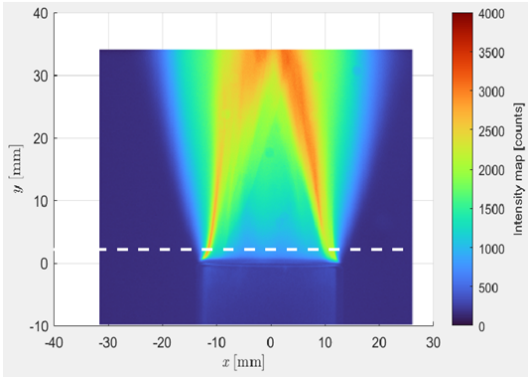

(c) Camera 3

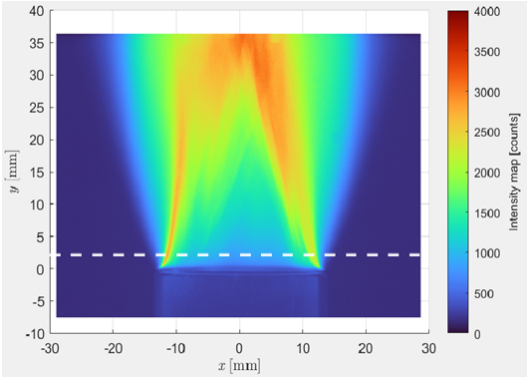

(d) Camera 4

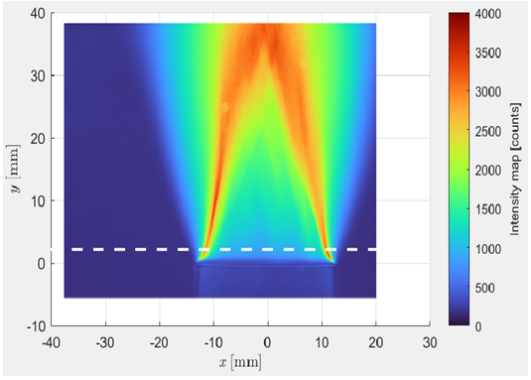

(e) Camera 5

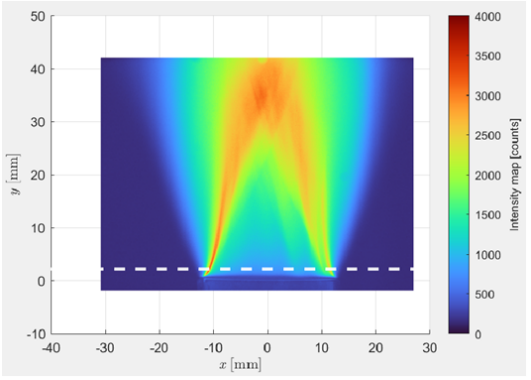

(f) Camera 6

Figure A.1: Set of simultaneous images acquired for 100% DNG flame at Re = 2750 from all six cameras. The white-dashed line represents the section at which intensity profiles have been extracted.

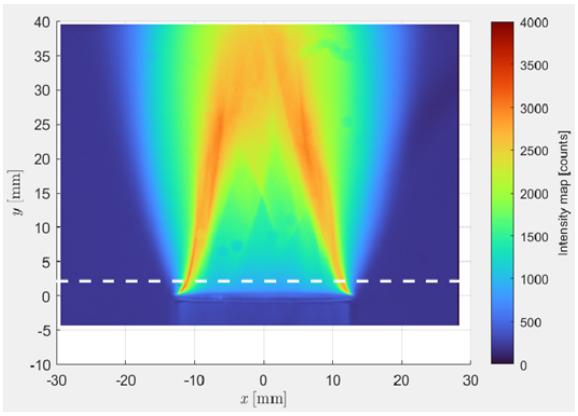

(a) Camera 1

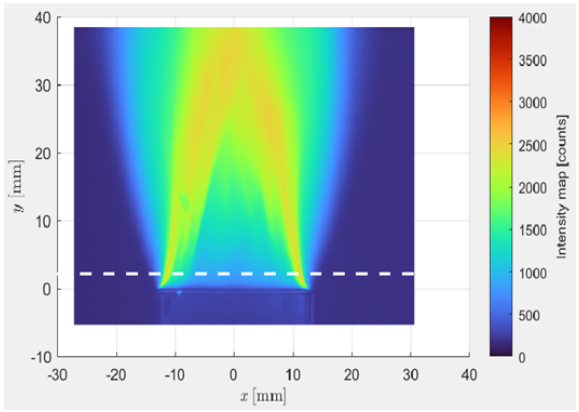

(b) Camera 2

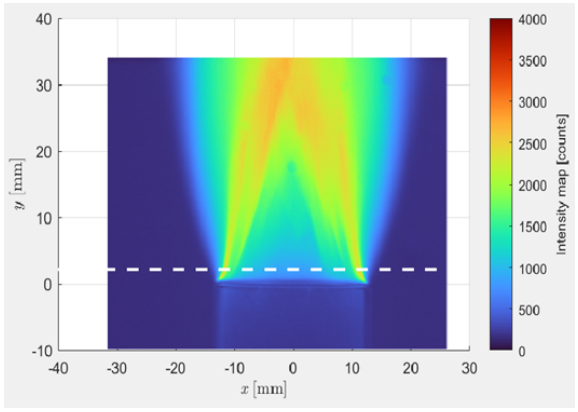

(c) Camera 3

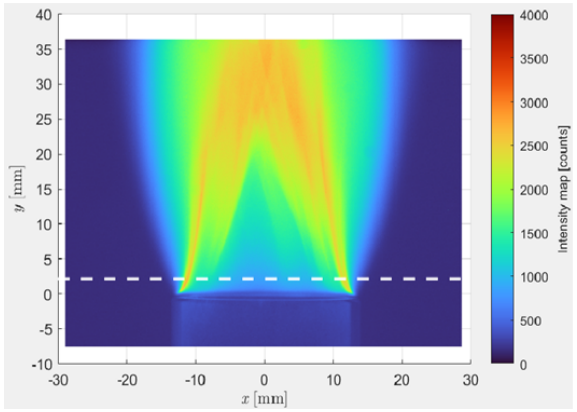

(d) Camera 4

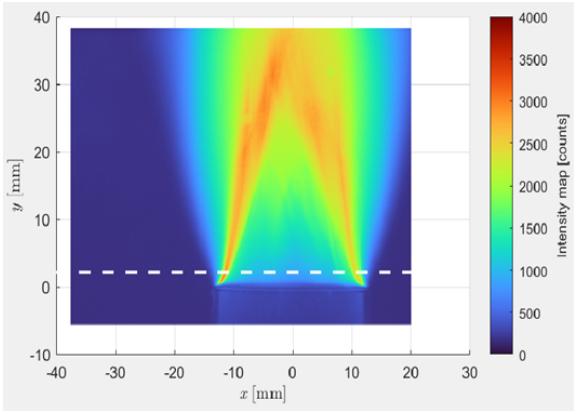

(e) Camera 5

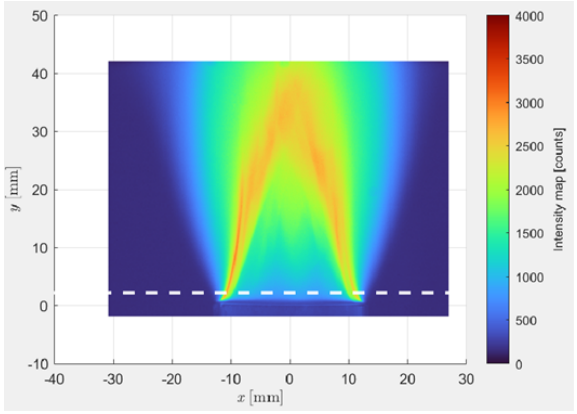

(f) Camera 6

Figure A.2: Set of simultaneous images acquired for 100% DNG flame at Re = 2300 from all six cameras. The white-dashed line represents the section at which intensity profiles have been extracted.

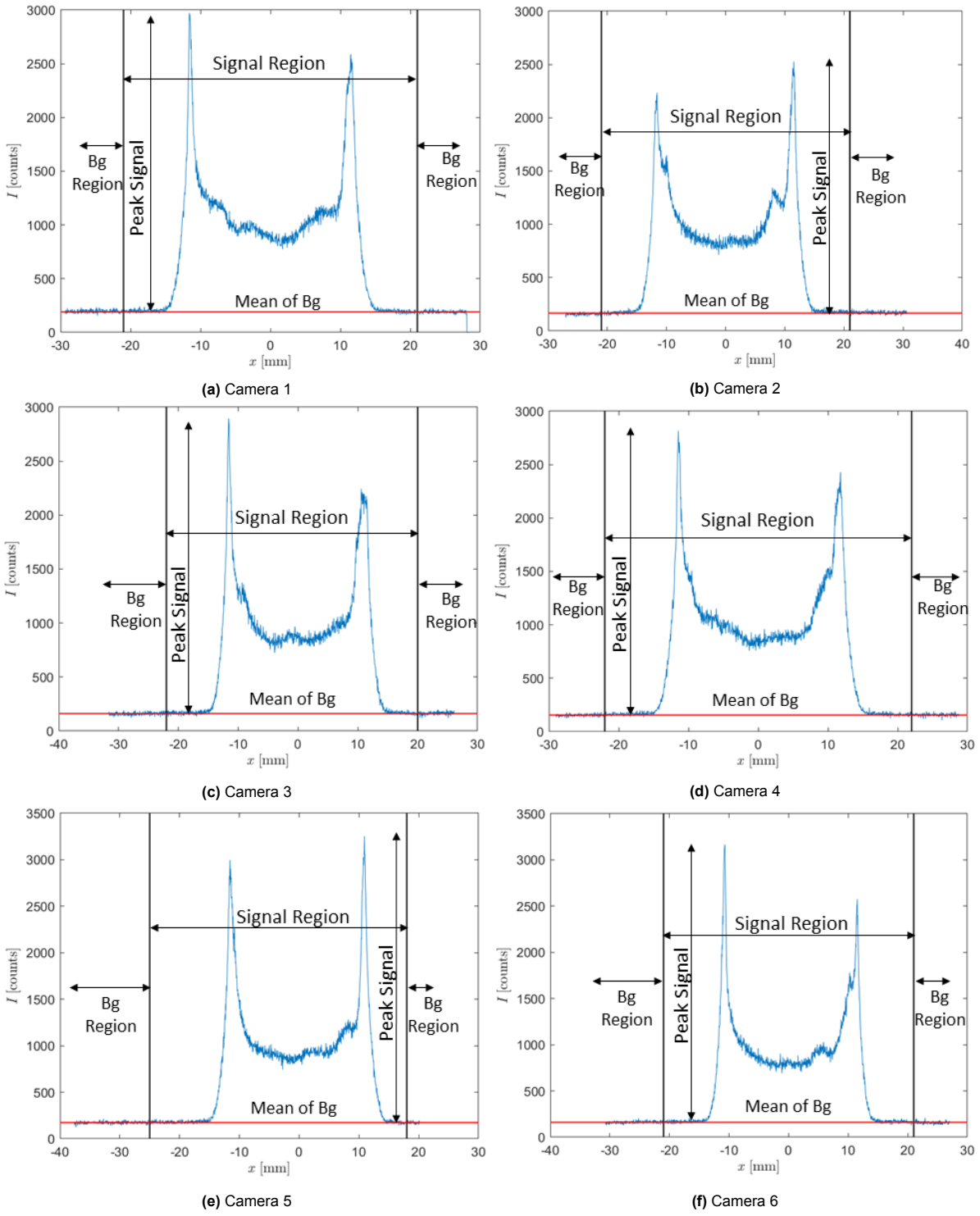

(a) Camera 1

(b) Camera 2

(c) Camera 3

(d) Camera 4

(e) Camera 5

(f) Camera 6

Figure A.3: Set of intensity profiles of simultaneous images acquired for 100% DNG flame at Re = 2750 from all six cameras. The profiles have been extracted from a segment of flame positioned at a height of 2.17 mm above the quartz tube rim as marked by white dashed lines in Figure A.1.

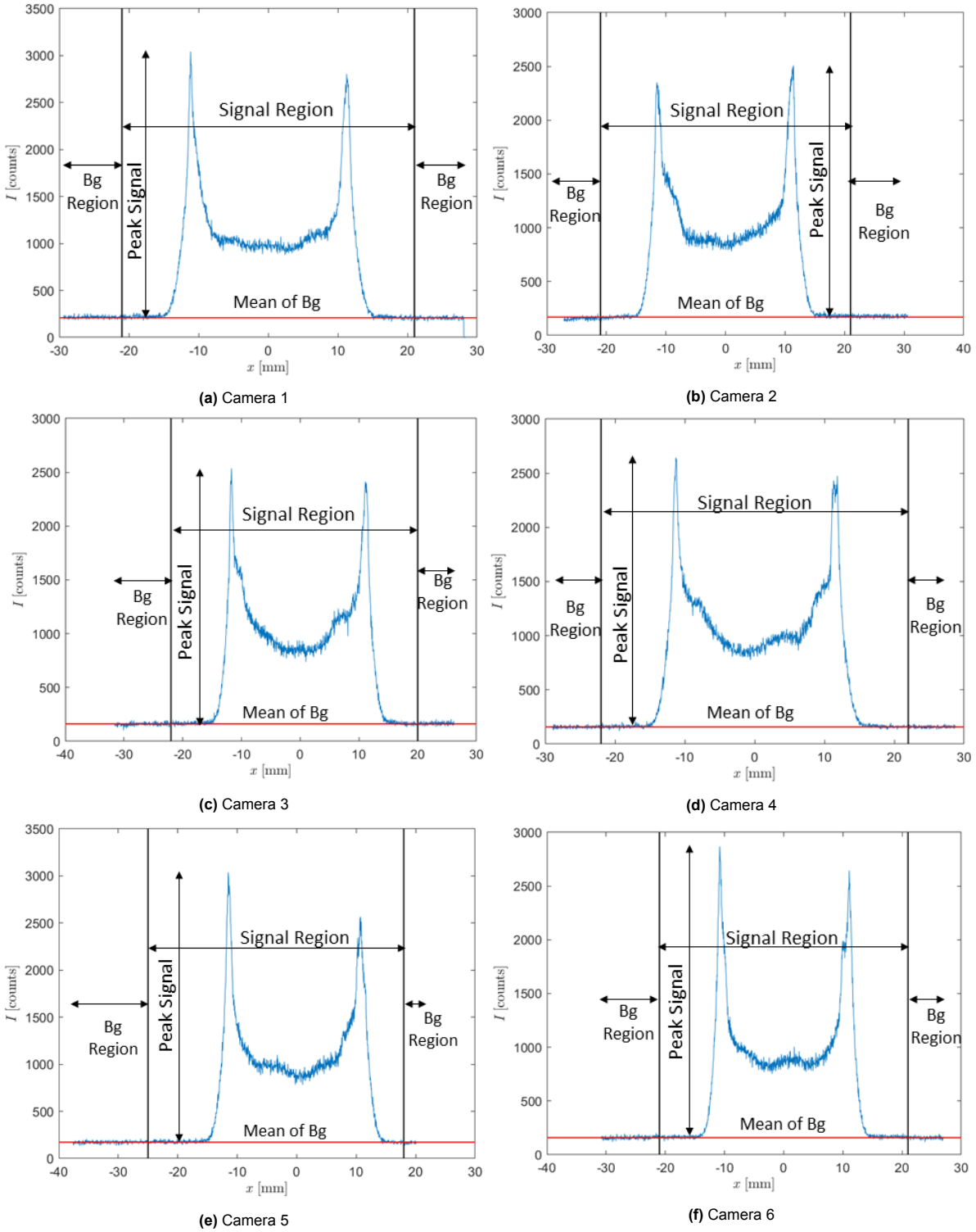

(a) Camera 1

(b) Camera 2

(c) Camera 3

(d) Camera 4

(e) Camera 5

(f) Camera 6

Figure A.4: Set of intensity profiles of simultaneous images acquired for 100% DNG flame at Re = 2300 from all six cameras. The profiles have been extracted from a segment of flame positioned at a height of 2.17 mm above the quartz tube rim as marked by white dashed lines in Figure A.2.

B

Appendix 2: Relevant parameters of intensity profiles

Camera Number	Mean of background [counts]	Peak of signal [counts]	Mean of signal [counts]	RMS of background [counts]
1.	190.73	2783.26	634.58	27.86
2.	166.67	2360.32	595.01	14.32
3.	161.37	2733.62	603.57	14.25
4.	155.53	2662.46	611.4	12.56
5.	173.71	3080.28	617.13	12.88
6.	160.75	3004.24	555.56	13.67

Table B.1: Relevant parameters of intensity profile for simultaneously captured images of 100% DNG flame at Re = 2750.

Camera Number	Mean of background [counts]	Peak of signal [counts]	Mean of signal [counts]	RMS of background [counts]
1.	208.63	2834.36	652.83	30.32
2.	169.95	2340	613.9	17.22
3.	161.68	2375.31	621.77	14.4
4.	157.67	2486.32	628.45	11.4
5.	171.99	2867	635.93	13.07
6.	158.7	2710.29	577.39	13.05

Table B.2: Relevant parameters of intensity profile for simultaneously captured images of 100% DNG flame at Re = 2300.

References

[1] A.Cappelletti and F.Martelli. “Investigation of a pure hydrogen fueled gas turbine burner”. In: *International Journal of Hydrogen Energy* 42.15 (2017), pp. 10513–10523. ISSN: 0360-3199. DOI: https://doi.org/10.1016/j.ijhydene.2017.02.104.

[2] A.Kalantari, E.Sullivan-Lewis, and V.McDonell. “Flashback propensity of turbulent hydrogen–air jet flames at gas turbine premixer conditions”. In: *Journal of Engineering for Gas Turbines and Power* 138.6 (2016), p. 061506.

[3] A.Kalantari and V.McDonell. “Boundary layer flashback of non-swirling premixed flames: Mechanisms, fundamental research, and recent advances”. In: *Progress in Energy and Combustion Science* 61 (2017), pp. 249–292. ISSN: 0360-1285. DOI: https://doi.org/10.1016/j.pecs.2017.03.001.

[4] A.Unterberger, J.Menser, and K.Mohri. “Evolutionary camera pose estimation of a multi-camera setup for computed tomography”. In: *2019 IEEE International Conference on Image Processing (ICIP)*. IEEE. 2019, pp. 464–468.

[5] C.Ruan, T.Yu, F.Chen, S.Wang, W.Cai, and X.Lu. “Experimental characterization of the spatiotemporal dynamics of a turbulent flame in a gas turbine model combustor using computed tomography of chemiluminescence”. In: *Energy* 170 (2019), pp. 744–751. ISSN: 0360-5442. DOI: https://doi.org/10.1016/j.energy.2018.12.215.

[6] D.Verhoeven. “Limited-data computed tomography algorithms for the physical sciences”. In: *Appl. Opt.* 32.20 (1993), pp. 3736–3754. DOI: 10.1364/AO.32.003736.

[7] G. E.Elsinga, F.Scarano, B.Wieneke, and B. W.van Oudheusden. “Tomographic particle image velocimetry”. In: *Experiments in fluids* 41.6 (2006), pp. 933–947.

[8] D. Ebi, R. Bombach, and P. Jansohn. “Swirl flame boundary layer flashback at elevated pressure: Modes of propagation and effect of hydrogen addition”. In: *Proceedings of the Combustion Institute* 38.4 (2021), pp. 6345–6353. ISSN: 1540-7489. DOI: https://doi.org/10.1016/j.proci.2020.06.305.

[9] F.Faldella. “Experimental investigation of Boundary Layer Flashback in high hydrogen concentration turbulent premixed jet flames”. In: *Master thesis, Delft University of Technology* (2020).

[10] F.Halter, C.Chauveau, and I.Gökalp. “Characterization of the effects of hydrogen addition in premixed methane/air flames”. In: *International Journal of Hydrogen Energy* 32.13 (2007). ICHS-2005, pp. 2585–2592. ISSN: 0360-3199. DOI: https://doi.org/10.1016/j.ijhydene.2006.11.033.

[11] F.J.W.A.Martins, A.Unterberger, and K.Mohri. “Tomographic imaging using multi-simultaneous measurements (TIMes) of emission and refractive index 3D fields in turbulent flames”. In: *Proceedings of the Combustion Institute* (2022). ISSN: 1540-7489. DOI: https://doi.org/10.1016/j.proci.2022.09.007.

[12] F.Zhang, W.Zhang, Q.Lei, X.Li, Y.Li, and M.Xu. “Voxel-free Neural Volume Reconstruction Technique for Volumetric Flame Reconstructions”. In: *Aerospace Science and Technology* (2023), p. 108107.

[13] J. Floyd, P. Geipel, and A.M. Kempf. “Computed Tomography of Chemiluminescence (CTC): Instantaneous 3D measurements and Phantom studies of a turbulent opposed jet flame”. In: *Combustion and Flame* 158.2 (2011), pp. 376–391. ISSN: 0010-2180. DOI: https://doi.org/10.1016/j.combustflame.2010.09.006.

[14] J. Floyd and A.M. Kempf. “Computed Tomography of Chemiluminescence (CTC): High resolution and instantaneous 3-D measurements of a Matrix burner”. In: *Proceedings of the Combustion Institute* 33.1 (2011), pp. 751–758. ISSN: 1540-7489. DOI: https://doi.org/10.1016/j.proci.2010.06.015.

[15] G.Cerri, M.Gazzino, F.Botta, and C.Salvini. “Production Planning with Hot Section Life Prediction for Optimum Gas Turbine Management”. In: *International Journal of Gas Turbine, Propulsion and Power Systems* 2.1 (2008), pp. 9–16.

[16] G.Willems. “Unraveling Flashback Phenomena of Turbulent premixed Hydrogen-Natural Gas-Air Flames”. In: *Master thesis, Delft University of Technology* (2022).

[17] J.Ballester and T. G.Armingol. “Diagnostic techniques for the monitoring and control of practical flames”. In: *Progress in Energy and Combustion Science* 36.4 (2010), pp. 375–411. ISSN: 0360-1285. DOI: https://doi.org/10.1016/j.pecs.2009.11.005.

[18] J.Kojima, Y.Ikeda, and T.Nakajima. “Spatially resolved measurement of OH*, CH*, and C2* chemiluminescence in the reaction zone of laminar methane/air premixed flames”. In: *Proceedings of the Combustion Institute* 28.2 (2000), pp. 1757–1764. ISSN: 1540-7489. DOI: https://doi.org/10.1016/S0082-0784(00)80577-9.

[19] J.Menser, A.Unterberger, A.Kempf, and K.Mohri. “Instantaneous 3d imaging of turbulent stratified methane/air flames using computed tomography of chemiluminescence”. In: *5th International Conference on Experimental Fluid Mechanics, Munich, Germany*. 2018, pp. 766–770.

[20] K.Mohri, S.Görs, J.Schöler, A. Rittler, T. Dreier, C.Schulz, and A.Kempf. “Instantaneous 3D imaging of highly turbulent flames using computed tomography of chemiluminescence”. In: *Appl. Opt.* 56.26 (2017), pp. 7385–7395. DOI: 10.1364/AO.56.007385.

[21] L.Ma, Y.Wu, Q. Lei, W.Xu, and C. D.Carter. “3D flame topography and curvature measurements at 5 kHz on a premixed turbulent Bunsen flame”. In: *Combustion and Flame* 166 (2016), pp. 66–75. ISSN: 0010-2180. DOI: https://doi.org/10.1016/j.combustflame.2015.12.031.

[22] X. Li and L. Ma. “Capabilities and limitations of 3D flame measurements based on computed tomography of chemiluminescence”. In: *Combustion and Flame* 162.3 (2015), pp. 642–651. ISSN: 0010-2180. DOI: https://doi.org/10.1016/j.combustflame.2014.08.020.

[23] H. Liu, J.Zhao, C.Shui, and W.Cai. “Reconstruction and analysis of non-premixed turbulent swirl flames based on kHz-rate multi-angular endoscopic volumetric tomography”. In: *Aerospace Science and Technology* 91 (2019), pp. 422–433. ISSN: 1270-9638. DOI: https://doi.org/10.1016/j.ast.2019.05.025.

[24] M.Emadi, D.Karkow, T.Salameh, A.Gohil, and Al.Ratner. “Flame structure changes resulting from hydrogen-enrichment and pressurization for low-swirl premixed methane–air flames”. In: *International Journal of Hydrogen Energy* 37.13 (2012). Proceedings of the Symposium on Hydrogen Production and Applications at the 240th American Chemical Society National Meeting, August 22-26, 2010, Boston, Massachusetts, USA, pp. 10397–10404. ISSN: 0360-3199. DOI: https://doi.org/10.1016/j.ijhydene.2012.04.017.

[25] M.Konle, F.Kiesewetter, and T.Sattelmayer. “Simultaneous high repetition rate PIV–LIF-measurements of CIVB driven flashback”. In: *Experiments in Fluids* 44 (2008), pp. 529–538.

[26] M.Kroener, T.Sattelmayer, J.Fritz, F.Kiesewetter, and C.Hirsch. “Flame propagation in swirling flows—effect of local extinction on the combustion induced vortex breakdown”. In: *Combustion Science and Technology* 179.7 (2007), pp. 1385–1416.

[27] M.Moliere. “Expanding fuel flexibility of gas turbines”. In: *Proceedings of the Institution of Mechanical Engineers, Part A: Journal of Power and Energy* 219.2 (2005), pp. 109–119. DOI: 10.1243/095765005X6818.

[28] M.Zhang, J.Wang, Y. Xie, W.Jin, Z.Wei, Z.Huang, and H.Kobayashi. “Flame front structure and burning velocity of turbulent premixed CH4/H2/air flames”. In: *International Journal of Hydrogen Energy* 38.26 (2013), pp. 11421–11428. ISSN: 0360-3199. DOI: https://doi.org/10.1016/j.ijhydene.2013.05.051.

[29] M.Zhang, M.Chang, J.Wang, and Z.Huang. “Flame dynamics analysis of highly hydrogen-enrichment premixed turbulent combustion”. In: *international journal of hydrogen energy* 45.1 (2020), pp. 1072–1083.

[30] N.A.Worth and J.R.Dawson. “Tomographic reconstruction of OH* chemiluminescence in two interacting turbulent flames”. In: *Measurement Science and Technology* 24.2 (2012), p. 024013. DOI: 10.1088/0957-0233/24/2/024013. URL: https://dx.doi.org/10.1088/0957-0233/24/2/024013.

[31] P.Kumar, R.Britter, and N.Gupta. “Hydrogen Fuel: Opportunities and Barriers”. In: *Journal of Fuel Cell Science and Technology* 6.2 (Feb. 2009), p. 021009. ISSN: 1550-624X. DOI: 10.1115/1.3005384.

[32] S.Rong, Y.Song, C.Wu, Q.Yuan, Z.Gao, and Z.Guo. “A camera array based reconstruction method for limited observation windows projection in three-dimensional flame chemiluminescence tomography”. In: *Engineering Research Express* 4.3 (2022), p. 035003.

[33] P. Sampath and F. Shum. “Combustion performance of hydrogen in a small gas turbine combustor”. In: *International Journal of Hydrogen Energy* 10.12 (1985), pp. 829–837. ISSN: 0360-3199. DOI: https://doi.org/10.1016/0360-3199(85)90172-7.

[34] R.W. Schefer, W.D. Kulatilaka, B.D. Patterson, and T.B. Settersten. “Visible emission of hydrogen flames”. In: *Combustion and Flame* 156.6 (2009), pp. 1234–1241. ISSN: 0010-2180. DOI: https://doi.org/10.1016/j.combustflame.2009.01.011.

[35] U. Stopper, M. Aigner, H. Ax, W. Meier, R. Sadanandan, M. Stöhr, and A. Bonaldo. “PIV, 2D-LIF and 1D-Raman measurements of flow field, composition and temperature in premixed gas turbine flames”. In: *Experimental Thermal and Fluid Science* 34.3 (2010). Sixth Mediterranean Combustion Symposium, pp. 396–403. ISSN: 0894-1777. DOI: https://doi.org/10.1016/j.expthermflusci.2009.10.012.

[36] T.García-Armingol and J.Ballester. “Flame chemiluminescence in premixed combustion of hydrogen-enriched fuels”. In: *International Journal of Hydrogen Energy* 39.21 (2014), pp. 11299–11307.

[37] T.Lieuwen, V.McDonell, D.Santavicca, and T.Sattelmayer. “Burner Development and Operability Issues Associated with Steady Flowing Syngas Fired Combustors”. In: *Combustion Science and Technology* 180.6 (2008), pp. 1169–1192. DOI: 10.1080/00102200801963375.

[38] F.H. Vance, L.P.H. de Goey, and J.A. van Oijen. “Development of a flashback correlation for burner-stabilized hydrogen-air premixed flames”. In: *Combustion and Flame* 243 (2022). A dedication to Professor Katharina Kohse-Höinghaus, p. 112045. ISSN: 0010-2180. DOI: https://doi.org/10.1016/j.combustflame.2022.112045.

[39] X.Liu, M.Bertsch, A.A.Subash, S.Yu, R.Z.Szasz, Z. Li, P.Petersson, X.S.Bai, M. Aldén, and D.Lörstad. “Investigation of turbulent premixed methane/air and hydrogen-enriched methane/air flames in a laboratory-scale gas turbine model combustor”. In: *International Journal of Hydrogen Energy* 46.24 (2021), pp. 13377–13388. ISSN: 0360-3199. DOI: https://doi.org/10.1016/j.ijhydene.2021.01.087.

[40] Y.C.Lin, S.Daniele, P.Jansohn, and K.Boulouchos. “Turbulent flame speed as an indicator for flashback propensity of hydrogen-rich fuel gases”. In: *Journal of engineering for gas turbines and power* 135.11 (2013), p. 111503.

[41] Y.Ikeda, J.Kojima, T.Nakajima, F.Akamatsu, and M.Katsuki. “Measurement of the local flame-front structure of turbulent premixed flames by local chemiluminescence”. In: *Proceedings of the Combustion Institute* 28.1 (2000), pp. 343–350. ISSN: 1540-7489. DOI: https://doi.org/10.1016/S0082-0784(00)80229-5.

[42] Y.ISHINO and N.OHIWA. “Three-Dimensional Computerized Tomographic Reconstruction of Instantaneous Distribution of Chemiluminescence of a Turbulent Premixed Flame”. In: *JSME International Journal Series B Fluids and Thermal Engineering* 48.1 (2005), pp. 34–40. DOI: 10.1299/jsmeb.48.34.

[43] Y.Jin and G.Situ. “A Survey for 3D Flame Chemiluminescence Tomography: Theory, Algorithms, and Applications”. In: *Frontiers in Photonics* 3 (2022). ISSN: 2673-6853. DOI: 10.3389/fphot.2022.845971.

[44] Y.Jin, W.Zhang, Y.Song, X.Qu, Z.Li, Y.Ji, and A.He. “Three-dimensional rapid flame chemiluminescence tomography via deep learning”. In: *Optics express* 27.19 (2019), pp. 27308–27334.

[45] M. Zhang, J.Wang, Y.Xie, Z.Wei, W.Jin, Z.Huang, and H.Kobayashi. “Measurement on instantaneous flame front structure of turbulent premixed CH4/H2/air flames”. In: *Experimental Thermal and Fluid Science* 52 (2014), pp. 288–296. ISSN: 0894-1777. DOI: https://doi.org/10.1016/j.expthermflusci.2013.10.002.